

Spectroscopy[®]

Solutions for Materials Analysis

Safety and disposability
from the leader in
microwave digestion.



We Simplify Science

cem.com/glass-vessels

Your safety is our top priority

In 1986, CEM introduced the first microwave digestion system in the world. Since then we have worked to improve digestion performance and build safety into each and every system. We are thrilled that we can now offer disposable digestion in a system that keeps you safe. CEM's disposable glass vessels bring all the benefits of other systems with disposable technology, including elimination of vessel washing and risk of

cross-contamination, but CEM disposable glass vessels operate at moderate pressures of ~300 psi, instead of extreme pressures of ~3,000 psi typical of other systems, keeping you and your team safe.

To schedule a free demonstration of CEM's disposable digestion solution contact us today at 800-726-3331 or info@cem.com.



Safe

Easy to use

Capable of digesting
24 samples per batch

Easy to install — No nitrogen
tanks or chillers necessary

Your solution to improved
laboratory efficiency



We Simplify Science

cem.com/glass-vessels



Spectroscopy[®]

Solutions for Materials Analysis

September 2019 Volume 34 Number 9

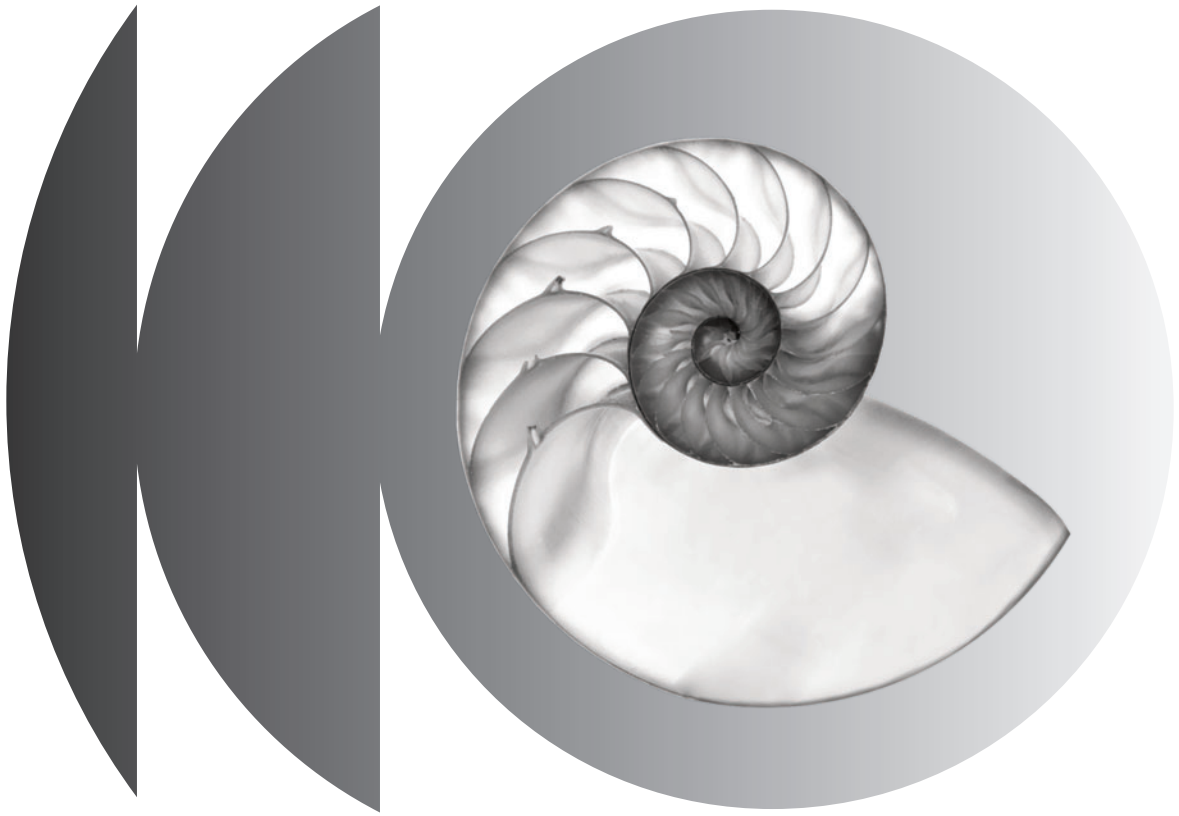
www.spectroscopyonline.com

Characterizing Polymer Melts with Raman Spectroscopy and Rheology

Stress, Strain, and Raman Spectroscopy

Identifying Primary, Secondary, and Tertiary Anime Salts

Do You Have a Hidden Data Integrity Problem?



The best ideas grow

OCEAN OPTICS IS NOW OCEAN INSIGHT.

Our name change represents deep investment in optical sensing solutions and expanded peer partner services to help bring greater value to our customers. From business or research challenges through to solutions, we can help provide greater understanding and actionable insights through products and people. “Insight” reflects the knowledge we bring, the solutions we provide, and the partnerships we value.

We seek to deliver insights at every level.



oceaninsight.com

Specac

THE GOLDEN GATE ATR

and Specac's added value top plates

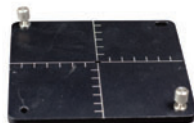
Find out more about our ATR, Diffuse Reflectance, Transmission products in the new Specac's Secrets Catalogue, including our Golden Gate, and it's Top Plates



High Temperature Top Plate



Low Temperature Top Plate



Micro-Specular Top Plate



Supercritical Fluids Top Plate



Reaction Cell Top Plate



Anvil Options



UK: 01689 873134 | WWW.SPECAC.COM | US: +1 866 726 1126

We are attending **SOIX**
2019

Booth number
310

Spectroscopy®

MANUSCRIPTS: To discuss possible article topics or obtain manuscript preparation guidelines, contact the editorial director at: (732) 346-3020, e-mail: LBush@mmhgroup.com.

Publishers assume no responsibility for safety of artwork, photographs, or manuscripts. Every caution is taken to ensure accuracy, but publishers cannot accept responsibility for the information supplied herein or for any opinion expressed.

SUBSCRIPTIONS: For subscription information: *Spectroscopy*, P.O. Box 6196, Duluth, MN 55806-6196; (888) 527-7008, 7:00 a.m. to 6:00 p.m. CST. Outside the U.S., +1-218-740-6477. Delivery of *Spectroscopy* outside the U.S. is 3–14 days after printing. Single-copy price:

U.S., \$10.00 + \$7.00 postage and handling (\$17.00 total); Canada and Mexico, \$12.00 + \$7.00 postage and handling (\$19.00 total); Other international, \$15.00 + \$7.00 postage and handling (\$22.00 total).

CHANGE OF ADDRESS: Send change of address to *Spectroscopy*, P.O. Box 6196, Duluth, MN 55806-6196; provide old mailing label as well as new address; include ZIP or postal code. Allow 4–6 weeks for change. Alternately, go to the following URL for address changes or subscription renewal: <http://ubmsubs.ubm.com/?pubid=SPEC>

RETURN ALL UNDELIVERABLE CANADIAN ADDRESSES TO: IMEX Global Solutions, P.O. Box 25542, London, ON N6C 6B2, CANADA. PUBLICATIONS MAIL AGREEMENT No.40612608.

REPRINT SERVICES: Reprints of all articles in this issue and past issues are available (500 minimum). Licensing and Reuse of Content: Contact our official partner, Wright's Media, about available usages, license fees, and award seal artwork at Advantstarwrightsmedia.com for more information. Please note that Wright's Media is the only authorized company that we've partnered with for MultiMedia Healthcare materials.

C.A.S.T. DATA AND LIST INFORMATION: Contact Melissa Stillwell, (218) 740-6831; e-mail: MStillwell@mmhgroup.com

INTERNATIONAL LICENSING: Alexa Rockenstein, (609) 819-6019, e-mail: ARockenstein@mmhgroup.com



© 2019 MultiMedia Healthcare LLC. All rights reserved. No part of this publication may be reproduced or transmitted in any form or by any means, electronic or mechanical including by photocopy, recording, or information storage and retrieval without permission in writing from the publisher. Authorization to photocopy items for internal/educational or personal use, or the internal/educational or personal use of specific clients is granted by MultiMedia Healthcare LLC for libraries and other users registered with the Copyright Clearance Center, 222 Rosewood Dr. Danvers, MA 01923, 978-750-8400 fax 978-646-8700 or visit <http://www.copyright.com> online. For uses beyond those listed above, please direct your written request to Permission Dept. email: ARockenstein@mmhgroup.com.

MultiMedia Healthcare LLC provides certain customer contact data (such as customers' names, addresses, phone numbers, and e-mail addresses) to third parties who wish to promote relevant products, services, and other opportunities that may be of interest to you. If you do not want MultiMedia Healthcare LLC to make your contact information available to third parties for marketing purposes, simply call toll-free 866-529-2922 between the hours of 7:30 a.m. and 5 p.m. CST and a customer service representative will assist you in removing your name from MultiMedia Healthcare LLC lists. Outside the U.S., please phone 218-740-6477.

Spectroscopy does not verify any claims or other information appearing in any of the advertisements contained in the publication, and cannot take responsibility for any losses or other damages incurred by readers in reliance of such content.

Spectroscopy welcomes unsolicited articles, manuscripts, photographs, illustrations and other materials but cannot be held responsible for their safekeeping or return.

To subscribe, call toll-free 888-527-7008. Outside the U.S. call 218-740-6477.

485F US Highway One South, Suite 210
Iselin, NJ 08830
(732) 596-0276
Fax: (732) 647-1235

Michael J. Tessalone

Group Vice President/MTessalone@mmhgroup.com

Stephanie Shaffer

Publisher/SShaffer@mmhgroup.com

Edward Fantuzzi

Associate Publisher/EFantuzzi@mmhgroup.com

Michael Kushner

Senior Director, Digital Media/MKushner@mmhgroup.com

Laura Bush

Editorial Director/LBush@mmhgroup.com

John Chasse

Managing Editor/JChasse@mmhgroup.com

Jerome Workman, Jr.

Senior Technical Editor/JWorkman@mmhgroup.com

Cindy Delonas

Associate Editor/CDelonas@mmhgroup.com

Allissa Marrapodi

Custom Content Writer/AMarrapodi@mmhgroup.com

Kristen Moore

Webcast Operations Manager/KMoore@mmhgroup.com

Vania Oliveira

Project Manager/VOliveira@mmhgroup.com

Sabina Advani

Digital Production Manager/SAdvani@mmhgroup.com

Kaylynn Chiarello-Ebner

Managing Editor, Special Projects/KEbner@mmhgroup.com

Dan Ward

Art Director/dward@hcl.com

Brianne Pangaro

Marketing Associate/BPangaro@mmhgroup.com

Melissa Stillwell

C.A.S.T. Data and List Information/MStillwell@mmhgroup.com

Alexa Rockenstein

Permissions/ARockenstein@mmhgroup.com

Jesse Singer

Production Manager/jsinger@hcl.com

Kelly Kemper

Audience Development Manager/KKemper@mmhgroup.com

Janet (Koehne) Roberts

Audience Support Analyst/JKoehne@mmhgroup.com

CORPORATE

Mike Hennessy, Sr.

Chairman and CEO/MHennessy@mjhassociates.com

Jack Lepping

Vice Chairman/JLepping@mjhassociates.com

Mike Hennessy, Jr.

President/MJHennessy@mjhassociates.com

George Glatz

Chief Operations Officer/GGlatz@mjhassociates.com

Neil Glasser, CPA/CPE

Chief Financial Officer/NGlasser@mdmag.com

Dave Esola

VP of Sales, Pharm Science/DEsola@mmhgroup.com



MB3000-CH90 laboratory gas analyzer

Measurement made easy

The MB3000-CH90 gas analyzer provides fast and accurate FT-IR critical gas measurements down to ppb levels in a user-friendly environment. This high performance and maintenance-free spectrometer is used in R&D or QA/QC laboratories for checking gas purity, controlling gas mixing and composition or performing unknown components speciation. The heated gas cell can be easily swapped and replaced with other sampling accessories, making the MB3000-CH90 a flexible and versatile tool for any laboratory.

Measurement made easy.

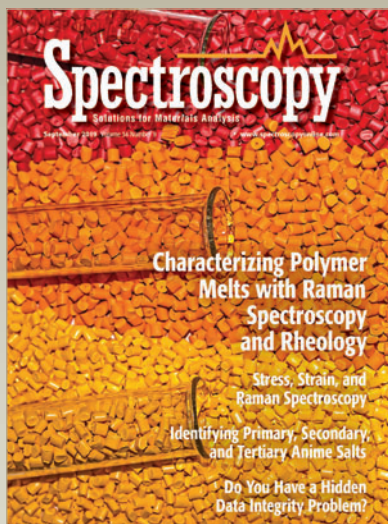
Want to learn more? Visit abb.com/analytical
or contact us at ftir@ca.abb.com



Spectroscopy

September 2019

Volume 34 Number 9



Cover image courtesy of
mmrmsmarc1/AdobeStock.

ON THE WEB

WEB SEMINARS

Maximize Your Profitability and Brand Loyalty Through High Quality Terpene Extraction

Stephen Markle, Planet 13 Holdings and Roberto Federico-Perez, Milestone, Inc.

Potency, Pesticides, and Metals, Oh My! Achieving Superior Cannabis Analyses with Simple Sample Prep Tools

Alicia Douglas Stell and Bob Lockerman, CEM Corporation

What's in Your Breakfast? Reliable Methods for Elemental Nutrient and Arsenic Speciation Analysis

Ken Neubauer and Eve Kroukamp, PerkinElmer, Inc.

How to Take the Next Step in Correlative Raman Imaging of Polymers and Microplastics

Ute Schmidt, WITec GmbH

<http://www.spectroscopyonline.com/spec/webcasts>

Like *Spectroscopy* on Facebook:
www.facebook.com/SpectroscopyMagazine

Follow *Spectroscopy* on Twitter:
<https://twitter.com/SpectroscopyMag>

Join the *Spectroscopy* Group on LinkedIn
<http://linkd.in/SpecGroup>



CONTENTS

COLUMNS

Molecular Spectroscopy Workbench 10

Stress, Strain, and Raman Spectroscopy

David Tuschel

When stress is applied to an object, it can produce strain. Strain can be detected through changes in peak position and bandwidth in Raman spectra. Here, we show examples of how strain in technologically important materials appears in the Raman spectra.

Focus on Quality 22

Analysis of FDA Infrared 483 Citations: Have You a Data Integrity Problem?

P.A. Smith and R.D. McDowall

Analysis of FDA Form 483 observations and warning letters for infrared spectrometers reveals a range of data integrity problems and a lack of laboratory procedures for the technique. Is your laboratory in the same situation?

IR Spectral Interpretation Workshop 30

Organic Nitrogen Compounds V: Amine Salts

Brian C. Smith

The amine salt functional group contains ionic bonding, and is extremely polar, giving rise to a number of intense and uniquely placed peaks that are easy to identify for primary, secondary, and tertiary amines.

FEATURE ARTICLE

Combined Raman Spectroscopy and Rheology for Characterizing Polymer Melts. 38

Fredrik Fleissner, Katharina E. Napp, Boris Wezista, and Loredana Völker-Pop

By combining Raman spectra interpretation with rheometric measurements, molecular conversion from crystalline to amorphous structures for polymers is revealed.

THE APPLICATION NOTEBOOK 45

DEPARTMENTS

Products & Resources 44

Ad Index 44

Spectroscopy (ISSN 0887-6703 [print], ISSN 1939-1900 [digital]) is published monthly by MultiMedia Healthcare LLC 325 W 1st St STE 300 Duluth MN 55802. *Spectroscopy* is distributed free of charge to users and specifiers of spectroscopic equipment in the United States. *Spectroscopy* is available on a paid subscription basis to nonqualified readers at the rate of: U.S. and possessions: 1 year (12 issues), \$74.95; 2 years (24 issues), \$134.50. Canada/Mexico: 1 year, \$95; 2 years, \$150. International: 1 year (12 issues), \$140; 2 years (24 issues), \$250. Periodicals postage paid at Duluth, MN 55806 and at additional mailing offices. POSTMASTER: Send address changes to *Spectroscopy*, P.O. Box 6196, Duluth, MN 55806-6196. PUBLICATIONS MAIL AGREEMENT NO. 40612608, Return Undeliverable Canadian Addresses to: IMEX Global Solutions, P. O. Box 25542, London, ON N6C 6B2, CANADA. Canadian GST number: R-124213133RT001. Printed in the U.S.A.

State-of-the-Art XRF Solutions

•FAST SDD®

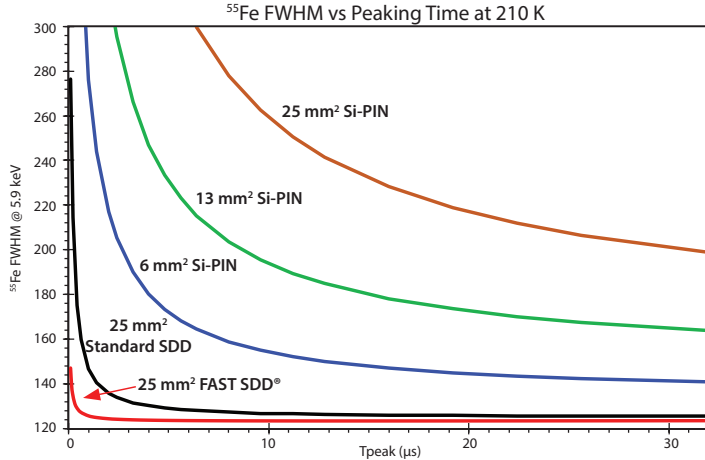
•SDD

•Si-PIN

In-house manufacturing = The highest performing detectors available

The best detector for optimal results

Amptek Detector Comparison: Si-PIN, Standard SDD, and FAST SDD®



FAST SDD® Detector

>2,000,000 CPS and 122 eV FWHM Resolution

Options:

- 25 mm² collimated to 17 mm²
- 70 mm² collimated to 50 mm²
- Windows: Be (0.5 mil) 12.5 μm, or C Series (Si₃N₄)
- TO-8 package fits all Amptek configurations

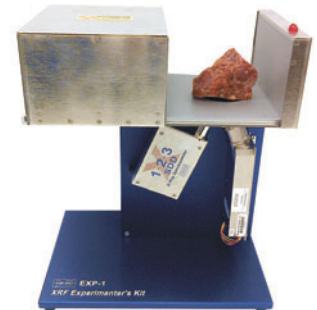
Configurations to meet your needs



XR-100 and PX5 Digital Pulse Processor



X-123 Complete X-Ray Spectrometer

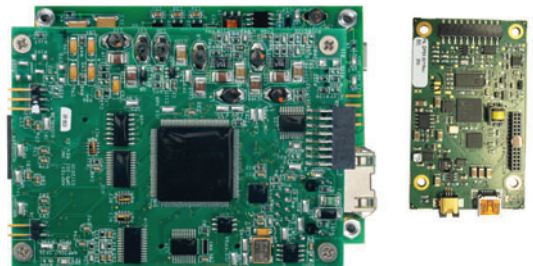


XRF Experimenters Kit

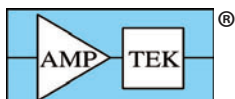
OEM Configurations



A sample of detectors with preamplifiers and heat sinks



Digital Pulse Processors and Power Supplies



OEM's #1 Choice
For XRF

amptek.com

AMETEK®
MATERIALS ANALYSIS DIVISION

Editorial Advisory Board

Fran Adar Horiba Scientific

Russ Algar University of British Columbia

Matthew J. Baker University of Strathclyde

Ramon M. Barnes University of Massachusetts

Mathieu Baudelet University of Central Florida

Rohit Bhargava University of Illinois at Urbana-Champaign

Paul N. Bourassa Blue Moon Inc.

Michael S. Bradley Thermo Fisher Scientific

Deborah Bradshaw Consultant

Lora L. Brehm The Dow Chemical Company

George Chan Lawrence Berkeley National Laboratory

John Cottle University of California Santa Barbara

David Lankin University of Illinois at Chicago,
College of Pharmacy

Barbara S. Larsen DuPont Central Research and Development

Bernhard Lendl Vienna University of Technology (TU Wien)

Ian R. Lewis Kaiser Optical Systems

Rachel R. Ogorzalek Loo University of California Los Angeles,
David Geffen School of Medicine

Howard Mark Mark Electronics

R.D. McDowall McDowall Consulting

Gary McGeorge Bristol-Myers Squibb

Linda Baine McGown Rensselaer Polytechnic Institute

Francis M. Mirabella Jr. Mirabella Practical Consulting Solutions, Inc.

Ellen V. Miseo Illuminate

Michael L. Myrick University of South Carolina

John W. Olesik The Ohio State University


Steven Ray State University of New York at Buffalo

Jim Rydzak Specere Consulting


Jerome Workman Jr. Unity Scientific

Lu Yang National Research Council Canada

Spectroscopy's Editorial Advisory Board is a group of distinguished individuals assembled to help the publication fulfill its editorial mission to promote the effective use of spectroscopic technology as a practical research and measurement tool. With recognized expertise in a wide range of technique and application areas, board members perform a range of functions, such as reviewing manuscripts, suggesting authors and topics for coverage, and providing the editor with general direction and feedback. We are indebted to these scientists for their contributions to the publication and to the spectroscopy community as a whole.



Next generation Raman imaging



High performance Raman systems for a range of applications

Raman spectroscopy produces chemical and structural images to help you understand more about the material being analysed. Renishaw has decades of experience developing flexible Raman systems that give reliable results, for even the most challenging measurements. With Renishaw's suite of Raman systems, you can see the small things, the large things and things you didn't even know were there.

Visit www.renishaw.com/raman

See us at SCIX
BOOTH #400
Oct 14-16 | Palm Springs, CA

Renishaw Inc. 1001 Wesemann Drive, West Dundee, Illinois, 60118, United States
T +1 847 286 9953 F +1 847 286 9974 E raman@renishaw.com
www.renishaw.com

KnowItAll®

IR/Raman Identification Pro

Identify, Analyze,
& Manage Spectra



Largest Database

World's largest spectral library for most comprehensive identification



Smartest Software

Patented solutions for most accurate analyses



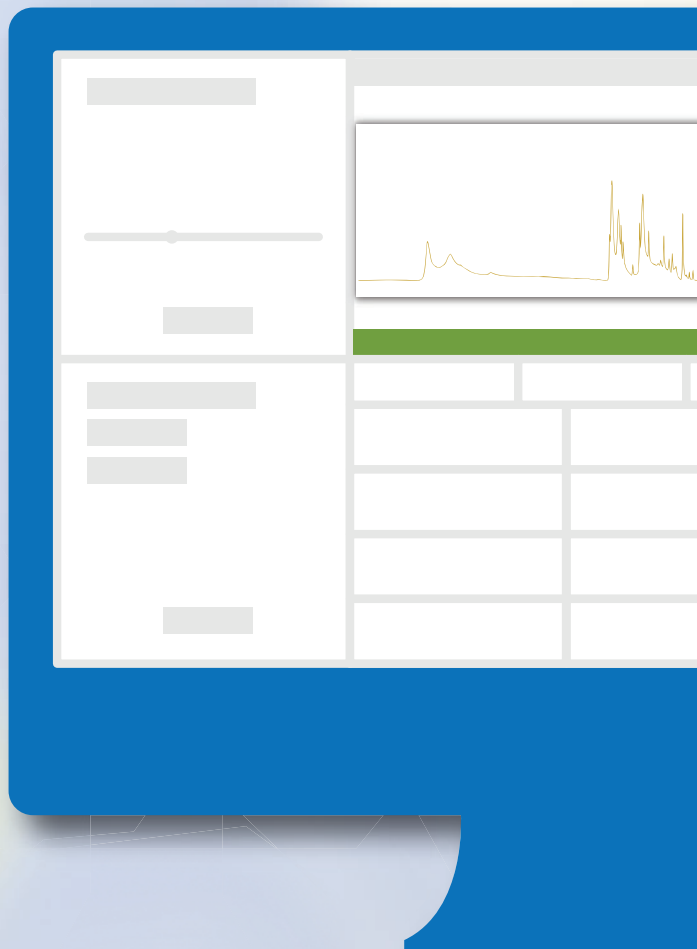
Fastest Search

Spectral search optimized for speed and performance



Highest Quality

Spectra measured using rigorous protocols for best overall results



Supports multiple types of data in multiple instrument formats!

www.knowitall.com/trial

BIO-RAD



Molecular Spectroscopy Workbench

Stress, Strain, and Raman Spectroscopy

Stress and *strain* are terms that are often used interchangeably when discussing the characteristics of materials. Nevertheless, their meanings are different. *Stress* is a force per unit area applied to an object, and *strain* is the effect on the object from the stress. Specifically, *strain* is the change in the positions of the atoms or the lengths of the chemical bonds within the object that are induced by the application of stress. Here, we discuss the distinction of these terms, and their mathematical forms as applied to crystals. Strain is manifest in Raman spectra through changes in peak position and bandwidth. We present examples of the identification of strain in crystals of several technologically important materials.

David Tuschel

Readers of *Spectroscopy* have often read how stress or strain can be detected by Raman spectroscopy through the shifting or broadening of certain bands. In this installment of “Molecular Spectroscopy Workbench,” we delve more deeply into this topic, discussing the physics and mathematics of stress and strain, and demonstrating their effects on Raman spectra. We begin by carefully defining these two terms, and making the proper distinction between them. Readers interested in a deeper mathematical explanation of stress and strain are encouraged to read the two chapters on these subjects in the classic work by Nye (1).

When external forces are applied to an object that does not move, we say that it is under *stress*. Furthermore, if the forces on the object do not vary spatially, then the object is subject to *homogeneous stress*. Stress normally occurs over an area of an object, and not just a point location. Therefore, stress is properly understood as the force per unit area applied to an object, and is described mathematically by the second rank tensor shown in equation 1, where σ represents stress:

$$\sigma = \begin{bmatrix} \sigma_{xx} & \sigma_{xy} & \sigma_{xz} \\ \sigma_{yx} & \sigma_{yy} & \sigma_{yz} \\ \sigma_{zx} & \sigma_{zy} & \sigma_{zz} \end{bmatrix} \quad [1]$$

We may consider an ideal object such as a cube with the usual x , y , and z axes to better understand the components of the stress tensor. The stress forces applied along the cube’s x , y , or z -axis are said to be the normal components of stress, and are associated with the

tensor elements σ_{xx} , σ_{yy} , and σ_{zz} , respectively. These normal component forces can be applied inward, directed towards the center of the object, or outward. The former is defined as a *compressive stress*, whereas the latter is a *tensile stress*. The sign convention that has been adopted is that a positive value of σ_{xx} , σ_{yy} , or σ_{zz} corresponds to a tensile stress, whereas a negative value indicates a compressive stress. Now, it is important to understand and appreciate that the stress forces applied to opposite faces of our ideal cube must be of equal magnitude, but from opposite directions, for our cube to not move. That is why we can describe stress as a static force. The magnitudes of the stress forces need not be the same on the x , y , or z faces, but they must be the same on the opposite pair of faces.

The diagonal tensor elements σ_{xx} , σ_{yy} , and σ_{zz} are the *normal components* of stress, whereas all of the other off-diagonal tensor elements such as σ_{xy} , σ_{yx} , and σ_{zy} are the *shear components*. The shear tensor elements are paired under a condition of static equilibrium such that

$$\sigma_{ij} = \sigma_{ji} \quad [2]$$

For example, $\sigma_{xy} = \sigma_{yx}$ would be shear forces perpendicular to the normal component σ_{zz} . In summary, the stress tensor diagonal elements describe the force per unit area as compressive or tensile normal components, and the off-diagonal tensor elements describe the shear unit area forces.

We have thus far discussed the stress tensor with respect to an ideal cubic object. We can now take those principles and begin to apply them to crystals of real chemical compounds or elements, and understand the strain induced in the crystal as a result of the application of the stress. It is critically important to understand how stress and strain differ. *Strain* is the change of the positions of the atoms, or the lengths of the chemical bonds within a crystal that are induced by the application of stress. Thus, for a cubic crystal such as silicon (Si), we can expect that a stress of a given magnitude applied along a crystallographic axis will produce the same degree of strain, whether it is applied along the x , y , or z crystallographic axis. However, for a uniaxial or biaxial crystal where all three crystallographic axes are not identical, the amount of strain induced by a given magnitude of stress will depend on the chemical bonding and forces along a particular crystal axis. Therefore, it is actually the changes in atomic positions and chemical bond lengths commensurate with strain that are detected in the Raman spectrum through the changes in peak position

or band broadening.

The relationship between a homogeneous stress and homogeneous strain as a generalized form of Hooke's Law is given by

$$\epsilon_{ij} = S_{ijkl}\sigma_{kl} \quad [3]$$

where ϵ_{ij} is the strain tensor and s_{ijkl} is the elastic compliance constant of the crystal-line material. The strain tensor is a second rank 3×3 tensor of the same form as the stress tensor shown in equation 1. Therefore, equation 4 consists of nine equations, each with nine components on the right hand side. For example,

$$\begin{aligned} \epsilon_{xx} = & S_{xxxx}\sigma_{xx} + S_{xxxxy}\sigma_{xy} + \\ & S_{xxxz}\sigma_{xz} + S_{xxyx}\sigma_{yx} + S_{xxyy}\sigma_{yy} + \\ & S_{xxyz}\sigma_{yz} + S_{xxzx}\sigma_{zx} + S_{xxzy}\sigma_{zy} + \\ & S_{xxxz}\sigma_{zz} \end{aligned} \quad [4]$$

Of course, there will be eight similar equations for the remaining ϵ_{xy} , ϵ_{xz} , ϵ_{yx} , ϵ_{yy} , ϵ_{yz} , ϵ_{zx} , ϵ_{zy} , and ϵ_{zz} tensor elements. The implication of equations 3 and 4 is that, if even only one component of the stress is nonzero, σ_{yy} for example, all of the strain elements may be nonzero. Consider what

that last statement could mean applied to a rectangular or even cubic crystal. If a uniaxial stress is applied to one face of the crystal, it will stretch in the direction of the applied force, but may also undergo shearing such that the angles between faces may differ from the original 90 degrees. In other words, strain may be induced in a material in a direction other than that of the applied stress.

We have discussed compressive and tensile stress, and so we can now understand the compressive and tensile strain induced in a crystal or material as a result of the application of the corresponding stress forces. If a crystal is subjected to a tensile stress, we can envision the atoms being pulled apart, or chemical bonds lengthened, relative to their normal positions and lengths in an unstressed crystal. As the chemical bond length increases, and the force constant remains the same, we should expect the vibrational frequency to decrease. A shift of the Raman peak position to lower frequencies is exactly what is observed from materials that have been subjected to a tensile stress. Conversely, if a compressive

FlexiSpec® fiber probes enable to monitor chemical reactions in-line & to run medical diagnostics in-vivo using all the key spectroscopy methods: ATR-absorption, diffuse reflection, Raman, fluorescence or their any combinations.

**UNIQUE
FIBER PROBES**

**FOR PROCESS
SPECTROSCOPY**

& MEDICAL DIAGNOSTICS

IN A BROAD 0.3-16 μm RANGE



sive stress is applied, we would expect the atoms in a crystal to move closer together, or the chemical bond lengths to be shortened, relative to their normal positions and lengths in an unstressed crystal. The resulting compressive strain in the crystal results in Raman peak positions shifted to higher frequencies. The lesson to be learned here is that compressive and tensile stresses will induce corresponding strains in the crystal that can be observed as shifts of a Raman peak position to higher or lower frequencies, respectively. The magnitude of the Raman peak shift will be commensurate with that of the stress and corresponding strain induced in the material. The degree to which the Raman band will shift is dependent on the specific material under examination and the elastic compliance constant (s_{ijkl}) of that chemical compound or element, and the specific crystallographic axes being probed.

As you can see, the stress-strain tensor relationship in even the most simple crystal structures can be complex. Nevertheless, quantitative analysis of stress or strain by Raman spectroscopy has been performed on a variety of materials, including silicon (2–7), aluminum oxide (8–10), barium titanate (11–12), and aluminum nitride (13). Now that we have reviewed the fundamental physics of stress and strain, we can examine how they affect the Raman spectra in various technologically important materials.

Imaging Strain in Polysilicon

Much of the early work on microRaman spectroscopy of semiconductors involved the characterization of polycrystalline silicon (14–17), also known as polysilicon, which is still used extensively in fabricated electronic devices. Theoretical and experimental work was directed towards an understanding of how strain, microcrystallinity, and crystal lattice defects or disorder can all affect the Raman band shape, position, and scattering strength of single and polycrystalline silicon (18–20). The presence of nanocrystalline silicon in polysilicon was confirmed through the combination of transmission electron microscopy and Raman spectroscopy, and the effects of extremely small silicon grain dimensions on the Raman spectra were attributed to phonon confinement (21–24). As the crystalline grain size becomes smaller, comparable to

the wavelength of the incident laser light or less, the Raman band broadens and shifts relative to that obtained from a crystalline domain significantly larger than the excitation wavelength. This has been explained in part by phonon confinement, in which the location of the phonon becomes more certain as the grain size becomes smaller, and therefore the energy of the phonon measured must become less certain consistent with the Heisenberg uncertainty principle.

It is important to understand the effects of nanocrystallinity on the Raman spectrum, so as not to wrongly attribute the spectral features of nanocrystals to strain in microcrystalline or larger grain sizes. Of course, strain can be present in nanocrystalline materials. If that is the case, then one will not be able to strictly differentiate the combined effects of strain and nanocrystallinity on the Raman spectrum.

A collection of data from a polysilicon test structure is shown in Figure 1. A reflected white light image of the structure appears in the lower right hand corner, and a Raman image corresponding to the central structure in the reflected light image appears to its left. The plot on the upper left consists of all of the Raman spectra acquired over the image area and the upper right hand plot is of the single spectrum associated with the cursor location in the Raman and reflected light images. The Raman data were acquired using 532 nm excitation and a 100x Olympus objective and by moving the stage in 200 nm increments over an approximate area of 25 μm x 25 μm . In this particular case, the Raman image is rendered through a color coded plot of Raman signal strength of the corresponding color bracketed Raman shift positions in the two upper traces.

Raman spectra of the unstrained substrate silicon, microcrystalline and strained polycrystalline silicon, and nanocrystalline silicon are shown in Figure 2. The substrate silicon spectrum consists of the Raman band at 521 cm^{-1} arising from the first order optical phonon at the Brillouin zone center. The Raman band in the spectrum of microcrystalline polysilicon appears at 515 cm^{-1} , a shift of -6 cm^{-1} relative to the peak position of the unstrained substrate silicon, thereby indicating the presence of tensile strain. The increased width of the polysilicon silicon Raman band indicates that there is a distribution of strains, and

the band shift is not the result of a single uniaxial stress. The shoulder at 521 cm^{-1} can be attributed to the substrate silicon underlying the polycrystalline silicon film. The spectrum of nanocrystalline silicon manifests substantial broadening with the peak centered at 502 cm^{-1} . As a result, the substrate silicon signal at 521 cm^{-1} is now better resolved. The substantial broadening and peak center shift of approximately -19 cm^{-1} are consistent with phonon confinement associated with crystal grain sizes with nanometer dimensions. Of course, the nanocrystalline silicon can also be strained, but the effects of strain cannot be differentiated from those of nanocrystallinity in the Raman spectrum.

With respect to our explanation of the Raman spectra in Figure 2, we now discuss the reasoning behind our choice of the color-coded brackets to render the Raman image, and how they relate to differences in the solid-state structure of silicon. If we were to have a merely elemental compositional image of this particular structure, we would expect it to be entirely uniform without spatial variation, because silicon would appear in every pixel of the image. However, if we distinguish the different solid-state structures of the silicon by identifying unstrained silicon with the Brillouin zone center Raman band of 520.7 cm^{-1} isolated in red brackets, microcrystalline and strained polycrystalline silicon in green brackets, and a distribution of nanocrystallinity and strain in the blue brackets, we can render the Raman image in the lower left hand corner. To some degree strain, microcrystallinity, and nanocrystallinity are comingled in the polysilicon regions of our images; however, we can make a reasonable distinction by attributing the blue regions as primarily due to nanocrystalline grain size.

Now we consider what our rendering reveals in the Raman image, expanded for more detailed examination in Figure 3. The red regions consist of either substrate silicon or grown single crystal silicon with different oxide thicknesses. The spatial variation of the single crystal Raman signal strengths corresponds precisely with the physical optical effects of the oxide thicknesses and even small contaminants or defects seen in the reflected light image. Furthermore, because of the thinness of the polysilicon A alone, one can see through the green polysilicon A component to the underlying

ing red substrate silicon, particularly on the left and right of the upper and lower portions of Figure 3. The spatial variation of the microcrystalline and strained polycrystalline silicon green component signal strength corresponds to both the central strip consisting of polysilicon B deposited on polysilicon A and the granular variation of polysilicon A seen in the reflected light image. Note that the polysilicon A bright green speckles in the Raman image correspond precisely to black speckles in the reflected light image. Careful examination of the central strip reveals these same speckles in the polysilicon A blurred somewhat by the polysilicon B deposited on top of it.

Now let's turn our attention to the appearance of nanocrystalline silicon in the image. The formation of nanocrystalline silicon occurs almost exclusively in polysilicon A and only on top of the central single crystal silicon structure, and not the substrate silicon. Note that the nanocrystallinity occurs primarily along the edge of the polysilicon A, but is absent as the polysilicon A continues along the silicon substrate. Also, we see that some of the polysilicon A

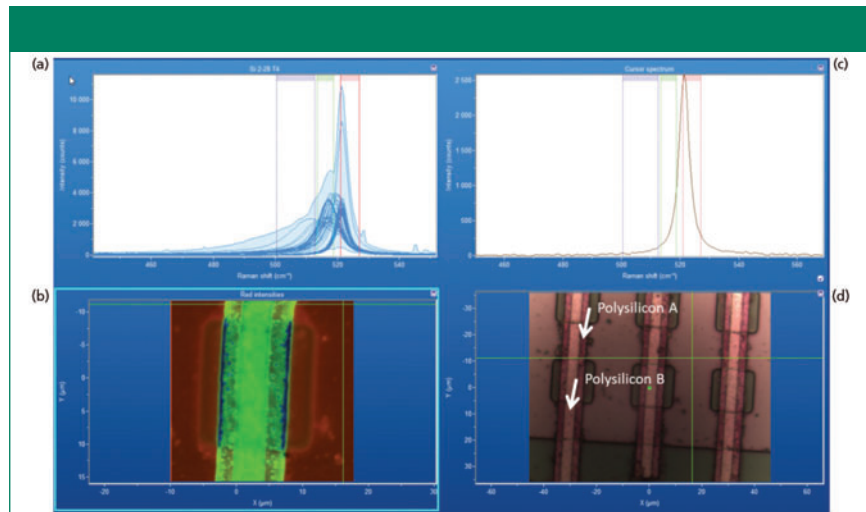


Figure 1: (a) Raman hyperspectral data set from a polysilicon test structure with (d) white reflected light image in lower right corner; (b) a Raman image generated from the spatially varying signal strengths between the color coded brackets in the spectral traces; (c) the single spectrum corresponding to the cross hairs in the Raman and white reflected light images.

speckles appear blue, thereby revealing nanocrystallinity over the central structure but not over the silicon substrate.

In summary, the intensity variations of the single crystal silicon comport with the

physical optical effects of varying oxide film thickness and surface contaminants. Also, this Raman image reveals the spatially varying nanocrystallinity, microcrystallinity and strain in polysilicon. We can infer



EXTENDING RAMAN Into the THz Domain



ONDAX is now Coherent, Inc.

Our patented **THz-Raman® Spectroscopy Systems** combine chemical detection and structural analysis in a single instrument. By improving both process and scientific analysis, this cost-effective technology delivers faster and more reliable results. Coherent now offers a full line of THz-Raman® products and high-performance lasers for your most challenging process or research spectroscopy applications.

Learn More—www.THz-Raman.com



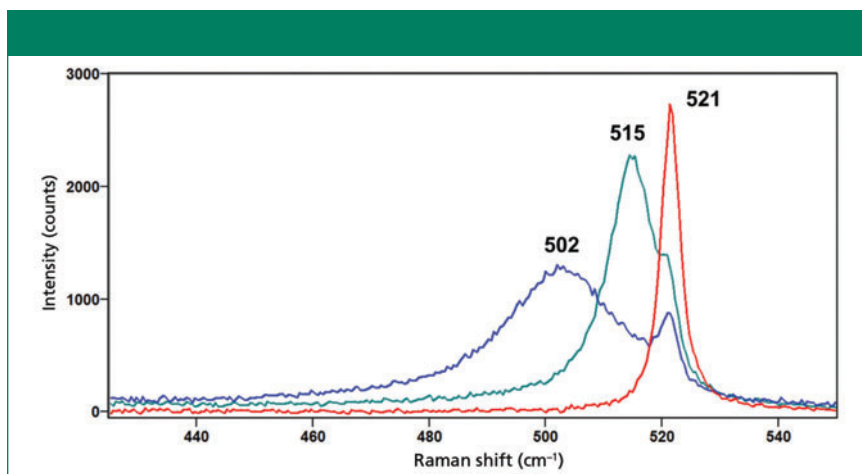


Figure 2: Raman spectra of the substrate silicon (red), microcrystalline and strained polycrystalline silicon (green), and nanocrystalline silicon (blue).

that these structural differences occur either as a result of processing conditions, or from interactions with the adjacent or underlying materials in which the polysilicon is in contact. The use of narrow colored brackets with our hyperspectral mapping data set allows one to differentiate strain free, strained microcrystalline, and nanocrystalline silicon and to render an image of these spatially varying solid state structures.

Strain in Diamond

The fabrication of diamond films by chemical vapor deposition (CVD) has been under development for many years now for applications including hardened surfaces, optical windows, and electrodes. The solid-state structure of these films has a direct impact on the material properties and therefore figures of merit of the final product. Crystallinity, single or poly, the number of defects, strain, and even crystal face, can affect performance. Furthermore, the uniformity of such films can affect the overall utility of the final product. Therefore, analytical methods are called for that can characterize the spatially varying structure of CVD diamond films.

To that end, we have made use of Raman polarization selection rules for the purpose of simply differentiating single from polycrystalline diamond, and to probe the extent of lattice defects, spatially varying strain, and the degree of disorder present in a crystal. We have applied polarization-orientation (P-O) Raman spectroscopy to characterize diamond films for crystallinity and strain. The reader is referred to a previous publication on P-O Raman spectroscopy

to understand the theory and practical applications of this method (25).

The CVD films consisted of diamond clusters whose edge lengths ranged from approximately 5 μm to 15 μm . The faces of the diamonds are square and triangular and presumably correspond to the (100) and (111) faces, respectively. We performed P-O Raman spectroscopy on the isolated square faces for the characterization of CVD diamond crystallinity. A reflected light image of one such square face from which P-O microRaman spectra were obtained is shown in Figure 4.

We obtained P-O Raman spectra of diamond films prepared by chemical vapor deposition using a 1.6 mW, 488.0 nm laser beam focused to a 0.6 μm diameter with an Olympus MS Plan 100 (0.95 NA) objective. Raman scattered light was collected using the same microscope objective (backscattering configuration). An analyzer was placed in front of the spectrometer entrance slit, and configured either parallel or perpendicular to the incident polarization. Individual spectra were collected at 5° rotational increments for each analyzer polarization configuration as the sample is then rotated within the focal plane. The sensitivities of the microscope and spectrometer to the two, orthogonal polarizations were characterized against a depolarized white light source. Accordingly, corrections were made to the intensities of P-O Raman spectra obtained at the corresponding polarizations.

The P-O Raman spectra shown in Figure 5 indicate that the diamond is a single crystal that contains substantial

defects. The orientational dependence of the Raman spectra manifest the expected sinusoidal response for a single crystal diamond rotated in a (100) plane with the parallel and perpendicular P-O spectral plots 45° out of phase with each other. However, the failure of the signal to vanish at the minima and the presence of an amorphous carbon band at approximately 1560 cm^{-1} invariant with orientation reveal considerable defects in what is nominally a single crystal of diamond.

In addition to the defect-induced disorder manifest in the spectra, crystal orientation dependent strain can be identified through band fitting. The strain-free Raman band of diamond appears at 1333 cm^{-1} . Previous work by other authors has demonstrated the crystallographic orientational variation of strain in diamond films and the use of polarized Raman spectroscopy to detect it (26–28). Figure 6 shows two Raman spectra from the perpendicular polarization set (Figure 5) separated by 5 rotational degrees. Band fitting reveals a strain-free component at 1333 cm^{-1} , and a second component at 1341 cm^{-1} , thereby indicating the presence of compressive strain. Note that the relative contributions of the strain-free to strained components of the diamond Raman band are inverted, even though the crystal has been rotated by only 5°. Indeed, the 3D variation of the strain in this crystal contributes significantly to the deviation of the experimentally obtained P-O diagram from one calculated for an ideal crystal. Were the diamond to be free of defects and spatially varying strain, we would expect the Raman signal strengths to be zero at the minima in the P-O plots shown in Figure 5.

Strain in Two-Dimensional Molybdenum Disulfide

There is a great need for characterization of two-dimensional (2D) transition metal dichalcogenide crystals because of their experimental nature and structural variability, often within one film. We have discussed the resonance Raman and photoluminescence spectroscopy and imaging of few-layer molybdenum disulfide previously (29). The spatial variation of the number of atomic layers of 2D crystals can often be inferred from the hue or color of the crystal when viewed using reflected white light microscopy, and so there have been develop-

ments to use optical microscopy to rapidly identify the number of stoichiometric layers that make up the 2D crystal (30). However, spatially varying strain in 2D crystals does not manifest itself in reflected white light images. In this article, we focus on spatially varying strain in exfoliated and chemical vapor deposition molybdenum disulfide revealed by Raman spectroscopy.

Several spectra and a Raman image of a large exfoliated molybdenum disulfide few-layer flake, and a smaller flake nearby, are shown in Figure 7. The Raman data were acquired using 532 nm excitation and a 100x Olympus objective and by moving the stage in 300 nm increments. The Raman image is a rendering of signal strength for a particular Raman band as a function of position on the sample. In this case, the Raman image is rendered through red corresponding to the Raman band of substrate silicon at 521 cm^{-1} , and green is associated with the Raman signal of the molybdenum disulfide A_{1g} band at 408 cm^{-1} .

Most of the large flake is strain free; however, substantial tensile strain is present along a portion of the perimeter. Raman spectroscopy is most useful for identifying spatially varying and heterogeneous strain through the broadening and shifting of bands relative to those from areas free of strain. Here, the broadening and the shifting to lower wavenumber by 4 cm^{-1} of the E_{2g}^1 and A_{1g} bands indicate the presence of tensile strain in the small flake and at the perimeter of the large flake. An interesting observation is that, very often, the structure of the perimeter of a few-layer molybdenum disulfide flake is quite different from that of the interior manifesting differences in both Raman scattering and photoluminescence.

Strain is frequently observed at the perimeters of exfoliated molybdenum disulfide few-layer flakes. It can also be detected at the perimeters and interfaces of 2D crystals grown by chemical vapor deposition. A collection of hyperspectral data and the corresponding Raman image from primarily single-layer molybdenum disulfide crystals grown on a silicon substrate are shown in Figure 8. The Raman data were acquired using 532 nm excitation and a 50x Olympus objective and by moving the stage in $1\text{ }\mu\text{m}$ increments over an area of approximately $120\text{ }\mu\text{m} \times 90\text{ }\mu\text{m}$. The spectra consist primarily of the E_{2g}^1 (382 cm^{-1}) and A_{1g} (402 cm^{-1}) molybdenum disulfide

bands, and the first order optical phonon from silicon at 521 cm^{-1} . A reflected white light image of the sample area appears in the lower right hand corner, and a Raman image corresponding to the reflected light image appears to its left. The large triangular features in the white light image are single-layer molybdenum disulfide crystals, and the surrounding lighter area is the silicon substrate. The small dark area at the center of the upper triangle is two-layer molybdenum disulfide. The plot on the upper left consists of all of the Raman

spectra acquired over the image area. The upper right hand plot is of the single spectrum associated with the cross hair location in the Raman and reflected light images; the line cursor is positioned at the E_{2g}^1 peak of strain-free molybdenum disulfide to reveal the strain at the cross hair location. The presence of shear E_{2g}^2 (21.2 cm^{-1}) and inter-layer breathing B_{2g}^2 (37.5 cm^{-1}) bands in the hyperspectral data set (upper left of Figure 8) from the small dark area confirms that it is two-layer molybdenum disulfide (31). These low frequency bands are absent



All New NanoRam[®]-1064 Handheld Raman for Nondestructive Raw Material ID & Verification

Minimizes fluorescence to effectively identify many more materials, even those with color in the lab, warehouse, and loading dock

On-board automated method validation

Learn More About the NanoRam-1064

www.bwtek.com/Nanoram1064

+1-302-368-7824

marketing@bwtek.com

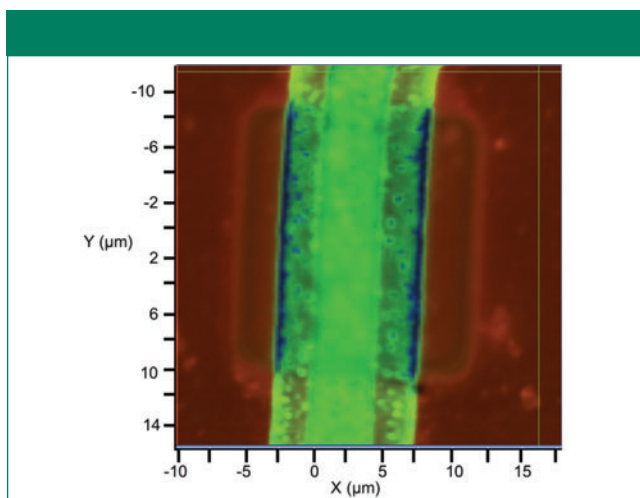


Figure 3: The Raman image from Figure 1b. Red corresponds to single crystal silicon, green to microcrystalline and strained polysilicon, and blue to nanocrystalline silicon. Polysilicon B (in the center) was deposited on the wider, underlying polysilicon A.

in the spectra of single-layer molybdenum disulfide.

The red Raman image in the lower left of Figure 8 corresponds to the E_{2g}^1 (382 cm^{-1}) molybdenum disulfide band between the red brackets seen in the plot in the upper left. The Raman image is a rendering of signal strength between the brackets as a function of position on the sample. In this particular case, the red brackets have been made narrow, and placed around the E_{2g}^1 (382 cm^{-1}) band as it appears in the interior of the crystal away from both the perimeter and crystal interfaces. Narrowing the brackets allows them to function as a spectral slit in the image generation; Raman bands that shift to lower or higher frequency will manifest decreased intensity as less of the band will appear between the narrow brackets. Consequently, areas of strain will show diminished signal strength and appear darker in the Raman image, because the Raman band has shifted to either lower or higher frequency depending on whether the strain is tensile or compressive, respectively.

We need to carefully examine the spectra from the Raman map in Figure 8 to understand how the narrow brackets function as a spectral slit to reveal strain and even the two-layer molybdenum disulfide in the Raman image. Representative spectra of the interior single-layer molybdenum disulfide, perimeter, strained crystal interface, and dark two-layer molybdenum disulfide are shown in Figure 9. The Raman spectrum of the interior single-layer molybdenum disulfide free of strain consists of the E_{2g}^1 (381.6 cm^{-1}) and A_{1g} (402.1 cm^{-1}) bands. The Raman spectrum of the dark two-layer molybdenum disulfide consists of the E_{2g}^1 (379.9 cm^{-1}) and A_{1g} (403.3 cm^{-1}) bands having peak positions -1.7 cm^{-1} and $+1.2\text{ cm}^{-1}$, respectively, relative to those of the single-layer molybdenum disulfide. The increased separation of the E_{2g}^1 and A_{1g} bands, along with the aforementioned presence of the low frequency bands, confirms that the small dark area in the upper triangle is two-layer molybdenum disulfide. The E_{2g}^1 (381.4 cm^{-1}) and A_{1g} (401.4 cm^{-1}) bands in the spectrum of the perimeter have shifted to -0.2 cm^{-1} and -0.7 cm^{-1} , respectively, thereby indicating the presence of a tensile strain at the perimeter. The E_{2g}^1 (382.9 cm^{-1}) and A_{1g} (402.7 cm^{-1}) bands in the spectrum of the strained crystal

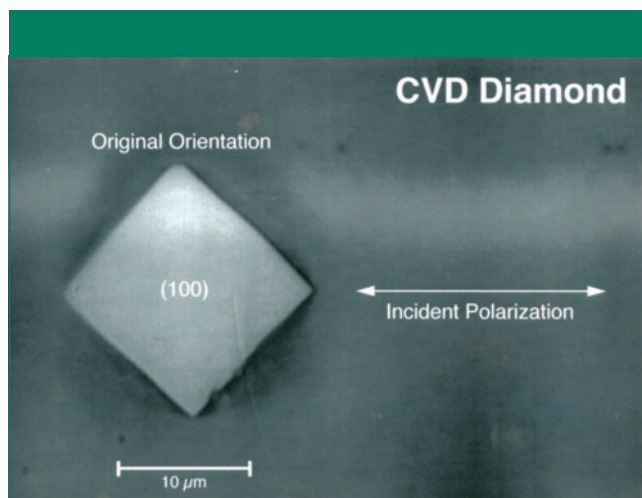


Figure 4: Reflected white light image of diamond prepared by chemical vapor deposition from which P-O microRaman spectra were obtained.

interface (the dark areas between the crystals) have shifted to $+1.3\text{ cm}^{-1}$ and $+0.6\text{ cm}^{-1}$, respectively, thereby indicating the presence of a compressive strain. The E_{2g}^1 band shift is twice that of the A_{1g} band and so the selection to bracket the E_{2g}^1 band makes it a better choice for revealing spatially varying strain at the crystal interfaces in the Raman image.

Now we consider what our rendering reveals in the Raman image expanded for more detailed examination in Figure 10. We choose a single spectral component color image with spectrally narrow brackets to reveal the spatially varying strain associated with the chosen Raman band. In this particular case, the red brackets have been made narrow, and placed around the E_{2g}^1 (382 cm^{-1}) band as it appears in the interior of the crystal away from both the perimeter and crystal interface. Using a narrow bracket allows it to function as a spectral slit in the image generation, thereby differentiating the strain-free single-layer molybdenum disulfide from the strained areas, as well as the two-layer molybdenum disulfide. As explained above, areas of strain appear darker in the Raman image because the band has shifted and contributes less signal strength within the narrow spectral brackets. The spectra in Figure 9 revealed the compressive strain at the interfaces of the triangular molybdenum disulfide crystals where the E_{2g}^1 band has shifted by as much as $+1.3\text{ cm}^{-1}$. Consequently, the Raman image of the adjoining single-layer molybdenum disulfide crystals appears darkest precisely at the interfaces where the crystals met upon their individual growth. Note that the darkness at the interfaces projects diffusely for micrometers into the crystal, thereby revealing the projection of spatially varying and diminishing strain at some distance from the interface into the interior of the crystal. Of course, the spatially varying strain seen in the Raman image is not detected in the reflected white light image. Raman imaging has revealed a distribution of strain in the crystals that could not have been known based upon the appearance of the reflected white light image.

Another collection of hyperspectral data and the corresponding Raman image of single-layer, two-layer and three-layer molybdenum disulfide crystals grown on a silicon substrate are shown in Figure 11. The triangle in the center of the reflected white light image (lower right) consists of spatially varying two-layer, and

three-layer molybdenum disulfide, the pink circle surrounding the triangle is single-layer molybdenum disulfide, and the area outside of the circle is the bare silicon substrate. The red Raman image in the lower left of Figure 11 corresponds to the spatially varying signal strength of the E_{2g}^1 (382 cm^{-1}) molybdenum disulfide band between the red brackets seen in the spectral plots. The plot on the upper right is of the single spectrum associated with the cross hair location at the interface of the multi-layer triangle and single-layer molybdenum disulfide; note the splitting of the A_{1g} band.

We examine the spectra from the Raman map in Figure 11 to understand the basis for the contrast between the single-layer molybdenum disulfide and the spatially varying two- and three-layer molybdenum disulfide triangle and the bright interface around the multilayer molybdenum disulfide triangle in the Raman image. Representative spectra of the single-layer molybdenum disulfide, triangle and single-layer molybdenum disulfide interface, and three-layer molybdenum disulfide are shown in Figure 12. The Raman spectrum

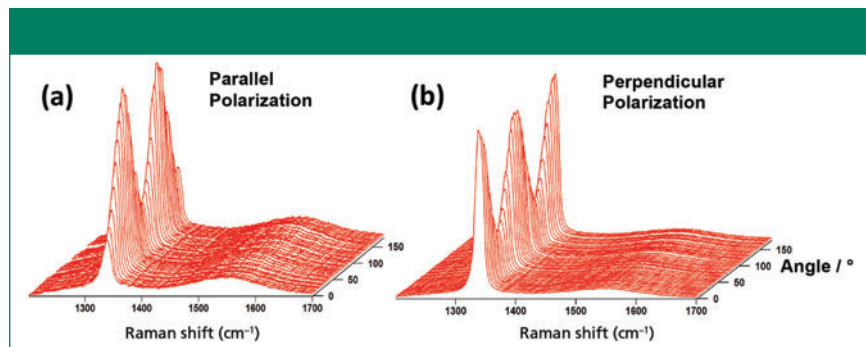


Figure 5: P-O Raman spectra of a (100) face of the CVD diamond shown in Figure 4. The light collection analyzer was oriented (a) parallel and (b) perpendicular to the incident polarization.

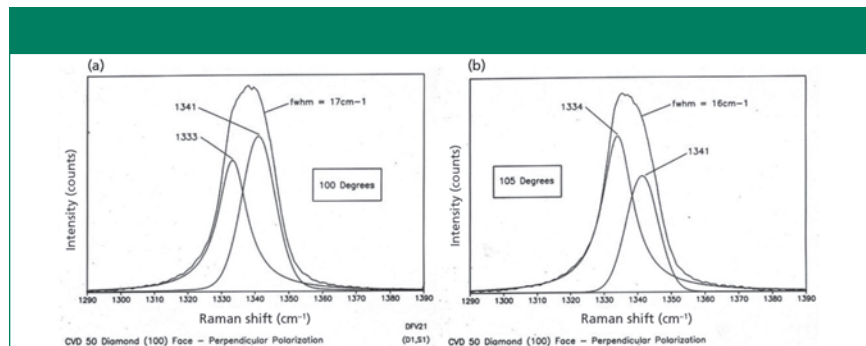
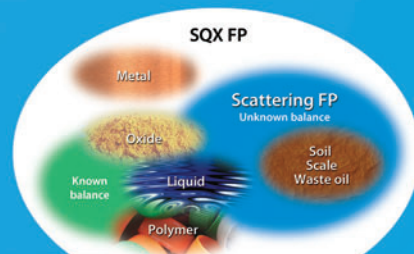


Figure 6: P-O Raman spectra separated by 5 rotational degrees for (a) versus (b). The spectra are fitted for strain-free diamond ($\sim 1333\text{ cm}^{-1}$) and a strain component.

ZSX Primus III+

HIGH PERFORMANCE WDXRF

- Tube-above optics for superior reliability
- Analysis of elements from O to U
- High precision sample positioning
- SQX fundamental parameters software



Rigaku Corporation and its Global Subsidiaries
website: www.Rigaku.com | email: info@Rigaku.com



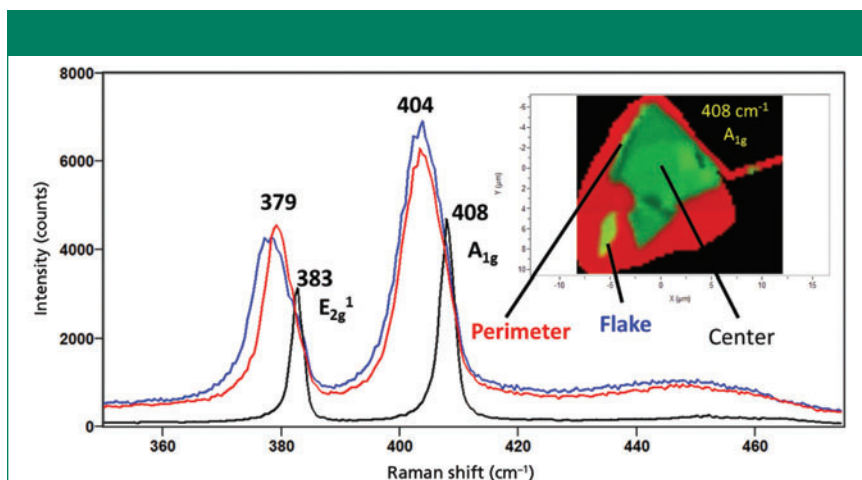


Figure 7: Raman spectra of few-layer molybdenum disulfide from different locations on the two flakes shown in the inset Raman image. The spectrum from the center is not strained. Note the substantial shifts and broadening corresponding to strain in the perimeter and flake spectra.

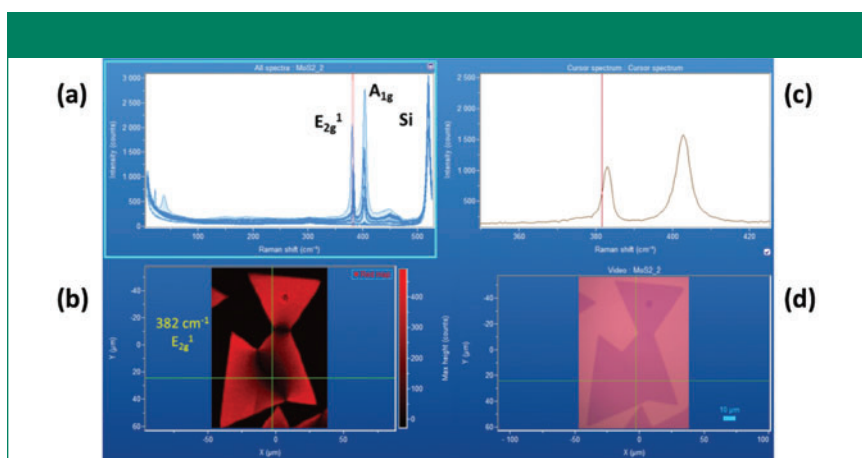


Figure 8: (a) Raman hyperspectral data set from molybdenum disulfide grown on silicon with (d) white reflected light image in lower right corner. (b) Raman image generated from the spatially varying signal strengths between the red brackets in the hyperspectral plot. (c) The single spectrum corresponding to the cross hairs in the Raman and white reflected light images; the line cursor is positioned at the E_{2g}^1 peak of strain-free MoS_2 .

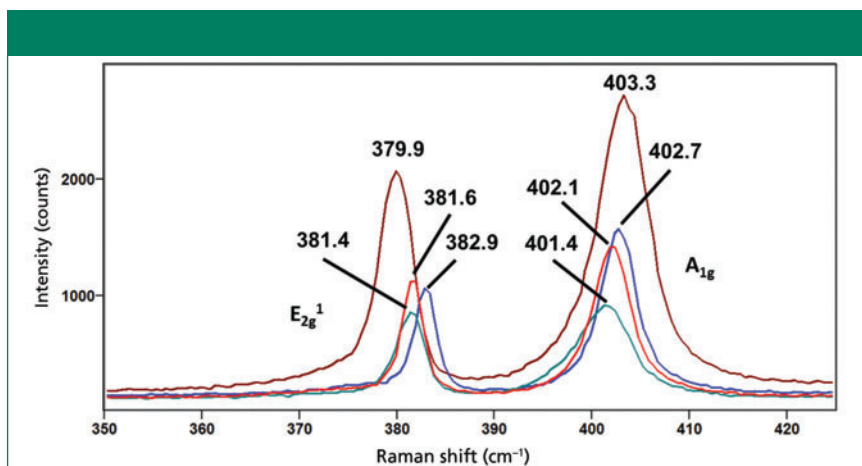


Figure 9: Raman spectra obtained from different locations of sample shown in Figure 8: Interior single-layer molybdenum disulfide (red), perimeter (green), strained crystal interface (blue), and dark two-layer molybdenum disulfide (brown).

of the single-layer molybdenum disulfide free of strain consists of the E_{2g}^1 (382.1 cm^{-1}) and A_{1g} (402.3 cm^{-1}) bands. The Raman spectrum of the triangular three-layer molybdenum disulfide consists of the E_{2g}^1 (378.2 cm^{-1}) and A_{1g} (404.1 cm^{-1}) bands having peak positions -3.9 cm^{-1} and $+1.8 \text{ cm}^{-1}$, respectively, relative to those of the single-layer molybdenum disulfide. The increased separation of the E_{2g}^1 and A_{1g} (-3.9 cm^{-1} and $+1.8 \text{ cm}^{-1}$) bands relative to the separation of the two-layer molybdenum disulfide in Figure 9 (-1.7 cm^{-1} and $+1.2 \text{ cm}^{-1}$) confirms that the area of the triangle from which this spectrum was generated is three-layer molybdenum disulfide. Further support for this interpretation is how much broader the E_{2g}^1 and A_{1g} bands in the spectrum of three-layer molybdenum disulfide are relative to their counterparts in the two-layer molybdenum disulfide spectrum. The shift of the E_{2g}^1 band to lower wavenumber away from the narrow brackets centered at 382.1 cm^{-1} is the basis for the diminished signal strength and dark appearance of the spatially varying two-layer and three-layer molybdenum disulfide triangle.

The interface of the spatially varying two-layer and three-layer molybdenum disulfide triangle adjoining the single layer molybdenum disulfide presents a structurally different case from the crystal interface of the single-layer molybdenum disulfide crystals that have grown to meet each other. Here, we see a splitting of the A_{1g} band. The E_{2g}^1 (381.5 cm^{-1}) and A_{1g} (402.6 and 406.6 cm^{-1}) bands in the spectrum of the triangle and single-layer molybdenum disulfide interface have shifted to -0.6 cm^{-1} and $(+0.3 \text{ cm}^{-1}$ and $+4.3 \text{ cm}^{-1})$ which is very different from either the perimeter or strained crystal interface spectra in Figure 9. The spectral interpretation at this interface is not as straightforward, because of the convolution of the multilayer and single layer molybdenum disulfide signals within the same spectrum. We may interpret the E_{2g}^1 (381.5 cm^{-1}) and A_{1g} (402.6 cm^{-1}) bands at the crystalline interface as consistent with a transition from the single-layer to two-layer molybdenum disulfide. However, the second A_{1g} (406.6 cm^{-1}) band is substantially shifted, $+4.3 \text{ cm}^{-1}$, relative to the single-layer molybdenum disulfide A_{1g} (402.3 cm^{-1}) band, thereby indicat-

ing a compressive strain at the interface.

The symmetry species and the directions of the atomic motions of the phonon modes affected by stress can help us to understand the differences observed in the images and spectra of Figures 8–12. The E_{2g}^1 band arises from in plane (xy -axes) atomic motions whereas the A_{1g} band is associated with vibrations along the z -axis (31). Therefore, these bands will be sensitive to strain in orthogonal directions in the crystal, the doubly degenerate E_{2g}^1 band in the xy -plane and the A_{1g} band along the z -axis (32–33). The large shift of $+4.3\text{ cm}^{-1}$ for the second A_{1g} band in the spectrum of the triangle multilayer–single-layer molybdenum disulfide interface is indicative of a significant compressive strain along the z -axis, whereas there is no indication of strain in the xy -plane based upon the peak position of the E_{2g}^1 band. This is quite different from the interfaces created by the growth of single-layer molybdenum disulfide crystals meeting each other. In the case of the contiguous single-layer molybdenum disulfide crystals, the E_{2g}^1 and A_{1g} bands in the spectrum of the strained crystal interface (the dark area between the crystals) have shifted by as much as $+1.3\text{ cm}^{-1}$ and $+0.6\text{ cm}^{-1}$, respectively, thereby indicating the presence of a compressive strain in the xy -plane and along the z axis. In contrast, a compressive strain of far greater magnitude appears only along the z -axis at the triangle multilayer–single-layer molybdenum disulfide interface.

Conclusion

Stress and strain were defined, and a mathematical description of their relationship was provided, making the proper distinction between the two terms. *Stress* is a force per unit area applied to an object, and *strain* is the effect on the object from the stress. Specifically, *strain* is the change in the positions of the atoms, or the lengths of the chemical bonds within the object that are induced by the application of stress. Compressive and tensile stresses will induce corresponding strains in the crystal, which can be observed as shifts of a Raman peak position to higher or lower frequencies, respectively. The magnitude of the Raman peak shift will

be commensurate with that of the stress and corresponding strain induced in the material. The degree to which the Raman band will shift is dependent upon the specific material under examination, the elastic compliance constant (s_{ijkl}) of that chemical compound or element, and the specific crystallographic axes being probed.

Raman spectroscopy is sensitive to strain, and has therefore been successfully used for the characterization of strain in materials. Raman spectra of

the unstrained substrate silicon, microcrystalline and strained polycrystalline silicon, and nanocrystalline silicon from a silicon device test structure were presented and formed the basis of a Raman image. The Raman image of the test structure revealed the spatially varying nanocrystallinity, microcrystallinity and strain in polysilicon. Strain was also identified in diamond films prepared by chemical vapor deposition. We have applied polarization-orientation Raman spectroscopy to characterize diamond

Spectroscopy Sampling Solutions



IRIS

New Diamond ATR

Featured Product

IRIS ATR — See the possibilities

The IRIS accessory is the go-to diamond ATR for every lab. It is designed to make IR sampling easy. You can expect high-quality spectra covering a wide range of samples from powders, gels, liquids, solids and more. It is ideal for research, QA/QC and sample identification.

The backbone of the IRIS is its high-precision optics. IRIS' powered mirrors have been designed and processed using diamond-turning technology to achieve optimal performance. All mirrors are gold-coated for maximum reflectivity.

The diamond ATR crystal, with a diameter of 2 mm, offers the ultimate sampling

surface for most all samples. It provides extreme hardness, and is suitable for testing samples with pH between 1–14. The unique inert PTFE sealing method of the diamond ATR element in the stainless-steel mounting plate adds to IRIS' universal applicability for the analysis of a wide range of organic and caustic samples.

PIKE Technologies is a primary source for spectroscopy accessories worldwide. Products include attenuated total reflection (ATR), diffuse reflection, specular reflection, integrating spheres, polarizers, a complete line of transmission sampling accessories and more.

Contact PIKE today to learn more.

PIKE (608) 274-2721
TECHNOLOGIES www.piketech.com
info@piketech.com

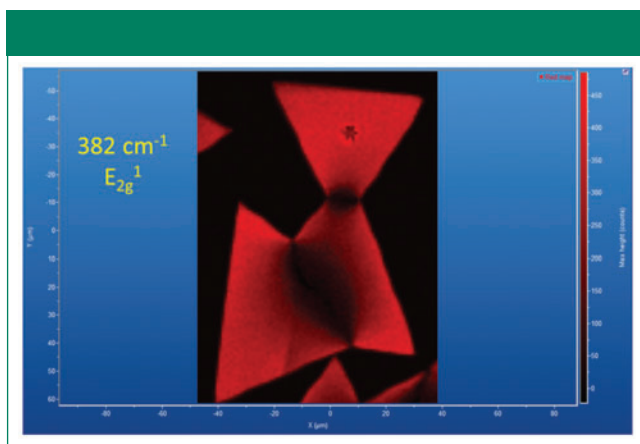


Figure 10: The Raman image from Figure 8b. Red corresponds to the narrow bracketed E_{2g}^1 band centered at 381.6 cm^{-1} . The interfacial areas appear dark because the E_{2g}^1 band has shifted to higher wavenumber due to compressive stress.

films for crystallinity and strain. Band fitting reveals a strain-free component at 1333 cm^{-1} and a second component at 1341 cm^{-1} , thereby indicating the presence of compressive strain.

Lastly, we discussed spatially varying strain in exfoliated and chemical vapor deposition molybdenum disulfide revealed by Raman spectroscopy. Most of the exfoliated flake is strain free; however, substantial tensile strain is present along a portion of the perimeter. Raman spectroscopy is useful for identifying

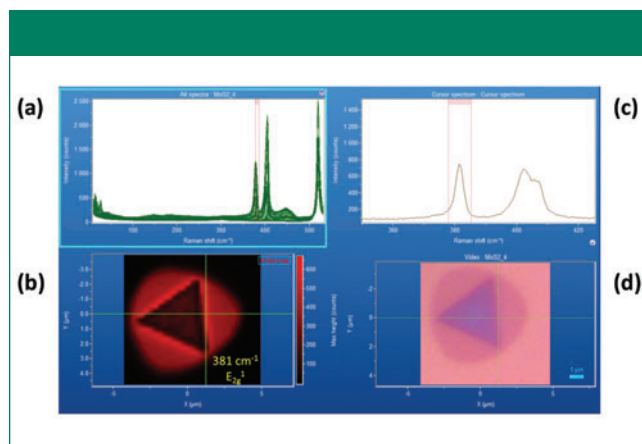


Figure 11: (a) Raman hyperspectral data set from molybdenum disulfide grown on silicon with (d) white reflected light image in lower right corner. The Raman image (b) was generated from the spatially varying signal strengths between the red brackets in the spectral plots. (c) The single spectrum corresponds to the cross hairs in the Raman and white reflected light images.

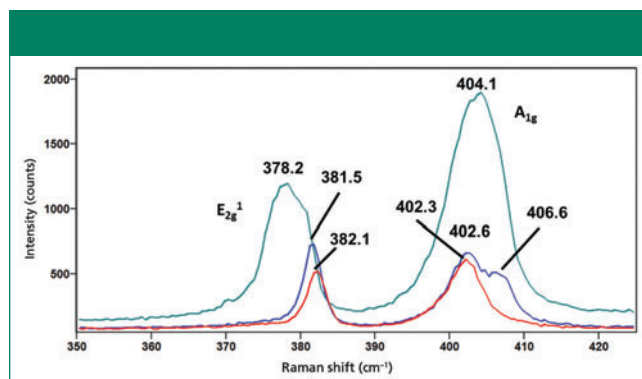


Figure 12: Raman spectra obtained from different locations of sample shown in Figure 11: Surrounding single-layer molybdenum disulfide (red), triangle and single-layer molybdenum disulfide interface (blue), and three-layer molybdenum disulfide (green).

spatially varying and heterogeneous strain in exfoliated molybdenum disulfide through the broadening and shifting of bands relative to those from areas free of strain. Strain was also detected at the perimeters and interfaces of 2D crystals grown by chemical vapor deposition. The Raman image of adjoining single-layer molybdenum disulfide crystals revealed strain at the interfaces where the crystals met upon their individual growth. The strain projects diffusely for micrometers into the crystal. The strain is greatest at the crystal interface and spatially varies and diminishes at some distance from the interface into the interior of the crystal. Here, the E_{2g}^1 and A_{1g} bands in the spectrum of the strained crystal interface have shifted by as much as $+1.3\text{ cm}^{-1}$ and $+0.6\text{ cm}^{-1}$, respectively, thereby indicating the presence of a compressive strain in the xy -plane and along the z -axis. The spatially varying strain seen in the Raman image is not detected in the reflected white light image. Contrast was observed in a second Raman image between the single-layer molybdenum disulfide and the spatially varying two- and three-layer molybdenum disulfide triangle and the

2019 EASTERN ANALYTICAL SYMPOSIUM & EXPOSITION



**ENHANCING
ANALYTICAL
CHEMISTRY**
WITH SUSTAINABLE SOLUTIONS



eas.org

Crowne Plaza Princeton
Conference Center
Plainsboro, NJ
November 18-20, 2019

**Conveniently located
in Central New Jersey**

**3 Day Technical Program
with 4 Days of Short Courses
and Seminars**

**3 Day Exposition with Access
to Vendors of Analytical
Equipment**

**Workshops and
Employment Bureau**



bright interface around the multi-layer molybdenum disulfide triangle. We interpret the E_{2g}^1 (381.5 cm^{-1}) and A_{1g} (402.6 cm^{-1}) bands at the crystalline interface as consistent with a transition from the single-layer to two-layer molybdenum disulfide. However, the second A_{1g} (406.6 cm^{-1}) band is substantially shifted, $+4.3\text{ cm}^{-1}$, relative to the single-layer molybdenum disulfide A_{1g} (402.3 cm^{-1}) band, thereby indicating a compressive strain at the interface. Compressive strain appears only along the z -axis at the triangle multilayer–single-layer molybdenum disulfide interface. This is quite different from the interface created by the growth of single-layer molybdenum disulfide crystals meeting each other.

References

- (1) J.F. Nye, *Physical Properties of Crystals* (Oxford University Press, 1985), pp. 82–109.
- (2) G.H. Loechelt, N.G. Cave and J. Menendez, *Appl. Phys. Lett.* **66**, 3639–3641 (1995).
- (3) G.H. Loechelt, N.G. Cave, and J. Menendez, *J. Appl. Phys.* **86**, 6164–6180 (1999).
- (4) I. De Wolf, H. Norstrom, and H.E. Maes, *J. Appl. Phys.* **74**, 4490–4500 (1993).
- (5) S.C. Jain, H.E. Maes, K. Pinaridi, and I. De Wolf, *J. Appl. Phys.* **79**, 8145–8165 (1996).
- (6) I. De Wolf, *J. Raman Spectrosc.* **30**, 877–883 (1999).
- (7) T. Miyatake and G. Pezzotti, *J. Appl. Phys.* **110**, 093511 (2011).
- (8) W. Zhu and G. Pezzotti, *Phys. Status Solidi A* **208**, 1141–1150 (2011).
- (9) W. Zhu and G. Pezzotti, *J. Raman Spectrosc.* **42**, 2015–2025 (2011).
- (10) G. Pezzotti and W. Zhu, *Phys. Chem. Chem. Phys.* **17**, 2608–2627 (2015).
- (11) G. Pezzotti, M. Higashino, K. Tsuji, and W. Zhu, *J. Eur. Ceramic Soc.* **30**, 199–204 (2010).
- (12) G. Pezzotti, K. Okai and W. Zhu, *J. Appl. Phys.* **111**, 013504 (2012).
- (13) W. Zhu and G. Pezzotti, *Microelectron. Reliab.* **55**, 66–73 (2015).
- (14) Y. Inoue, S. Nakashima, A. Mitsuishi, T. Nishimura, and Y. Akasaka, *Jpn. J. Appl. Phys.* **25**, 798–801 (1986).
- (15) D. R. Tallant, T. J. Headley, J. W. Medernach, and F. Geyling, *Mat. Res. Soc. Symp. Proc.* **324**, 255–260 (1994).
- (16) D. V. Murphy and S. R. J. Brueck, *Mat. Res. Soc. Symp. Proc.* **17**, 81–94 (1983).
- (17) G. Harbecke, L. Krausbauer, E. F. Steigmeier, A. E. Widmer, H. F. Kapfert, and G. Neugebauer, *Appl. Phys. Lett.* **42**, 249–251 (1983).
- (18) G.-X. Cheng, H. Xia, K.-J. Chen, W. Zhang and X.-K. Zhang, *Phys. Stat. Sol. A* **118**, K51–K54 (1990).
- (19) N. Ohtani and K. Kawamura, *Solid State Commun.* **75**, 711–715 (1990).
- (20) H. Richter, Z. P. Wang, and L. Ley, *Solid State Commun.* **39**, 625–629 (1981).
- (21) Z. Iqbal and S. Veprek, *SPIE Proc.* **794**, 179–182 (1987).
- (22) V. A. Volodin, M. D. Efremov, and V. A. Gritsenko, *Solid State Phenom.* **57–58**, 501–506 (1997).
- (23) Y. He, C. Yin, G. Cheng, L. Wang, X. Liu, and G. Y. Hu, *J. Appl. Phys.* **75**, 797–803 (1994).
- (24) H. Xia, Y. L. He, L. C. Wang, W. Zhang, X. N. Liu, X. K. Zhang, D. Feng, and H. E. Jackson, *J. Appl. Phys.* **78**, 6705–6708 (1995).
- (25) D. Tuschel, *Spectroscopy* **27**(3), 22–27 (2012).
- (26) S.-A. Stuart, S. Prawer, and P.S. Weiser, *Diamond Related Mater.* **2**,

753–757 (1993).

- (27) T. Gries, L. Vandenbulcke, P. Simon, and A. Canizares, *J. Appl. Phys.* **102**, 083519 (2007).
- (28) T. Gries, L. Vandenbulcke, P. Simon, and A. Canizares, *J. Appl. Phys.* **104**, 023524 (2008).
- (29) D. Tuschel, *Spectroscopy* **30**(3) 14–29 (2015).
- (30) H. Li, J. Wu, X. Huang, G. Lu, J. Yang, X. Lu, Q. Xiong, and H. Zhang, *ACS Nano* **7**, 10344–10353 (2013).
- (31) X. Zhang, W.P. Han, J.B. Wu, S. Milana, Y. Lu, Q.Q. Li, A.C. Ferrari, and P.H. Tan, *Phys. Rev. B* **87**, 115413 (2013).
- (32) B. Amorim, A. Cortijo, F. de Juan, A.G. Grushin, F. Guinea, A. Gutierrez-Rubio, H. Ochoa, V. Parente, R. Roldan, P. San-Jose, J. Schiefele, M. Sturla, and M.A.H. Vozmediano, *Phys. Reports* **617**, 1–54 (2016).
- (33) M. Yagmurcukardes, C. Bacaksiz, E. Unsal, B. Akbali, R.T. Senger, and H. Sahin, *Phys. Rev. B* **97**, 115427 (2018).



David Tuschel is a Raman applications manager at Horiba Scientific, in Edison, New Jersey, where he works with Fran Adar. David is sharing authorship of this column with Fran. He can be reached at: SpectroscopyEdit@UBM.com

For more information on this topic, please visit:
www.spectroscopyonline.com/adar

Certified Reference Materials
 UV/VIS/NIR/MidIR from a
World Leader

Deep UV to Infra-red
 Fluorescence
 Microvolume & microplate
 ISO 17034:2016 &
 ISO/IEC 17025:2017 accredited
 Lifetime Guarantee
 Fast re-calibration service
 Custom & OEM

Starna
 Starna Scientific Ltd

Starna Cells Inc.
 (800) 228-4482
 sales@starnacells.com
 www.starna.com

Focus on Quality

Analysis of FDA Infrared 483 Citations: Have You a Data Integrity Problem?

Analysis of 47 FDA Form 483 observations and warning letters for infrared spectrometers reveals a spectrum of data integrity problems and a lack of laboratory procedures for the technique. Is this your laboratory?

P.A. Smith and R.D. McDowall

Since the Able Laboratories data falsification case in 2005 (1), there has been a regulatory focus on the lack of data integrity with chromatography data systems. This scrutiny has focused on inappropriate access privileges with conflicts of interest, deletion of data files, failure to configure the application, testing into compliance, and failure to review audit trail entries (2). More recently, inspection focus has moved to the use of peak integration to integrate into compliance and masking potential impurities (3). There have been many warning letters as a result of these noncompliances and poor data management practices; this is due to chromatography being a major technique that can comprise between 40–70% of a laboratory's workload. You may ask, "Why the focus on chromatography in a publication on spectroscopy?" Just think of chromatography as sample preparation for spectroscopy!

In contrast, there are relatively few FDA warning letters involving spectroscopic techniques. An analysis of FDA warning letters citing infrared spectrometers was published in 2014 (4).

Originally, we were going to write a column looking at some of the data integrity issues that could occur with Fourier transform infrared spectroscopy (FT-IR) analysis, with a few regulatory citations to illustrate each point. However, given the bonanza of Form 483 observations and warning letters that have been issued by the FDA, we realized that an analysis of these would provide a great overview of the current regulatory problems facing the technique, before discussing specific topics in the future.

Understanding Our Approach

In this column, we present an analysis of 47 Form 483 observations and warning letters issued between 2012 and 2018 (5–51). It should be noted that many of these Form 483 observations are not generally available publicly. Therefore, these observations, the regulatory focus on infrared, and the conclusions we have drawn may be new to laboratories that only review FDA warning letters. We have taken each citation or observation and broken it down into one or more data integrity areas; therefore, a single observation can have one or more data integrity noncompliances. For example:

- The application does not have an audit trail. This is a single 483 observation and a single data integrity issue.
- In contrast, here is a more complex citation: System audit trails are not available on the two FT-IR instruments, and quality control (QC) operators have the option of not saving the IR data. This citation will be classified into two entries; one of no audit trail, and another of application software design because data are not automatically saved. This is a simple example of compound data integrity problems, but some citations can be far more detailed and complex.

Therefore, there is not a one-to-one correlation between all noncompliances analyzed and the data classification presented here.

The noncompliances have resulted in a total of 104 separate citations for IR analysis that have been classified and discussed below. Some of these are self-explanatory, and will not be discussed in part due to space considerations and because the solution is obvious (such as no software validation, for example). In the references, we

have included the FDA Facility Establishment Identifier (FEI), which is the way the FDA identifies a specific site in a company. Where there are different FEI numbers for the same organization, this means that two sites or facilities were inspected.

Our main challenge in this analysis is to interpret a regulatory citation, because we don't know all the circumstances at the time of the observation by an inspector. For example, we don't know the functionality of the application software, so the observation of no system audit trails available as shown above could be a true software design limitation, or, more likely, it could be that the users did not enable this function. We have used our experience and best judgement in classifying each citation in this analysis.

We do not claim that this noncompliance review reflects the total number of 483 observations issued, but, based on the significant number, it is reasonably comprehensive to draw firm conclusions on regulatory gaps involving IR analysis. Enjoy reading about the calamities of others. If any noncompliance mentioned here applies to your laboratory, what are you going to do? We suggest that you remediate the problem before you are included in a future update of this article!

Citations Before the Operational Use of the Instrument

One of the surprises of our analysis is that 42% of the 483 citations occur before the instrument and the associated software application are supposed to become operational. You may doubt this statement, but look at both Table I and Figure 1 and you will see two main areas: inadequate software architecture, and design and failure to qualify, calibrate, or validate the system. The interpretation of these nonconformance data is based on the wording of the 483 observations.

The biggest area, at 37% of the total noncompliances, appears to be due to inadequate architecture and design of the application software that has been purchased by the regulated laboratories. The main problems with the application software are that, as implemented, there are inadequate controls for ensuring data integrity, no audit trail, and the architecture where data files are stored in directories within the operating system and users can delete data without any record in the data system. Again, this is based on the wording inspectors

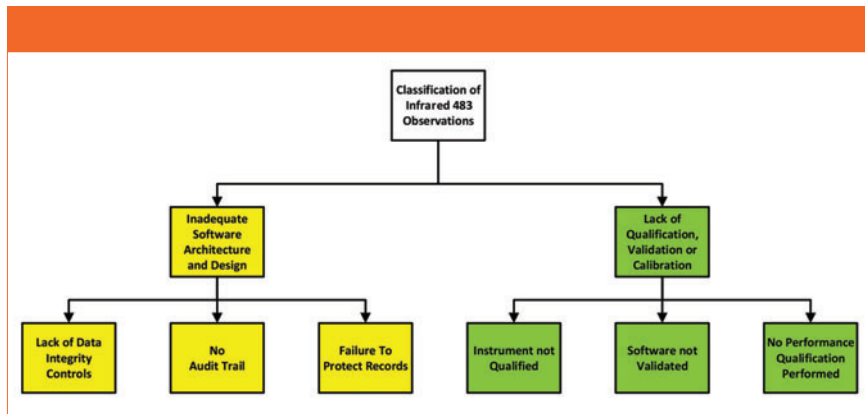


Figure 1: Infrared spectroscopy Form 483 citations occurring before operational use of the instrument and software.

included in each Form 483 report, which represents a high level conclusive summary of the inspection findings, and not a detailed analysis of the root cause associated with each observation. In particular, this represents the inspector's interpretation of what was found about how software was implemented, and not the full compliance capabilities of each software package. In line with FDA warning letters, in many instances, the

manufacturer and name of the software was included in many of the examples we reviewed, but we have redacted these in this column.

Some of the citations for poor software design are:

- The UV and FT-IR analytical instruments are both equipped with commercial software that does not prevent accidental or intentional deletion of files containing data.



Hexagonal Grid with Underlying Supports X-ray Mapping

EDAX Data - Accurate representation. No distortion, no broadening.

Oblique Geometry Data - Broadening of wire grids and supports shows X-ray counts originating where they should not.

Geometry designed for accurate elemental analysis when results matter.

- Orbis micro-XRF Analyzer: Non-destructive X-ray elemental analysis from Na to Bk
- Excitation geometry perpendicular to sample for accurate sample targeting
- High intensity analysis for micro to millimeter areas
- Increased sensitivity with filters as standard
- Fastest analytical speed with state of the art detectors

Power your next insight with EDAX.
edax.com/Products/Micro-XRF/Orbis/index.aspx

AMETEK
MATERIALS ANALYSIS DIVISION

Micro-XRF Applications Include:

- Micro size parts, defects and small inclusions
- Forensics
- Industrial QC/FA
- Compliance Testing
- Coating Thickness / Composition
- and much more ...

EDAX

Smart Insight

Table I: Infrared spectroscopy Form 493 citations Part 1: citations occurring before operational use of the instrument

Noncompliance	Citation	Number
No qualification, validation, or calibration (6%)	No validation	1
	No instrument qualification	3
	No performance qualification	2
Inadequate software architecture and design (37%)	Lack of data integrity controls	5
	No audit trail	16
	Failure to protect records	17
Total citations before operational use of instrument (42% of total citations)		44

Table II: Infrared spectroscopy Form 483 non compliances Part 2: operational use of the instrument

Noncompliance	Citations	Number
Poor security and access control (11%)	Shared identities, conflicts of interest, all users are administrators	11
Data falsification or testing into compliance (8%)	Data deletion, repeat testing	8
No audit trail review (7%)	When there is an audit trail, the entries are not reviewed	7
Failure to backup data (7%)	Backup not performed, or backup is inconsistent	7
Work not scientifically sound (6%)	Unscientific use of the instrument	6
Inadequate instrument log book entries (5%)	Instrument log book entries, not performed, inadequate, not done, or entries not reviewed	5
Lack of procedures (4%)	Procedures are not written, or do not document current working practices	4
Failure to maintain complete data (3%)	Data lost, or no data for a test found	3
Raw data defined as paper (3%)	Focus on paper printouts, and not electronic records as the GMP records	3
Inadequate OOS investigations (3%)	No scientific basis for the conclusion of the investigation	3
Miscellaneous (3%)	Lack of a data integrity review program	1
	No data assessment after calibration failure	1
	No verification of a compendial test	1
Total citations during operational use of instrument (58% of total citations)		60

- QC operators have the option of not saving the IR spectra.
- With the FT-IR instrument (QC/FT-IR/201), it was noted that the redacted software had an option to enable or disable automatic saving of measurement available to the chemist.
- FT-IR spectrophotometers used in identity testing were observed to have a “delete” option available to the user.
- The lack of an audit trail was one of the largest number of citations; there was no audit trail in 16 out of 104, or 15%, of all citations.

The use of directories in the operating system for data storage where a user can delete spectral files without any record in the application software (assuming there is a function capable of this) gave rise to 17 citations out of 104, or 16%.

- There were no controls to prevent deletion of data and deleted FT-IR data was observed in the computer recycle bin.
- Data can be deleted off the FT-IR used in the testing of active pharmaceutical ingredient (API). The data can be deleted off the computer systems hard drive, outside of the system software, and therefore not captured by the systems audit trail.
- Laboratory personnel can change and save changes to the date and time setting in the Windows operating system.

The first problem is that regulated laboratories are purchasing IR application software that appears not to have any or inadequate data integrity controls. For example, all data should be saved, and there must be an audit trail built into the system which, once implemented, cannot be turned off. However, suppliers are market driven, and if users don't ask for these features, or help into how to implement them, then they won't be delivered. The responsibility of the supplier to help customers implement a compliant solution is becoming increasingly important. There is also the overall market that a supplier is developing its software for both regulated and unregulated industry sectors. What should occur is that suppliers should be selling configurable software, and also providing assistance in the form of white papers informing users how to configure the software or providing professional services to help implement compliant solutions. The second issue is the overall architecture of the system: Almost all IR software is designed for standalone operation, or can be implemented as a standalone system. Many standalone systems involve files storage in directories in an operating system, and not a database. If the software is designed to support networked implementation, using database storage on a secure network server, this should be implemented. This would remove many of the limitations of standalone systems, such as backup, as this would be performed by the IT department.

Part of the problem is that many software applications require a range of expertise to implement compliant solutions,

so that an expert in the analytical technique, someone with a detailed understanding of the software capabilities and strong IT and Part 11 knowledge, is required. From the number of Form 483 observations, it is clear that this multidisciplinary collaboration has not occurred.

What are Performance Qualification Tests for IR Instruments?

The second area for noncompliance before operational use of the instrument (6%) is due to failure to qualify or calibrate the instrument or validate the software. This is a fairly straightforward area, and we were not going to discuss this, with the exception of two citations about the performance qualification of an IR instrument, one of which is:

No Performance Qualification (PQ) is required before use to ensure the performance of the <redacted> FT-IR; only the . . . operation qualification is performed. In addition, the SOP # <redacted> does not require such a test.

United States Pharmacopoeia (USP) general chapter <1058> on Analytical Instrument Qualification (AIQ) was recently updated (52), and contains new requirements compared with the 2008 version. The key issues are that:

- Users must write a user requirements specification (URS) that contains the operating parameters for the IR spectrometer and the instrument software.
- These parameters are verified in the Operational Qualification (OQ).
- Performance Qualification (PQ) needs tests that either directly or indirectly confirm that the instrument continues to operate in compliance with the operating parameters in the URS (52).

The difference between an instrument OQ and PQ is typically the area of greatest discussion when considering analytical instrument qualification. It is important to first understand that, because an OQ and PQ test different attributes of instrument performance, both are required.

Uniquely for FT-IR, the subject of calibration also needs to be considered because of confusion that can arise around interpretation of this word. First, in simple terms, the instrument performance attributes that are associated with an OQ and PQ are:

- OQ: Documents how the instrument satisfies user requirements before operational release and at regular intervals, typically after an annual preventative maintenance service.
- PQ: Demonstrates the instrument continues to work under actual conditions of use as documented in the user requirements specification.

The reader must consider what these terms mean for an FT-IR instrument, and be able to defend this interpretation during regulatory inspections.

For an FT-IR instrument, apart from replacing the internal desiccant that removes water vapor from sealed instrument enclosure, there are typically no user serviceable components. Therefore, it would be more appropriate to label regular testing of instrument as performance verification checks for wavelength accuracy, resolution, and signal-to-noise, rather than calibration. However, for an FDA inspector, calibration is most likely to be the name used for in-

strument performance checks, because this is specified in the Good Manufacturing Practice regulations in 21 *CFR* 211.160(b)(4) (53).

Tests performed on analytical instruments during qualification typically fall under the following categories:

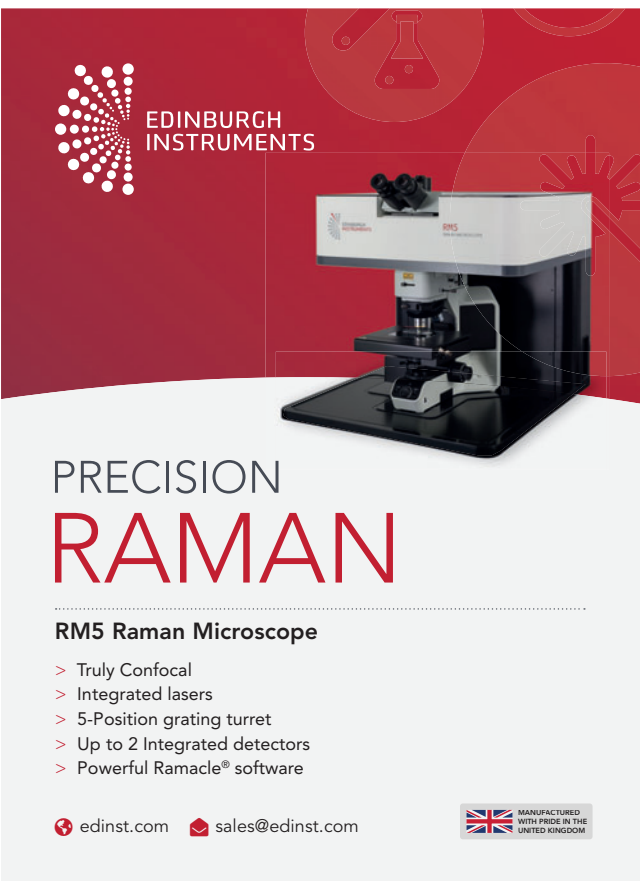
- metrology-based tests (not needed for an FT-IR instrument, unless temperature controlled)
- reference material-based tests
- detector noise-based tests
- usage-based tests (recording spectra).

We will return to this topic in a later “Focus on Quality” column, where we will address OQ and PQ requirements for FT-IR in more detail.

Citations During the Operational Phase

The main citations for IR systems found by FDA inspectors during the operational phase are listed in Table II, and shown diagrammatically in Figure 2. In general, these citations mirror those found with chromatography data systems (CDS) such as:

- Poor Security and Access Control: This is the biggest problem with issues identified such as no security, all users have the same identity, and password thus making attribution of action impossible and conflicts of interest where all laboratory users have administrator rights. Some people will never learn! This is especially true when these citations against CDS have been made for the past 10–15 years. What is interesting in this case is that some laboratories have been cited because management had administrator access, confirming a requirement for applica-



EDINBURGH INSTRUMENTS

PRECISION
RAMAN

RM5 Raman Microscope

- > Truly Confocal
- > Integrated lasers
- > 5-Position grating turret
- > Up to 2 Integrated detectors
- > Powerful Ramacle® software

edinst.com sales@edinst.com

MANUFACTURED WITH PRIDE IN THE UNITED KINGDOM

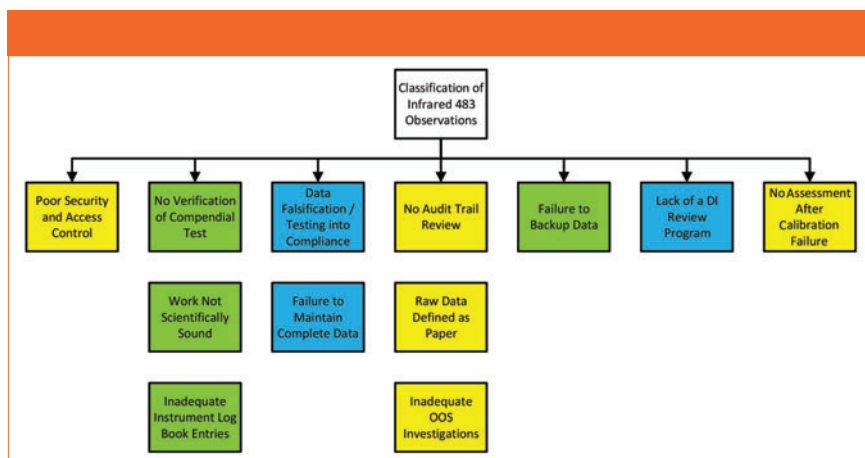


Figure 2: Infrared spectroscopy Form 483 observations as found by FDA inspectors during operational work.

- Pharmacopeia requirements are not harmonized for FT-IR.

Historically, the IT departments in many companies had a policy that made it harder for laboratories to attach instrument control computers to the corporate network. In principle, this was to protect the network, but the outcome can be proliferation of standalone systems, irrespective of the system capability. A busy laboratory can follow the path of least resistance, and implement standalone systems with the consequential impact of poor data backup and access control, for example. Some of the principal reasons for originally writing this article was the data integrity risks of identification by FT-IR spectroscopy; in particular, because there is a skill associated with the manual task of sample preparation, it will always be a higher risk from a data integrity perspective. How are decisions made about the quality of the sample preparation recorded and differentiated from identification failure?

Analysts in busy laboratories have tended to move away from specialist skills (in IR spectroscopy, for example), toward being more generalists. This trend contributes to some of the citations in this article, such as inappropriate and unscientific use of the technique. The difference between an IR spectroscopist and a part-time user was well documented over 20 years ago (57).

Another contributory factor, which is compounded by the deskilling of analysts, is the lack of harmonization of the pharmacopeia general chapters on identification by IR spectroscopy.

tion administration to be independent of the laboratory.

- Data Falsification/Testing into Compliance: This is another classic area for citations that is not limited to CDS, and are also found with IR systems. Citations here include data deletion, and retesting until a passing result is obtained. Some people never learn.
- No Audit Trail Review: Even when you have an audit trail in the application, it is either turned off or if it is turned on the entries are not reviewed. There is even one citation where the audit trail is stored on a secure network, but the laboratory and QA staff cannot access it!
- Failure to Backup Data: This is a major problem when a laboratory is left to backup its own GMP records, and fails to do so. It is always better to get the IT department to back the data up on secure network drives.

In addition, there are the following gems of noncompliance:

- Work Not Scientifically Sound: A variety of novel and unscientific approaches to charm FDA inspectors, such as use of IR analysis for cleaning validation where lack of sensitivity to detect an analyte was the issue (for example, using an identification algorithm to compare spectra of cleaning wash samples with pure solvents). On the bright side, every cleaning validation passes.
- Inadequate Instrument Log Book Entries: The instrument log book was featured in an earlier "Focus on Quality" column (54); here there were five citations for inadequate log book entries, including the

failure of a second person to review them.

- Lack of Procedures: Another evergreen classic of noncompliance. No procedure or work instruction available, and naturally no training records, either—two citations for one noncompliance! Come on, how easy do you want to make it for an auditor or inspector?
- Failure to Maintain Complete Data: Although closely associated with data falsification, the writing of the citations indicate that this is due to a laboratory error, such as losing rather than deleting electronic records. Also, there are signed paper printouts, but no accompanying electronic records—oops!
- Raw Data Defined as Paper: One of the main data integrity messages is that paper cannot be raw data when a computerized system is involved (55); unsurprisingly, this message has not got through to some laboratories, who then receive a 483 observation.
- Inadequate OOS Investigations: Invalidated OOS results are a key quality metric that the FDA have selected for GMP laboratories as part of their quality metrics program (56), and it is the lack of root cause analysis or finding a scientifically sound assignable cause for invalidating an OOS result that gains an inspector's attention.

Contributory Factors

Some of the factors that contributed to the observations reported in this article are:

- Historical IT perspective: Protection of the corporate network
- Deskilling of the analyst workforce: The move from specialist to generalist

- How large should a difference between two infrared spectra be, before action needs to be taken?
- Where differences occur, some drug monographs require the sample and the reference material to be recrystallized to confirm the identification; how many laboratories do this?
- Even the process used to perform the identification can be different; some pharmacopeias include reference spectra that can be used, while others require that a reference material spectrum is recorded concordantly.

Where there is a lack of harmonization, the simplest route can be to ignore specific pharmacopeia requirements.

The fundamental challenge for identification by infrared (either IR or FT-IR spectroscopy) is the decision about how the

comparison should be made. If spectra are compared by algorithms, the library and the limits used need to be validated. Ironically, if the decision is based on manual comparison of sample and reference spectra, this can be best accomplished using large printed spectra, with the investment focus on analyst training compared to library and algorithm validation. Although there are some other citations, as seen in Table II, we have chosen not to discuss them as they are single observations and may not be indicative of a trend.

Summary

In this column, we have taken 104 regulatory noncompliances for infrared analysis issued by the FDA and analyzed them for trends. Interestingly, 42% of noncompliances can occur before an instrument is operational, due to the purchase of poor software functions, or failure to validate, qualify, or calibrate the system. Noncompliances when an instrument is operational vary widely, but mirror those found with CDS, such as inadequate access control, data falsification, lack of complete data, inadequate backup, and no audit trail review.

Based on this review and the non-conformance findings in the Form 483 observations, it is apparent that identification by FT-IR spectroscopy is an area of focus during laboratory audits, and that it is a high-risk area with poor implementation of compliant solutions. As an example of this regulatory focus, Yunnan Hande received an FDA warning letter in 2015. The Form 483 observations include a range of data integrity observations, but the warning letter only focuses on identification by infrared (58).

References

- (1) *Able Laboratories Form 483 Observations. 2005* (2016); Available from: <http://www.fda.gov/downloads/aboutfda/centersoffices/officeofglobalregulatoryoperationsandpolicy/ora/oraelectronicreadingroom/ucm061818.pdf>.
- (2) R.D. McDowall, *Validation of Chromatography Data Systems: Ensuring Data Integrity, Meeting Business and Regulatory Requirements* (Royal Society of Chemistry, Cambridge, United Kingdom, 2nd ed., 2017).
- (3) H. Longdon and R.D. McDowall, *LCGC Europe* **32**, (In press) (2019).
- (4) P. Smith, *Pharm. Technol.* **26**(5), 48–51 (2014).
- (5) *FDA 483 Observations Cispharma, USA*, April 23, 2012, FEI 3008276856 (Food and Drug Administration, Silver Spring, Maryland, 2012).
- (6) *FDA Warning Letter Cadila Pharmaceuticals Ltd, India*, March 28, 2014, FEI 3002806711 (Food and Drug Administration, Silver Spring, Maryland, 2014).
- (7) *FDA Warning Letter Unimark Remedies, India*, March 21, 2014, FEI 3005202703 (Food and Drug Administration, Silver Spring, Maryland, 2014).
- (8) *FDA 483 Observations Lynwood, USA*, April 3, 2014, FEI 1000160562 (Food and Drug Administration, Silver Spring, Maryland, 2014).
- (9) *FDA 483 Observations Ohm Laboratories, USA*, March 18, 2014, FEI 1000222352 (Food and Drug Administration, Silver Spring, Maryland, 2014).
- (10) *FDA 483 Observations Cosma S.p.A, Italy*, January 15, 2015, FEI 3002806754 (Food and Drug Administration, Silver Spring, Maryland, 2015).

- (11) *FDA 483 Observations Yunnan Hand, China*, February 26, 2016, FEI 3002808537 (Food and Drug Administration, Silver Spring, Maryland, 2016).
- (12) *FDA Warning Letter Wockhardt, India*, December 15, 2016, FEI 3002808500 (Food and Drug Administration, Silver Spring, Maryland, 2016).
- (13) *FDA 483 Observations Tianjin, China*, September 2, 2016, FEI 3008256667 (Food and Drug Administration, Silver Spring, Maryland, 2016).
- (14) *FDA 483 Observations Tianjin, China*, September 1, 2016, FEI 3007751421 (Food and Drug Administration, Silver Spring, Maryland, 2016).
- (15) *FDA 483 Observations Teva, Hungary*, January 29, 2016, FEI 3002875215 (Food and Drug Administration, Silver Spring, Maryland, 2016).
- (16) *FDA 483 Observations Synbiotics, India*, March 31, 2016, FEI 3008494993 (Food and Drug Administration, Silver Spring, Maryland, 2016).
- (17) *FDA 483 Observations Sun Pharma, India*, July 29, 2016, FEI 3012032037 (Food and Drug Administration, Silver Spring, Maryland, 2016).
- (18) *FDA 483 Observations Spectrum Laboratories, USA*, March 14, 2016, FEI 2246824 (Food and Drug Administration, Silver Spring, Maryland, 2016).
- (19) *FDA 483 Observations Sekisui Medical Co, Japan*, June 17, 2016, FEI 3002806840 (Food and Drug Administration: Silver Spring, Maryland, 2016).
- (20) *FDA 483 Observations Olon S.p.A, Italy*, February 5, 2016, FEI



Quality Cells for Quality results



Starna

Starna Scientific Ltd

Fully fused construction

Transmission from 190 nm to 3800 nm

Path lengths from 0.008 to 500 mm

Volumes from 0.5µl to 170ml

Wide range of standard cells

Custom designs

Starna Cells Inc.

(800) 228-4482

sales@starnacells.com

www.starna.com

- 3002806373 (Food and Drug Administration, Silver Spring, Maryland, 2016).
- (21) *FDA 483 Observations Natco Pharma, India*, March 7, 2016, FEI 3004540906 (Food and Drug Administration, Silver Spring, Maryland, 2016).
- (22) *FDA 483 Observations Jinan Jinda, China*, June 1, 2016, FEI 3004002973 (Food and Drug Administration, Silver Spring, Maryland, 2016).
- (23) *FDA 483 Observations Huntington, USA*, June 24, 2017, FEI 1810414. (Food and Drug Administration, Silver Spring, Maryland, 2016).
- (24) *FDA 483 Observations Coral Drug Private Ltd, India*, March 11, 2016, FEI 3003496619 (Food and Drug Administration, Silver Spring, Maryland, 2016).
- (25) *FDA 483 Observations Cheng Pong Chemical, China*, April 22, 2016, FEI 1000174711 (Food and Drug Administration, Silver Spring, Maryland, 2016).
- (26) *FDA 483 Observations Belcher Pharmaceuticals, USA*, May 13, 2016, FEI 1000526113. (Food and Drug Administration, Silver Spring, Maryland, 2016).
- (27) *FDA 483 Observations Bayer, Finland*, May 15, 2016, FEI 1000350927 (Food and Drug Administration, Silver Spring, Maryland, 2016).
- (28) *FDA 483 Observations Apotex, India*, June 3, 2016, FEI 3005466325 (Food and Drug Administration, Silver Spring, Maryland, 2016).
- (29) *FDA 483 Observations Anjan Drug Private, India*, January 18, 2016, FEI 3005782924 (Food and Drug Administration, Silver Spring, Maryland, 2016).
- (30) *FDA 483 Observations 3M Health Care, UK*, August 12, 2016, FEI 3002807506 (Food and Drug Administration, Silver Spring, Maryland, 2016).
- (31) *FDA 483 Observations Troy, USA*, January 17, 2017, FEI 3001451565 (Food and Drug Administration, Silver Spring, Maryland, 2017).
- (32) *FDA 483 Observations Mitsubishi Tanabe, Japan*, September 22, 2017, FEI 3002808316 (Food and Drug Administration, Silver Spring, Maryland, 2017).
- (33) *FDA 483 Observations Lymol Medical Corp, USA*, June 24, 2017, FEI 1221129 (Food and Drug Administration, Silver Spring, Maryland, 2017).
- (34) *FDA 483 Observations Kymos, Spain*, July 18, 2018, FEI 3008661256 (Food and Drug Administration, Silver Spring, Maryland, 2017).
- (35) *FDA 483 Observations IDT Australia Ltd., Australia*, December 8, 2017, FEI 3000219354 (Food and Drug Administration, Silver Spring, Maryland, 2017).
- (36) *FDA 483 Observations Genus Life Sciences Inc., USA*, September 29, 2017, FEI 3003851100 (Food and Drug Administration, Silver Spring, Maryland, 2017).
- (37) *FDA Warning Letter Fresenius Kabi, India*, May 24, 2017, FEI 3003519498 (Food and Drug Administration, Silver Spring, Maryland, 2017).
- (38) *FDA 483 Observations Daito Pharmaceuticals, USA*, November 10, 2017, FEI 3002806779 (Food and Drug Administration, Silver Spring, Maryland, 2017).
- (39) *FDA 483 Observations Cambrex Profarmico, Italy*, May 19, 2017, FEI 3003723076 (Food and Drug Administration, Silver Spring, Maryland, 2017).
- (40) *FDA 483 Observations ABS Corporation, USA*, November 16, 2017, FEI 1950042 (Food and Drug Administration, Silver Spring, Maryland, 2017).
- (41) *FDA 483 Observations Vetter Pharma, Germany*, January 17, 2017, FEI 3002270322 (Food and Drug Administration, Silver Spring, Maryland, 2017).
- (42) *FDA 483 Observations Laclede, Inc., USA*, November 7, 2018, FEI 2022474 (Food and Drug Administration, Silver Spring, Maryland, 2018).
- (43) *FDA 483 Observations Kaken Pharmaceutical Co., Ltd., Japan*, June 22, 2018, FEI 3002807376 (Food and Drug Administration, Silver Spring, Maryland, 2018).
- (44) *FDA 483 Observations Covinia, USA*, May 15, 2018, FEI 2013342 (Food and Drug Administration, Silver Spring, Maryland, 2018).
- (45) *FDA 483 Observations, Carson, USA*, November 19, 2018, FEI 2012546 (Food and Drug Administration, Silver Spring, Maryland, 2018).
- (46) *FDA 483 Observations CMIC, Korea*, June 16, 2018, FEI 3013212450 (Food and Drug Administration, Silver Spring, Maryland, 2018).
- (47) *FDA 483 Observations Cambridge Major Laboratories, Netherlands*, November 9, 2018, FEI 3004153149 (Food and Drug Administration, Silver Spring, Maryland, 2018).
- (48) *FDA 483 Observations Apotek Production Laboratories, India*, June 1, 2018, FEI 3004967053 (Food and Drug Administration, Silver Spring, Maryland, 2018).
- (49) *FDA 483 Observations Acorn Inc, USA*, August 30, 2018, FEI 2246848 (Food and Drug Administration, Silver Spring, Maryland, 2018).
- (50) *FDA 483 Observations G&W Labs, USA*, February 15, 2018, FEI 2210277 (Food and Drug Administration, Silver Spring, Maryland, 2018).
- (51) *FDA 483 Observations Lupin, India*, October 18, 2018, FEI 3009107538. (Food and Drug Administration, Silver Spring, Maryland, 2018).
- (52) *USP 41 General Chapter <1058> Analytical Instrument Qualification* (United States Pharmacopoeia Convention Rockville, Maryland, 2018).
- (53) *21 CFR 211 Current Good Manufacturing Practice for Finished Pharmaceutical Products* (Food and Drug Administration, Silver Spring, Maryland, 2008).
- (54) R.D. McDowall, *Spectroscopy* **32**(12), 8–12 (2017).
- (55) *FDA Guidance for Industry Data Integrity and Compliance With Drug CGMP Questions and Answers*, (Food and Drug Administration, Silver Spring, Maryland, 2018).
- (56) *FDA Guidance for Industry Submission of Quality Metrics Data, Revision 1* (Food and Drug Administration: Rockville, Maryland, 2016).
- (57) G.Dent, *Spectrochim. Acta, Part A* **51**, 2209 (1995).
- (58) *FDA Warning Letter, Yunnan Hande Biotech Co. Ltd.*, April 6, 2015 (Food and Drug Administration, Silver Spring, Maryland, 2015).

About the Guest Co-Author



Paul Smith is a Global Strategic Compliance Specialist at Agilent Technologies.

About the Columnist



R.D. McDowall is the director of R.D. McDowall Limited and the editor of the "Questions of Quality" column for *LCGC Europe*, *Spectroscopy's* sister magazine. Direct correspondence to: SpectroscopyEdit@UBM.com

For more information on this topic, please visit our homepage at: www.spectroscopyonline.com



Bringing Raman to Life

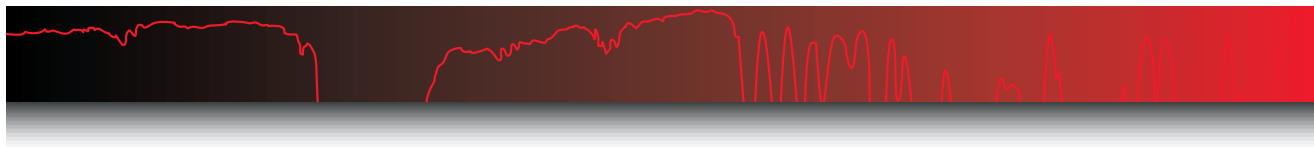
Raman spectroscopy holds great potential to provide answers about the world around us. As you unlock these connections, we're creating the products to bring them to life, from off-the-shelf modular systems for research to compact, integrated solutions for OEMs. Contact us to learn how we're pushing the limits of compact Raman – in speed, sensitivity, and limit of detection.

RAMAN | UV-VIS | FLUORESCENCE | NIR
 +1 919-544-7785 • info@wasatchphotonics.com • wasatchphotonics.com

Wasatch) **Photonics**

SCIX 2019

You spoke, and we listened. See for yourself with our newest products: flexible, integrated Raman systems, adaptive sampling accessories, and built-in library matching software! **COME SEE US AT BOOTH 713**



IR Spectral Interpretation Workshop

Organic Nitrogen Compounds V: Amine Salts

The nitrogen of amines is basic, and can react with strong acids to form what are called *amine salts*. These compounds are very important in the pharmaceutical industry, as many active pharmaceutical ingredients are amine salts. The amine salt functional group contains ionic bonding, and is extremely polar, giving rise to a number of intense and uniquely placed peaks that makes them easy to identify. In this article, the amine salts of primary, secondary, and tertiary amines will be discussed.

Brian C. Smith

This is the fifth installment in our examination of the infrared (IR) spectra of organic nitrogen-containing functional groups. In previous columns, I introduced the topic, and we studied the spectra of primary amines, secondary amines, tertiary amines, and nitriles (1–4). The nitrogen of amines possesses a lone pair of electrons. This lone pair is somewhat basic, and can react with strong acids to form what are called *amine salts* (5). Primary amines, secondary amines, and tertiary amines can react with strong acids to form what are called *primary amine salts*, *secondary amine salts*, and *tertiary amine salts*. The reactions of these three amines with hydrochloric acid to form amine salts is illustrated in Figure 1.

Note the unusual structure of amine salts seen in Figure 1. The lone pair of electrons on the amine reacts with the proton from the acid, forming a new N-H bond. Thus, the primary amine NH_2 group is protonated to give a NH_3^+ unit, a secondary amine N-H is protonated to give a NH_2^+ functional group, and a tertiary amine is protonated to give a NH^+ unit. As a result, the amine salt functional group is highly polar, with a positive charge on the nitrogen that is balanced by the negative charge from the anion of the acid. In the case of hydrochloric acid, this is the chloride ion, Cl^- .

Recall that, in a classical acid-base reaction, one of the products is called a salt (5). For example, the reaction of HCl and NaOH literally gives salt (NaCl) and water. The reactions in Figure 1 are acid-base reactions, hence the designation of one of the products as an amine salt. Although many strong acids can be used

to form amine salts, in my observation, hydrochloric acid is most frequently used. In this case, the amine salt is a hydrochloride salt, and the name *hydrochloride* is added to the name of the compound. For example, the reaction of methylamine with hydrochloric acid forms methylamine hydrochloride.

Because we have full positive and negative charges in the amine salt functional group, we have ionic bonding instead of the covalent bonding found in amines. Ultimately, we have two large charges separated by a distance, which means that amine salts have large dipole moments. Recall that one of the things that determines IR peak intensity is $d\mu/dx$, the change in dipole moment with respect to distance during a vibration (6). Given that amine salts have large dipole moments, their vibrations have large values of $d\mu/dx$, and so their spectra have intense peaks, as we will see below.

Amine salts are very important in medicinal chemistry, and any number of legal (and illegal) drugs contain the amine salt functional group. The reason for this is water solubility; a water soluble molecule is more easily taken in by the human body, and is more bioavailable than a water insoluble molecule. Many drug substances are large organic molecules, which tend to be nonpolar and water insoluble. Additionally, many drug substances contain amine groups. By simply reacting the drug molecule's amine functional group with a strong acid like HCl, the amine salt is formed, and the compound is rendered water soluble, and thus more bioavailable.

Being able to distinguish amines from amine salts even has legal implications. Cocaine is found in two forms, the hydrochloro-



How did *you* Learn Raman?



Learn more at:
LearnRaman.com
(516) 939-0888
reva@hellma.com
 @LearnRaman



← *Scan Me!*

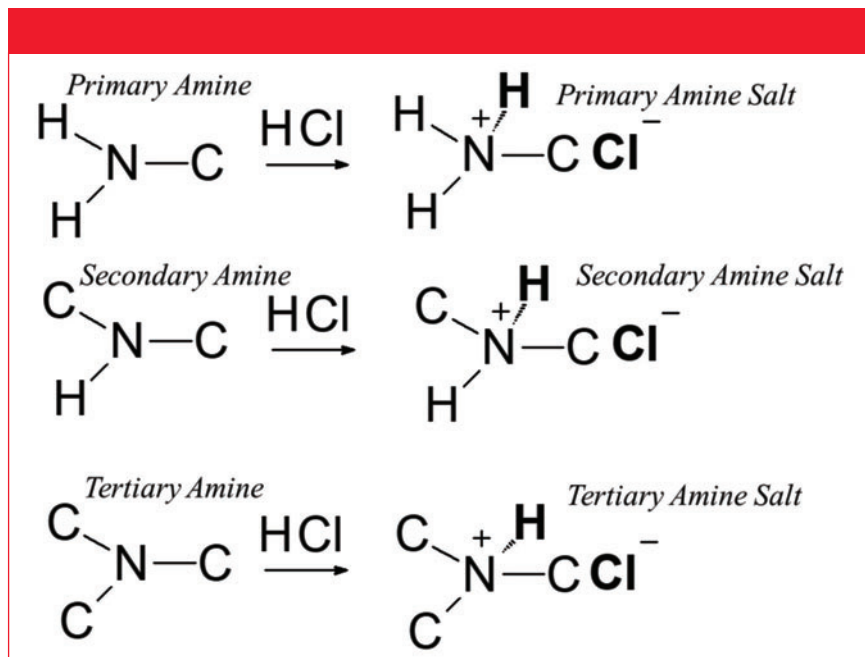


Figure 1: The reaction of a primary amine, secondary amine, and a tertiary amine with hydrochloric acid to form a primary amine salt, secondary amine salt, and a tertiary amine salt.

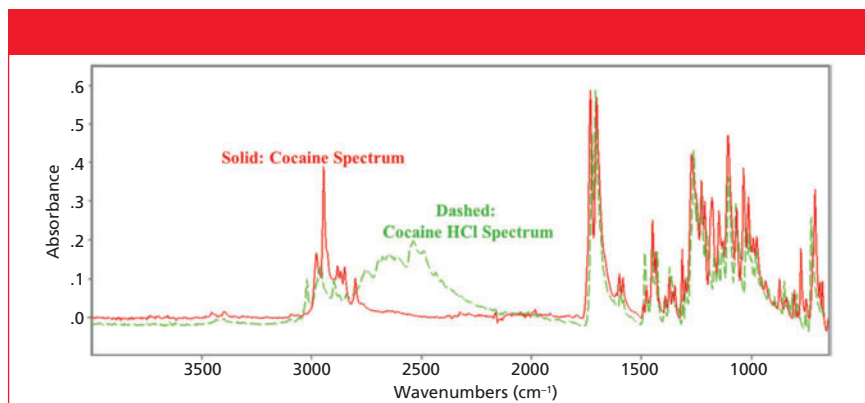


Figure 2: An overlay of the infrared absorbance spectra of cocaine and cocaine HCl.

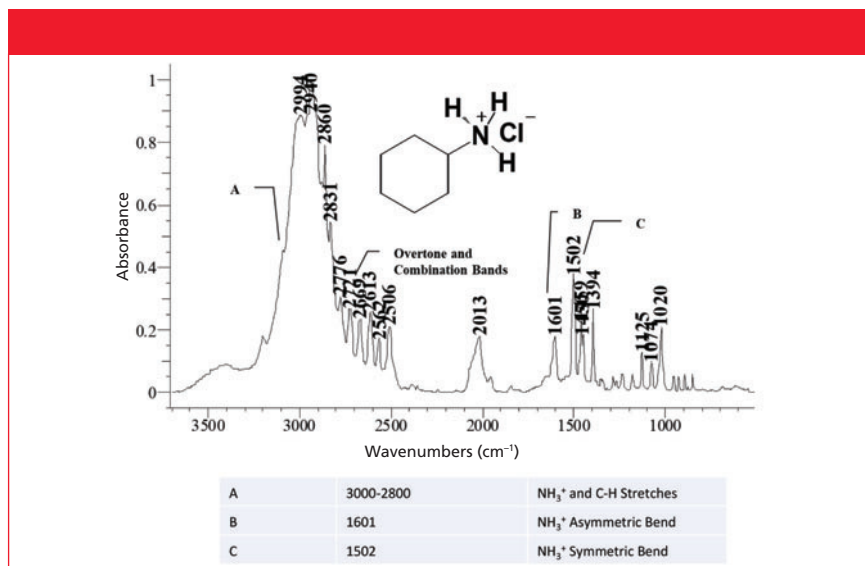


Figure 3: The infrared absorbance spectrum of cyclohexylamine hydrochloride.

ride amine salt and the amine or “free base” with the street name *crack cocaine* (7). In the United States, possession of these two illicit substances carries different penalties, as the crack version is considered more dangerous. One of the major uses of Fourier transform infrared spectroscopy (FT-IR) in forensic labs is distinguishing cocaine hydrochloride from cocaine. Fortunately, this is easy as can be seen in Figure 2, which shows an overlay of the IR spectra of cocaine base and cocaine HCl.

The IR Spectra of Amine Salts

Overview

In addition to intense peaks, we would expect amine salts to have broad peaks as well. Recall that, in IR spectra, peak width is determined by the strength of intermolecular bonding (6). Nonpolar functional groups, like benzene rings, have narrow peaks, while molecules that have strong intermolecular bonds, such as water, which is hydrogen bonded, have broad peaks (6). Amine salts are highly polar; their molecules interact strongly producing very broad peaks. This is seen in the spectrum of cyclohexylamine hydrochloride in Figure 3.

The tall and broad feature labeled A centered near 3000 cm⁻¹ (going forward, assume all peak positions listed are in cm⁻¹ units, even if not specifically stated) is an envelope of absorbance due to the stretching vibrations of the NH₃⁺ group. All amine salt spectra exhibit a broad envelope, like the one seen in Figure 3, which we will generically call the “NH⁺ stretching envelope.” This feature is broad enough, intense enough, and appears at an unusual enough position that, by itself, can be indicative of the presence of an amine salt in a sample. The position of this envelope varies with the type of amine salt, as discussed below.

The right-hand side of this envelope has superimposed upon it a number of peaks that are due to overtone and combination bands. Recall that overtone and combination features are usually weak (8). However, in the case of amine salts, their high polarity means that the $d\mu/dx$ values for these overtone and combination vibrations are large enough for these peaks to appear easily in the spectra of amine salts.

A note on the spectra of anions in amine salts: For hydrochloride salts, where the anion is the chloride or Cl⁻ ion, due to

its mass, peaks from vibrations involving this ion generally fall below 400, where most FT-IR spectra cut off. However, amine salts made from acids with polyatomic anions, such as sulfuric acid, do exhibit anion peaks in the mid-IR region. This is illustrated by the spectrum of d-amphetamine sulfate, which is made by reacting amphetamine with sulfuric acid, and whose spectrum is seen in Figure 4.

The broad envelope centered around 1050 is due to the stretching of the bonds in the SO_4^{-2} unit. The even broader envelope that extends from 3500 to 2000 is the NH^+ stretching envelope.

Primary Amine Salt Spectra

A primary amine salt features the NH_3^+ unit, with the resultant broad intense NH^+ stretching envelope seen in Figure 3. For primary amine salts, generally this envelope falls from 3200 to 2800. We already know that alkane C-H stretches also fall in this region (9). As is common in IR spectroscopy (10), if a broad peak and a narrow peak fall in the same wavenumber range, the narrow peak may be seen on top of or as a shoulder

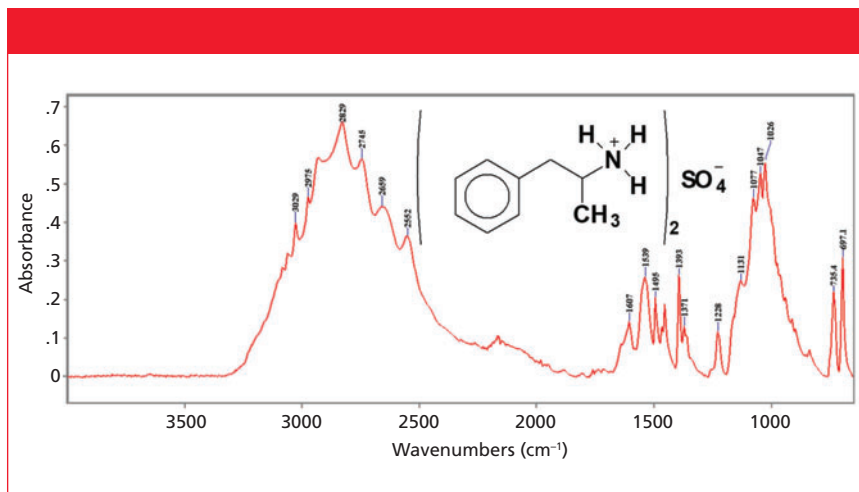


Figure 4: The infrared absorbance spectrum of d-amphetamine sulfate.

Table I: The Group Wavenumbers of Primary, Secondary, and Tertiary Amine Salts

Amine Salt	N-H Stretches	Overtone/Combi. Bands	N-H Bends
Primary NH_3^+	3200-2800	2800-2000	1625-1560 1550-1500
Secondary NH_2^+	3000-2700	2800-2000	1620-1560
Tertiary NH^+	2700-2300	2800-2000	—



Society for Applied Spectroscopy Training Courses

Are you doing infrared spectroscopy but feel that you are only scratching the surface? Does Raman spectroscopy confuse you and make you wonder where you can use it? Are you mystified when someone tells you that there is an enormous amount of information in infrared and Raman spectra but in school you learned to look and see when the carbonyl disappeared after reaction?

To address these needs and many others SAS is kicking off a training effort at SciX. We will be offering four courses geared to vibrational spectroscopy. They are:

- **Practical Vibrational Spectroscopy** (James A. de Haseth, University of Georgia)- Provides an introduction to Raman, mid-infrared and near-infrared concentrating on why an absorption occurs, where an absorption occurs and the benefits and limitations of the techniques.
- **Spectral Searching** (James A. de Haseth, University of Georgia) – Provides an introduction to spectral searching. Among other topics, this course will cover how to do an efficient search, why the first "hit" may not be the right answer and how to deal with a mixture or when the unknown is not in the database.
- **Problems with FT-IR Spectra and how to Avoid Them** (Ellen Mise, TeakOrigin, Jenni Brigg, Pike Technologies, Gloria Story, P&G) - Users of FT-IR spectrometers may have received little or no formal training in spectroscopy and therefore cannot distinguish between "good" and "bad" spectra. In this course, we will show many of the problems that are commonly encountered with FT-IR spectra measured by inexperienced (and often experienced!) users and show how to avoid them.
- **Introduction to Raman Spectroscopy and Imaging** (David Tuschel, HORIBA Scientific) - You will learn the basics of applied Raman spectroscopy and imaging and be taught the application of group theory to crystalline materials and how to apply those symmetry rules to perform "Raman Crystallography". The instructor will teach Raman spectroscopy and imaging at a practical level and cover topics to allow the student to immediately apply the material in the workplace.

Please see the SciX program for longer descriptions of these course and when they will be offered.

Answers to Previous Infrared Spectral Interpretation Challenge

The spectrum from the last interpretation challenge is seen in Figure ii.

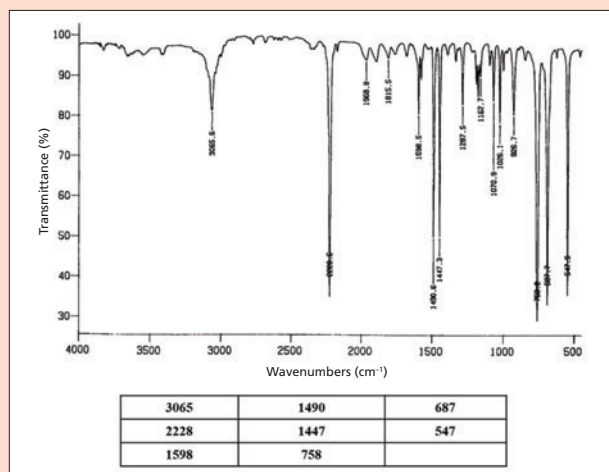


Figure ii: The infrared transmittance spectrum of a liquid—the sampling technique is thin film.

Reading the spectrum from left to right, the first significant peak we encounter is at 3065. Based on previous knowledge (13), we can conclude that this is the C-H stretch of a functional group containing unsaturated carbons. The lack of C-H stretches between 3000 and 2800 means there are no saturated carbons present, and the molecule is said to be totally unsaturated (13).

Both alkenes and benzene rings have C-H stretches between 3100 and 3000 (13). The way to distinguish them is that alkenes have a C=C stretching peak from 1680 to 1630 (13), and benzene rings have sharp, intense “ring modes” from 1620 to 1400 (14). There are no significant peaks between 1680 and 1630, but there is a series of sharp, strong peaks between 1620 and 1400, namely at 1598, 1490, and 1447. These indicate that the unsaturated carbons are part of a benzene ring.

The next thing we need to determine is the substitution pattern around the benzene ring. Recall that this is done using the position of the aromatic C-H wagging peak between 1000

and 700, and the presence or absence of an aromatic ring bend at 690 (14). In Figure ii, the C-H wagging peak is at 758, and the ring bend is at 687, indicative of mono-substitution. The four benzene fingers (15) between 2000 and 1600 confirm this is a monosubstituted benzene ring.

The final question to answer, then, is what is the substituent on the benzene ring? The biggest peak in the spectrum is the answer, the sharp feature at 2228. We learned in the last column (1) that nitriles have large, sharp C=N stretching peaks around 2200. Specifically, aromatic nitriles absorb between 2240 and 2220. The peak at 2228 then is assigned as the C=N stretch of an aromatic nitrile. Thus, we have a monosubstituted benzene ring with a nitrile substituent. There is only one molecule that fits this description, last column’s Infrared Spectral Interpretation Challenge.

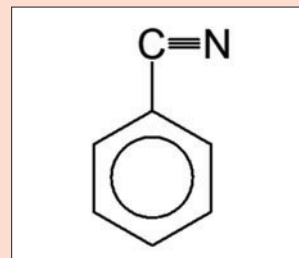


Figure iii: The chemical structure of benzonitrile, the answer to last column’s Infrared Spectral Interpretation Challenge.

The correct peak assignments for the problem are seen in Table i.

Table i: The correct peak assignment for benzonitrile.	
Peak	Assignment
3065	Aromatic C-H Stretch
2228	Aromatic C=N Stretch
1598, 1490, 1447	Aromatic ring modes
758	Out-of-plane C-H bend
687	Aromatic ring bend

For long time readers of this column, the spectrum of benzonitrile should look familiar; it has appeared in a few previous columns as an example of a spectrum with narrow peaks (6,14). Hopefully, you found this helpful.

on the broader peak. This is why the CH₂ stretches of the cyclohexyl group sit on top of the NH⁺ stretching envelope. As already mentioned, there is a series of overtone and combination bands on the right hand side of the NH₃⁺ stretching envelope. These features are common for all amine salt spectra, and the fall in the range from 2800 to 2000. Recall that carboxylic acids have a similar series of overtone and combination bands in this region, also caused by the extreme polarity of this functional group (11).

Table I lists the N-H stretching envelope positions for the three different types of amine salts. Note that there is some

overlap, particularly between primary and secondary amines.

This means that the position of the NH⁺ stretching envelope will not always disclose whether an amine salt is primary, secondary, or tertiary. So what are we to do?

Fortunately, like many other functional groups, amine salts have multiple IR features, and these come to the rescue here. In addition to NH⁺ stretching vibrations, amine salts also have NH⁺ bending vibrations as well. The NH₃⁺ grouping of primary amine salts features two peaks from the asymmetric and symmetric bending vibrations, labeled B and C in Figure 2. In

general, the asymmetric bend falls from 1625 to 1560, and the symmetric bend from 1550 to 1500. Strangely enough, these peaks are small in sharp contrast to the intense NH⁺ stretching envelope. This is all due to the difference in dμ/dx between the stretching and bending vibrations of the amine salt functional group.

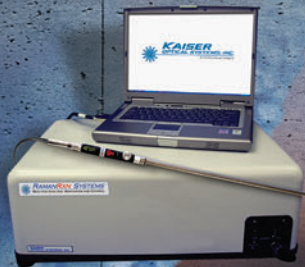
Secondary Amine Salt Spectra

Secondary amine salts contain the NH₂⁺ group. The IR spectrum of a secondary amine salt, diisopropylamine hydrochloride, is seen in Figure 5.

The NH⁺ stretching envelope is labeled

Kaiser Raman: trusted from laboratory to process

The **RAMANRXN SYSTEMS™** family of analyzers from Kaiser are robust, reliable and proven in chemical, pharmaceutical, bioprocessing and polymer applications. They are equally suited for operating within the laboratory as a research tool, in a QA/QC laboratory, in process development or in manufacturing.



Research/Process
Development



Production/
Manufacturing



KAISER
OPTICAL SYSTEMS, INC.

An Endress+Hauser Company

www.kosi.com



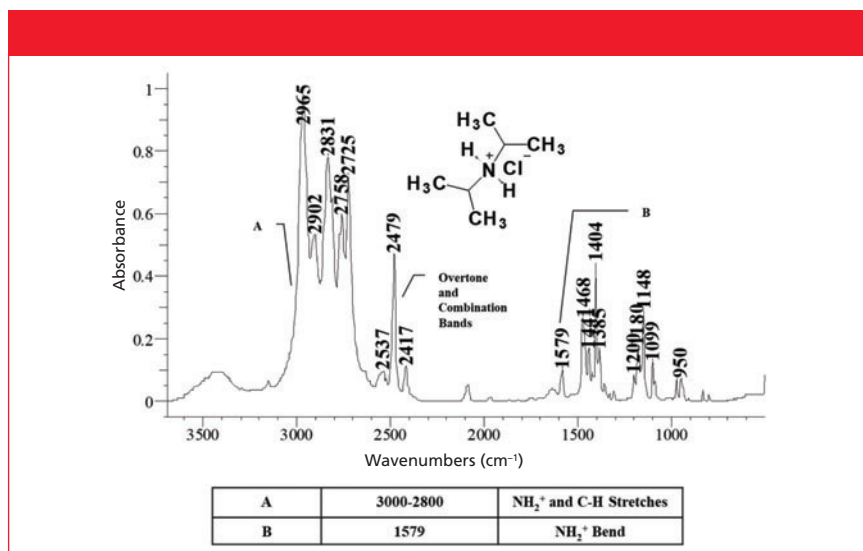


Figure 5: The infrared absorbance spectrum of a secondary amine salt, diisopropylamine hydrochloride.

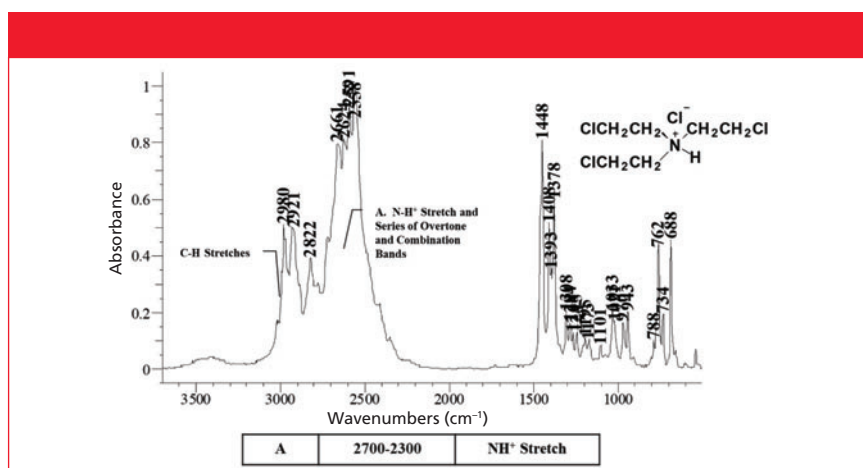


Figure 6: The infrared absorbance spectrum of a tertiary amine salt, 2,2',2''-trichloroethylamine hydrochloride.

A. Note that it is broad and strong, like the ones seen in Figures 3 and 4. As in Figure 3, the C-H stretches here also fall on top of the NH⁺ stretching envelope. It also has the expected complement of overtone and combination bands on its lower wavenumber side. For secondary amine salts in general, this envelope is found from 3000 to 2700. Note that there is some overlap between the envelopes of primary and secondary amines. However, secondary amine salts only have one NH⁺ bending band compared to primary amine salts. This feature typically falls from 1620 to 1560, and is labeled B in Figure 5. Thus the position and number of NH⁺ bending bands is what determines whether a sample contains a primary or secondary amine salt.

Tertiary Amine Salt Spectra

Tertiary amine salts contain the NH⁺ group, as seen in Figure 1. The IR spectrum of a tertiary amine salt, 2,2',2''-trichloroethylamine hydrochloride, is seen in Figure 6.

The NH⁺ stretching envelope is Figure 6 is labeled A. Note that it is lower in wavenumber than for primary and secondary amine salts, and that the C-H stretches fall as shoulders to left of the envelope peak. Given that the NH⁺ stretching envelope for tertiary amines falls squarely in the overtone-combination range from 2800 to 2000, these peaks show up on top of and as shoulders to the right of the NH⁺ stretching envelope. In general, for tertiary amine salts, this envelope falls from 2700 to 2300. The size, width, and position of this peak is practically unique in IR spectroscopy—in my decades of experience, I have never seen a peak like it (10). Thus, this peak by itself is strongly indicative of their being a tertiary amine salt in a sample. Tertiary amine salts do not have any NH⁺ bending peaks, so the lack of peaks from 1625 to 1500 can also be used to distinguish tertiary amine salts from primary and secondary salts.

We discussed previously that tertiary amines have no strong, unique peaks, and thus are difficult to detect using IR spectroscopy (12). This contrasts with tertiary amine salts, whose NH⁺ stretching envelope sticks out like a sore thumb. A way of detecting a tertiary amine in a sample then is to treat 1 mL of liquid tertiary amine, or tertiary amine dissolved in an organic solvent, with 1 mL of 50:50 HCl in ethanol. If there is a tertiary amine present, the amine

Your Next Infrared Spectral Interpretation Challenge

Your next Infrared Spectral Interpretation Challenge is seen in Figure *i*. Given its complexity, you only need to determine if there is an amine present. If so, justify your answer, and then determine the type of amine salt. Happy interpreting!

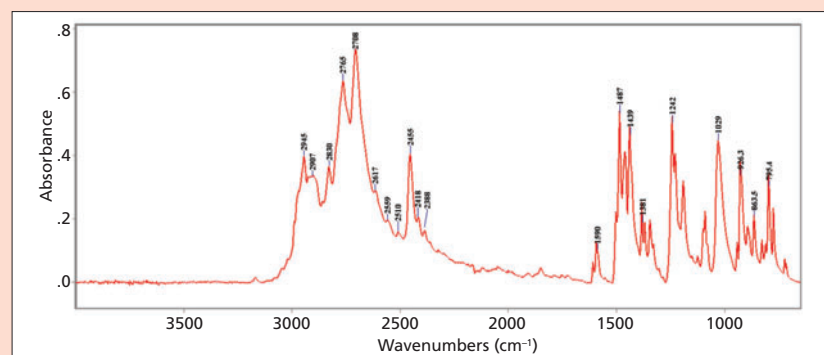


Figure *i*: The infrared absorbance spectrum of a solid.

salt will form and precipitate as a solid from solution (12). Collect the precipitate via filtration, dry, and measure its IR spectrum. If you see a big, whopping NH^+ stretching envelope like the one seen in Figure 6, your original sample contained a tertiary amine.

The group wavenumber peaks for amine salts are listed in Table I.

Conclusions

Amine salts are made by reacting amines with strong acids. Primary amine salts contain the NH_3^+ group, secondary amine salts the NH_2^+ group, and tertiary amine salts the NH^+ group. Amine salts are important, because they are used to make drug substances water soluble, and hence more bioavailable.

All amine salts contain an intense, broad NH^+ stretching envelope that is a rather unique infrared feature. The envelope position overlaps for primary and secondary amine salts, but is unique for tertiary salts. Primary and secondary amine salts can be distinguished by the number and position of NH^+ bending peaks.

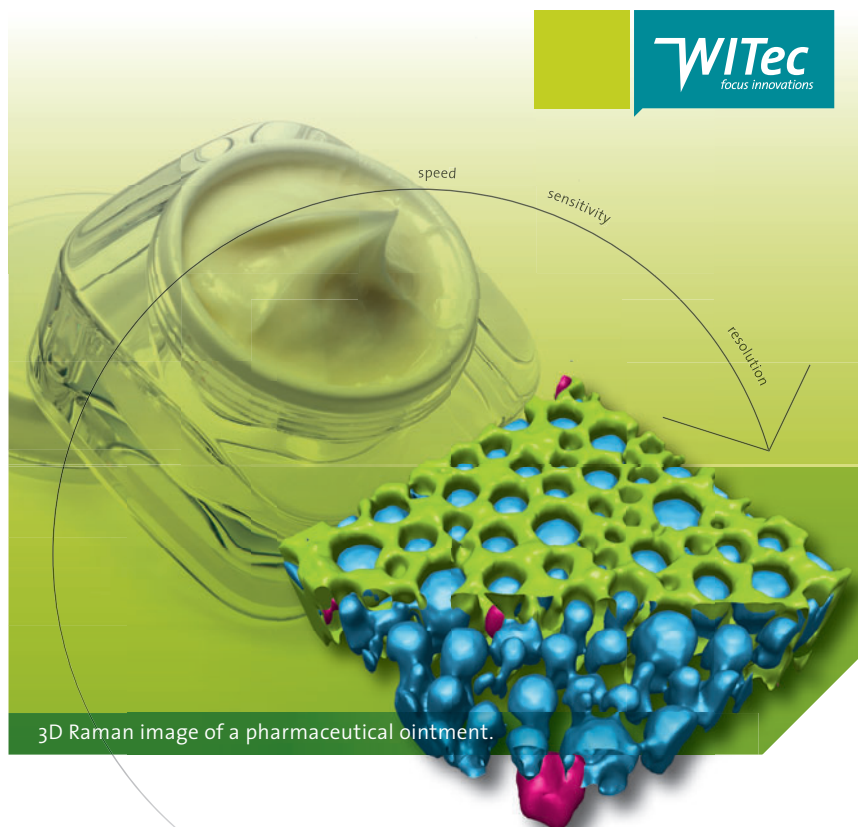
References

- (1) B.C. Smith, *Spectroscopy* **34**(7), 18–21, 44 (2019).
- (2) B.C. Smith, *Spectroscopy* **34**(5), 22–26 (2019).
- (3) B.C. Smith, *Spectroscopy* **34**(3), 22–25 (2019).
- (4) B.C. Smith, *Spectroscopy* **34**(1), 10–15 (2019).
- (5) A. Streitwieser and C. Heathcock, *Introduction to Organic Chemistry* (MacMillan, New York, New York, 1st ed., 1976).
- (6) B.C. Smith, *Spectroscopy* **30**(1), 16–23 (2015).
- (7) <https://en.wikipedia.org/wiki/Cocaine>
- (8) B.C. Smith, *Spectroscopy* **31**(7), 30–34 (2016).
- (9) B.C. Smith, *Spectroscopy* **30**(4), 18–23 (2015).
- (10) B.C. Smith, *Infrared Spectral Interpretation: A Systematic Approach* (CRC Press, Boca Raton, Florida, 1999).
- (11) B.C. Smith, *Spectroscopy* **33**(1), 14–20 (2018).
- (12) B.C. Smith, *Spectroscopy* **33**(3), 16–20 (2018).
- (13) B.C. Smith, *Spectroscopy* **31**(11), 28–34 (2016).
- (14) B.C. Smith, *Spectroscopy* **31**(5), 36–39 (2016).



Brian C. Smith, PhD, is founder and CEO of Big Sur Scientific, a maker of portable mid-infrared cannabis analyzers. He has over 30 years experience as an industrial infrared spectroscopist, has published numerous peer reviewed papers, and has written three books on spectroscopy. As a trainer, he has helped thousands of people around the world improve their infrared analyses. In addition to writing for *Spectroscopy*, Dr. Smith writes a regular column for its sister publication *Cannabis Science and Technology* and sits on its editorial board. He earned his PhD in physical chemistry from Dartmouth College. He can be reached at: SpectroscopyEdit@MMHGroup.com

For more information on this topic, please visit our homepage at:
www.spectroscopyonline.com



3D Raman image of a pharmaceutical ointment.

3D Raman Imaging

Turn ideas into **discoveries**

Let your discoveries lead the scientific future. Like no other system, WITec's confocal 3D Raman microscopes allow for cutting-edge chemical imaging and correlative microscopy with AFM, SNOM, SEM or Profilometry. Discuss your ideas with us at info@witec.de.



Raman · AFM · SNOM · RISE

www.witec.de

MADE IN GERMANY

Combined Raman Spectroscopy and Rheology for Characterizing Polymer Melts

During phase transition, the physical as well as chemical properties of polymers change dramatically. While the viscoelastic properties can usually be characterized with a rheometer, no chemical information is obtained by the mechanical testing. The interpretation of rheometric results often relies on empirical models and a more phenomenological approach. For directly relating the changes in rheological behavior to chemical changes, we employ Raman spectroscopy in situ with rheology. The phase transition from the crystalline to liquid state for different polymers was monitored for a temperature range from 70 to 150 °C. This phase transition resulted in a higher viscosity, as well as an alteration of vibrational bands in the Raman spectrum, reflecting the conversion from a crystalline to an amorphous structure. Having both viscoelastic and spectroscopic information on a sample allows a detailed characterization, and interpretation of the sample behavior on the molecular level.

Frederik Fleissner, Katharina E. Napp, Boris Wezislá, and Loredana Völker-Pop

Melting and crystallization of polymers play a pivotal role in modern industrial production processes, such as molding or extrusion. Phase transitions are often characterized by the changes in the viscoelastic properties of the material, which are determined by rheological measurements (1). However, this method only provides an indirect measure of the molecular changes, and the interpretation of results has to rely on empirical assumptions (1). This gap can be bridged by molecular spectroscopy, such as infrared (IR) or Raman spectroscopy, as these are sensitive to the chemical composition and conformation of a substance (1).

Previous studies have shown the advantage of a combination of rheology with spectroscopic techniques. Several research groups used home-built Raman-rheo setups to study the influence of tensile deformation on the C-C bonds (2) and CH₂ bending modes (3,4) in polyethylene. Epoxy curing was investigated by Farquharson and associates by simultaneously measuring the dynamic mechanical rheology and Fourier-transform Raman spectroscopy to correlate between the degree of crosslinking and macroscopic parameters such as gelation and vitrification (5). Recently, the group of Kotula at the U.S. National Institute of Standards and Technology (NIST) showed the application of a rheometer and coupled Raman microscope to study the crystallization of high-density polyethylene (6) and polycaprolactone (7).

In this study, we demonstrate the benefits of combined rheology and Raman spectroscopy, by comparing phase transitions in different types of polyethylene (PE). Polyethylenes are semicrystalline thermoplastics and are some of the most commonly used polymers in industry. Due to their favorable properties, such as ease of processing, toughness, and chemical resistance, polyethylenes have a broad range of applications, including films and packaging containers, cable insulations, and household plastics (8). Their different forms are commonly distinguished by their density (9). The main forms are high-density PE (HDPE), low-density PE (LDPE), and linear low-density PE (LLDPE). HDPE has a high molecular weight of more than 300,000, and consists of mostly unbranched polymer chains leading to a dense packing, and therefore a high degree of crystallinity in the solid state. LDPE, on the other hand, exhibits large branches with nonuniform lengths (8). The degree of crystallinity in a polymer is defined by the fractional amount of polymers in the crystalline phase present in the sample (10). Because the crystallinity of polyethylenes and their densities have a linear relationship, one usually refers to the density of the polymer.

To analyze the Raman spectra obtained during phase transitions in different PEs, we employ a chemometric approach called *multivariate curve resolution by alternating least squares* (MCR-ALS) (11,12). This approach does not require a manual selection of Raman spectra that reflect the phase transition, but

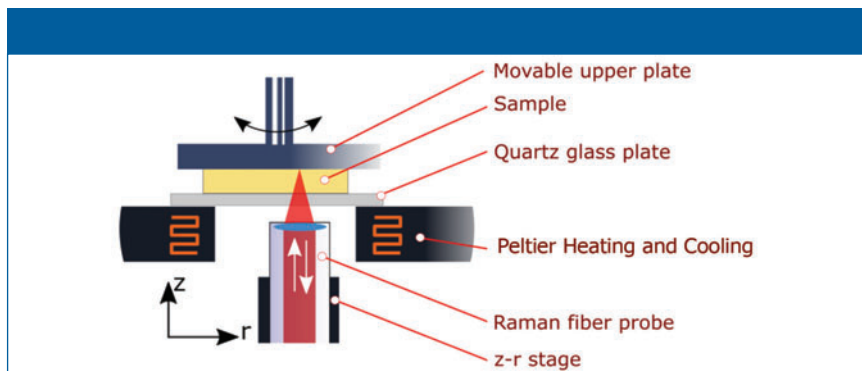


Figure 1: Schematic of the experimental setup.

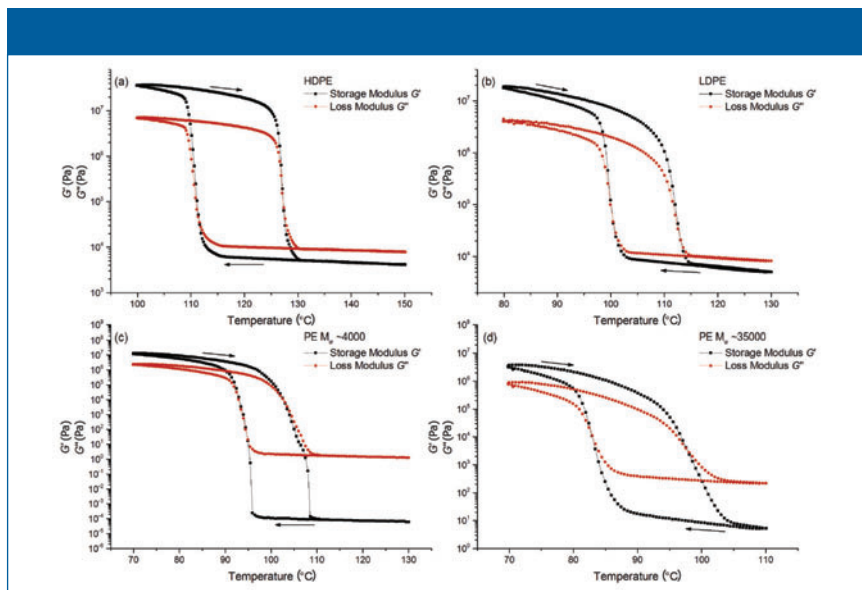


Figure 2: Comparison of the viscoelastic behavior of (a) HDPE, (b) LDPE, (c) PE $M_w \sim 4,000$, and (d) PE $M_w \sim 35,000$ over the temperature sweep measurement. The lower limit for the measurement of G' and G'' is 10^{-4} for the rheometer used.

Table 1: Polyethylene samples investigated in this study

Sample Name	Characterization	Melting Point (°C)	Density in g/mL (at 25 °C)
LDPE	Low density	116	0.925
HDPE	High density	125–140	0.952
PE M_w 4000	Average $M_w \sim 4000$ Average $M_n \sim 1700$	92	0.92
PE M_w 35,000	Average $M_w \sim 35,000$ Average $M_n \sim 7700$	90	0.906

instead calculates the “pure component spectra,” and their respective contribution of the amorphous and crystal phase at each temperature.

Methods

Instrumentation

An air-bearing-based Modular Compact Rheometer (MCR 302) (Anton Paar) was used to measure the viscoelastic properties of the samples in a plate-plate geometry. The sample temperature was varied

by a Peltier temperature device (PTD) below and above the sample area, to ensure temperature homogeneity within the sample. To prevent thermal degradation, the sample chamber was rinsed with nitrogen continuously during experiments.

A temperature sweep test from high to low temperature, and back to high temperature, was performed in oscillation at a constant frequency of 1 Hz. At high temperatures, when the sample is in melt state, a strain of 1% was applied.



Mini Rugged Spectrometers



Portable Analyzers
Raman, NIR, LIBS, Color, Radiometry



Research & Laboratory
Absorbance, Fluorescence, OES



Spectrometers
Light Sources
Accessories

SpectraWIZ Mobile App Software



813.855.8687 | www.StellarNet.us

Low Cost - Rugged - Research Quality

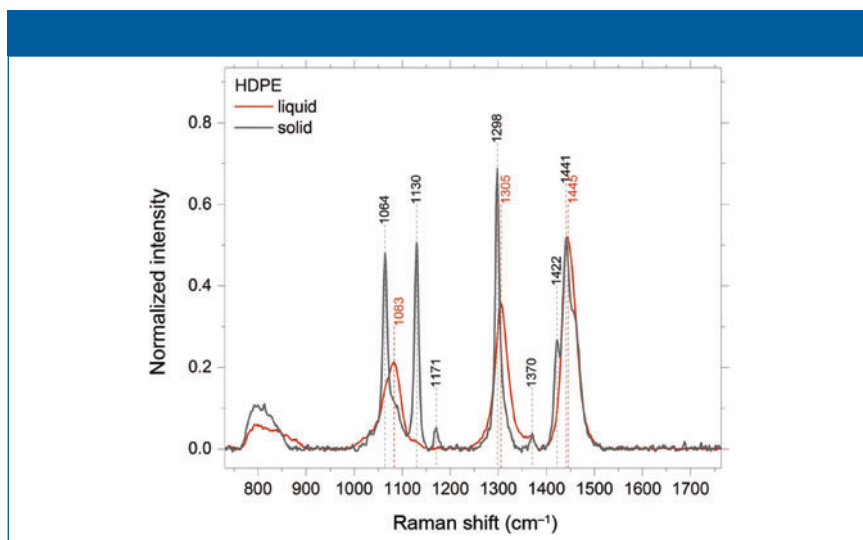


Figure 3: Raman spectra of HDPE in the liquid (red) at 150 °C and solid state (gray) at 100 °C. Both spectra were normalized to the maximum of the CH band between 2800 to 3200 cm^{-1} .

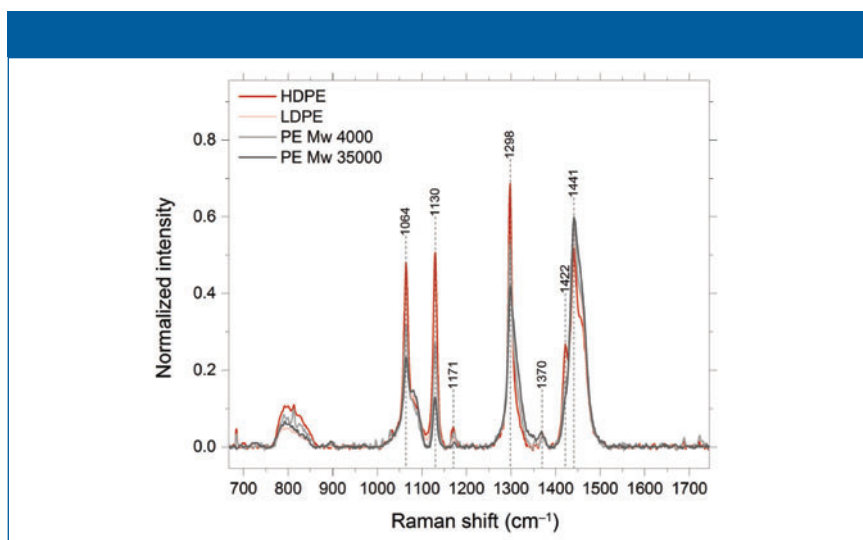


Figure 4: Raman spectra of the four polyethylene samples in the solid state.

The strain was logarithmically reduced with decreasing temperature, so that at the lowest temperature only a strain of 0.01% was applied. The strain ramp was chosen in a way that the sample response to the strain is strong enough to result in a proper signal strength, but low enough not to influence the sample behavior. When reaching the minimum temperature, a constant temperature was kept, in order to avoid thermal inertia effects.

In order to follow not only crystallization, but also the melting behavior of the sample, the temperature was increased up to the initial temperature with a heating rate of 1 °C/min.

To measure Raman spectra *in situ*, a quartz glass plate (B&M Optik GmbH), that was shown not to cause an unwanted

fluorescent background, was used as a bottom plate of the rheometer configuration. Below, an optical fiber probe resistant up to 200 °C and with a long working distance of 20 mm, optimized for the excitation wavelength of 785 nm, and free from unwanted silica background (Inphotonics) (13) was mounted on a stage moveable in a radial direction, as well as along the *z*-axis (Figure 1). Raman spectra were acquired with a Cora 7200 Raman spectrometer (Anton Paar) with an excitation wavelength of 785 nm and an optical resolution of 7 cm^{-1} . A laser power of 300 mW and an acquisition time of 3 s were employed. A spectrum corrected by a dark spectrum was obtained every 30 s over the course of the rheological test. The spectrometer

was calibrated according to the ASTM E1840 *Standard Guide for Raman Shift Standards for Spectrometer Calibration* using benzonitrile.

Sample Preparation

Different types of polyethylene were obtained from Sigma-Aldrich (see Table I), and used without further pretreatment. Before each measurement, the measuring cell was preheated to the set initial temperature. Subsequently, the granulate polymer sample was applied to the heated plate, and the hood was closed. The polymer was fully molten as judged by the normal force, a trimming was conducted, and we waited another 5 min to ensure temperature equilibrium.

Table II lists the parameters used for the rheological characterization of each polymer. For PE $M_w \sim 4,000$, the strain changed from 10% (in the liquid-like phase) to 0.01% in the rubber elastic state. For HDPE, a serrated plate of 15 mm diameter was used to prevent slippage of the sample.

Raman Data Processing

The spectral data of each experiment were pooled into a single data matrix, and processed further in self-written Python scripts. First, Raman spectra were baseline corrected with an iterative Savitzky-Golay filtering algorithm (14) to remove unwanted contributions from fluorescence. Spectral decomposition into two components was performed by using the pyMCR package (15).

Furthermore, only a rough selection of the different component spectra is necessary prior to the analysis. In the case of this study, it was assumed that there are two different phases in the systems studied, a liquid–amorphous and a crystalline phase.

Results and Discussion

Rheological Characterization

Figure 2 shows a comparison of the rheological characterization of all four polymer samples. The samples are partially crystalline polymers, showing a partially homogeneous superstructure where crystalline zones are combined with amorphous regions. An increasing temperature increases the mobility of the macromolecules in the amor-

phous regions, which leads to a decrease of the storage modulus G' , and the loss modulus G'' . When reaching the melting temperature, the crystalline zones in the polymer start to melt as well. The intersection where G'' becomes larger than G' indicates the molten state predominantly showing a viscoelastic behavior.

Each type of PE shows an individual trend of G' and G'' during cooling and heating (see Figure 2a–d) as they differ greatly in their crystallization properties. Furthermore, crystal structure and the degree of crystallization depend strongly on the heating and cooling rate, and therefore on the thermal history, of the sample. Comparing the viscoelastic properties of LDPE and HDPE (Figures 2a and 2b), it can be seen that HDPE exhibits a higher stiffness than LDPE. This is due to its lower degree of branching, and therefore higher degree of crystallinity. For HDPE, it can be expected that the crystals are also larger and more uniform than those of LDPE. Figure 2c shows the rheological characterization of the PE sample with average molecular weight of 4000. Due to the very short average chain length (average 1700 monomers per polymer), this sample exhibits the lowest viscosity of the tested PEs. The rheological characterization of the sample with average molecular weight of 35,000, and the highest polydispersity is shown in Figure 2d. The shape of the G' and G'' curves is very smooth, which confirms its lower crystallinity (1) compared to the other three samples.

Determination of Melting Points from Rheological Measurements

During the oscillatory tests, both the storage modulus G' and the loss modulus G'' are recorded. While G' describes the elastic behavior of the material, G'' , gives information about the viscous contribution of the material's behavior, due to deformation energy which is lost by the relative motion between molecules, structures, and crystals (1).

The solidification temperature, which is the crystallization temperature in case of crystal forming materials such as PE, is determined by cooling a molten sample, and finding the intersection of $G'(T)$ and $G''(T)$. Below the crystallization temperature, the sample is in a rubbery state, G' is

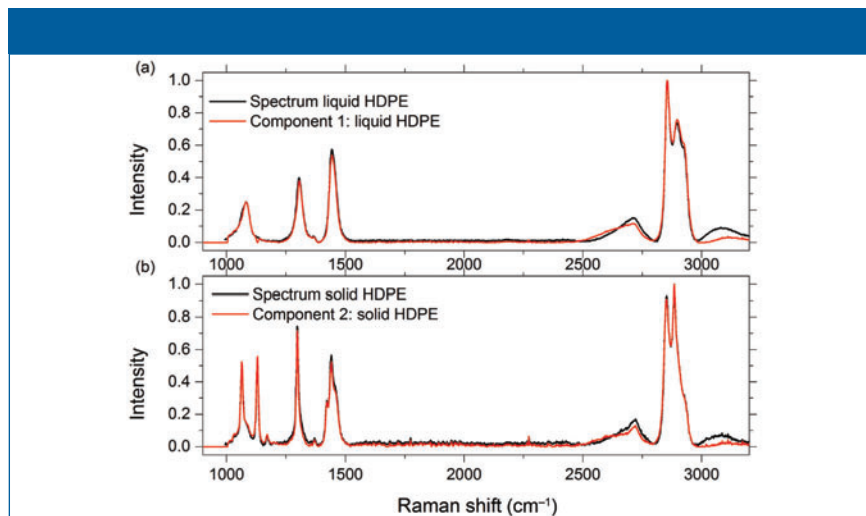


Figure 5: Raman spectra and “pure” component spectra obtained by MCR-ALS for (a) liquid and (b) solid-crystalline HDPE, showing identical spectral features.

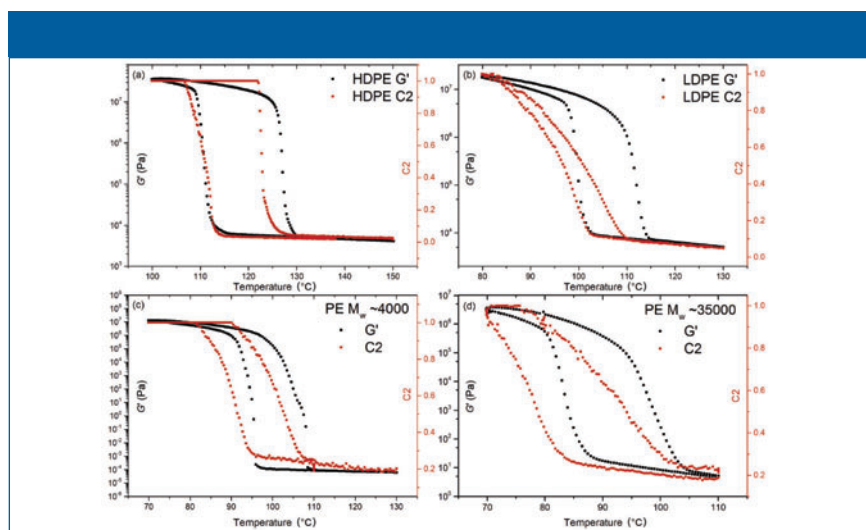


Figure 6: Correlation of the storage modulus G' from the rheological measurement and component c2 from the MCR-ALS analysis of the Raman spectra for the four different polyethylene samples.

larger than G'' , and the material responds essentially as an elastic solid. When heating the sample, the melting point is determined in a similar way by the point of intersection.

Table III shows the comparison of melting and crystallization points for the tested PE samples. The rheologically determined melting and crystallization points show the same trend as the values stated by the manufacturer. However, the respective values differ substantially, which might be caused by undercooling and overheating of the samples.

Raman Characterization

Raman spectra differ between solid and liquid HDPE. The phase transition from the solid to the liquid state is reflected by

several changes in the Raman spectra, as shown in Figure 3: The band at 1064 cm^{-1} shifts to higher wavenumber, and gets broader and lower in peak height. The peaks at 1130 cm^{-1} and 1171 cm^{-1} vanish completely. Those three bands are associated with the C-C stretching vibrations, the first is the symmetric and the last the asymmetric C-C stretching of the consecutive trans conformations within the polymer chain (3). In the solid state, the trans conformation is preferred, due to the better packing ability, while in the liquid state less ordered structures with many different conformers and a low proportion of consecutive trans conformations are present so that bands associated with trans conformation vanish (16). A similar behavior is found in the

Table II: Rheological characterization parameters

Sample	Maximum Temperature (°C)	Minimum Temperature (°C)	Cooling and Heating Rate (°C/min)	Plate Diameter (mm)	Measuring Gap (mm)
LDPE	150	100	1	15	1
HDPE	130	80	1	25	1
PE M _w 4000	130	70	1	20	1
PE M _w 35,000	110	70	1	25	1

Table III: Comparison of rheologically determined melting points with the manufacturer's statement

Melting Points (°C)	Rheo (Cooling)	Rheo (heating)	Manufacturer's Literature
HDPE	111	127	125–140
LDPE	100	113	116
PE M _w 4000	95	107	92
PE M _w 35,000	83	98	90

Table IV: Raman signals of the solid and liquid state of HDPE with assignment to the corresponding molecular vibration. Band assignment in accordance with references (3,16,18)

Solid State (Semi-Crystalline)		Liquid State (Amorphous)	
Position (cm ⁻¹)	Assignment	Position (cm ⁻¹)	Assignment
1064	ν_{as} (C-C), trans	1083	ν (C-C)
1130	ν_s (C-C), trans	1305	(C-C) twisting
1171	ν (C-C)	1445	δ (CH ₂)
1298	(C-C) twisting, crystalline	2855	ν_{as} (C-H)
1370	δ (CH ₂)	2896	ν_s (C-H)
1422	δ (CH ₂), ω (CH ₂), orthorhombic	2925	ν (C-H)
1441	δ (CH ₂) intermediate (amorphous and trans)	----	----
2721	ν (C-H)	----	----
2852	ν_{as} (C-H)	----	----
2885	ν_s (C-H)	----	----

region between 1250 cm⁻¹ and 1450 cm⁻¹. Bands associated with the crystalline state vanish (1422 cm⁻¹), or shift to higher wavenumber (1298 cm⁻¹ and 1441 cm⁻¹). A shift to higher wavenumber indicates a stronger intramolecular bond, which may be caused by weaker intermolecular interactions present in the liquid phase compared to the solid phase (17). Table IV lists the peak positions and their corresponding assignment to vibrational bands for the solid and liquid states.

Spectral Comparison of the Four Polyethylenes in the Solid State

The four polyethylene samples provide similar Raman spectra, yet several peaks vary in relative intensity (Figure 4). The polymers with a lower degree of crystallinity result in a spectral signature, which contains contributions of Raman peaks

assigned to the crystalline and amorphous state. From their relative intensities, the following qualitative order for the degree of crystallinity may be deduced:

$$\text{HDPE} > \text{LDPE} \approx \text{PE M}_w 4000 > \text{PE M}_w 35,000$$

The lower degree of crystallinity of PE M_w 35,000 compared to PE M_w 4000 matches their polydispersity indices. Furthermore, the order of crystallinity deduced from the Raman spectra is in good agreement with the density values given by the manufacturer. Because density and crystallinity are linearly correlated, the Raman spectra can be used to determine the densities of the samples relative to each other.

MCR-ALS Analysis

MCR-ALS is a popular chemometric algorithm for decomposing spectral data

matrices of mixtures into a set of pure components and their respective loadings, as it requires only little prior information about the mixture (12,19). Similar to principal component analysis, MCR finds a maximal explained variance in the spectral data of one experiment, but additionally considers constraints such as non-negativity (11,19). This is advantageous over the manual selection of unique Raman peaks, as the entire spectrum is considered to represent the target component. Furthermore, the influence of random noise is reduced by this technique as any uncorrelated signals will be ignored. For HDPE, the resulting two components representing the crystalline and liquid phases are fully reconstructed by the MCR-ALS algorithm, as shown in Figure 5, in direct comparison with the Raman spectra of the chosen state. From the obtained loadings of both components in each measurement a concentration curve over the temperature was obtained.

Correlation of the Spectral and Rheological Characterization

The component loadings found by MCR-ALS were compared with the simultaneous rheological characterization of each sample. Because the storage modulus G' and component 2 are both associated with the solid state of the polymers, a qualitative analysis of the sample properties is possible. Figure 6 shows the storage modulus G' and the behavior of component c2 over the temperature range. While G' monitors the elastic behavior of the sample, c2 is a measure for the crystalline polymers present in the sample.

For HDPE (Figure 6a), the cooling curves of both parameters show a large increase at approximately 110 °C, which indicates a direct correlation of the crystallization with the storage modulus. For the subsequent heating curve, this correlation is less pronounced. The component c2 already decreases above temperatures of 123 °C, whereas the storage modulus stays high until a temperature of 127 °C.

The Raman data show that HDPE already undergoes a transition from the semicrystalline to the fully amorphous state, while still being a solid material of high storage modulus. Given that the

Raman signals of amorphous solid and liquid do not differ substantially, the two states are not distinguished as different components in the MCR-ALS analysis.

For LDPE (Figure 6b), the determined G' and component c2 differ substantially. While the rheological measurement shows a typical hysteresis with a steep transition region, the curve for component c2 shows a very shallow slope. Kempf and colleagues monitored the transition of LDPE via rheo-Raman in 2017. Their approach featured a lower cooling rate near the transition temperature of 0.2 °C/min. They used two distinct bands of the crystalline and amorphous phases for Raman characterization. With this approach, good coincidence between rheological and Raman peak intensity curves was obtained (20). Therefore, we assume that, in the case of this experiment, the measurement parameters were not optimally chosen. The cooling and heating rate was too large for the LDPE sample. The crystallization seems to be kinetically hindered. A further study with a smaller cooling rate might resolve the difference in behavior.

PE with a molecular weight of approximately 4000 (Figure 6c) results in a behavior similar to that shown by HDPE. The Raman curve is shifted to lower temperature for the cooling as well as the heating process. Again, this fact may be correlated to a crystalline amorphous transition.

For the fourth tested sample, PE M_w 35,000 (Figure 6d), which exhibits a large polydispersity, we find that the difference in the start temperatures of the transitions between rheological and Raman curves is even larger than for the sample, PE M_w 4000. Here, the amount of crystalline phase within the fully solidified polymer is the lowest of the four samples studied. Therefore, the crystallization starts at a very late point in the measurement. The rheological curve is very smooth, which indicates that the polymer exhibits a larger number of amorphous regions than the other three samples (1).

The loading of component c2 never reaches zero for sample PE M_w 4000 and PE M_w 35,000. Because the spectra of the fully solidified samples (defined as component c2 = 1) are a superposition of the crystalline signals with a substantial

number of amorphous signals, this is an expected behavior.

Conclusion

A simultaneous rheo-Raman characterization of four different types of polyethylene was conducted by coupling a Raman spectrometer to a rheometer, via an optical fiber probe. Raman spectra of PE in its solid state yielded a trend on the crystallinity, which correlates with the density of the tested samples. By employing a chemometric analysis of the Raman data, additional information on the change of the crystallization state with temperature was obtained. It was shown that the transition to the solid phase, observed from the rheological characterization, starts at higher temperatures than the crystallization indicated by the Raman data. We therefore conclude that PE for the employed parameters first undergoes a transition from the amorphous liquid to an amorphous solid state, and later on starts to crystallize.

Acknowledgements

We are grateful to Alexander Klutz, Thomas Mezger and Roman Führer for helpful and critical discussions.

References

- (1) T.G. Mezger, *The Rheology Handbook* (Vincenz Network GmbH and Co KG, Hannover, Germany, 2nd Ed., 2006).
- (2) C.K. Chai, N.M. Dixon, D.L. Gerrard, and W. Reed, *Polymer* **36**(3), 661–663 (1995).
- (3) T. Kida, Y. Hiejima, and K. Nitta, *Int. J. Exp. Spectroscopic. Tech.* **1**(1), (2016).
- (4) T. Kida, Y. Hiejima, and K. Nitta, *Polym. Int.* **67**, 335–340 (2018).
- (5) S. Farquharson, J. Carignan, V. Kitrov, A. Senador, and M. Shaw, *Proc. of SPIE*, 5272 (2004).
- (6) A.P. Kotula, M.W. Meer, F. De Vito, J. Plog, A.R. Hight Walker, and K.B. Migler, *Rev. Sci. Instrum.* **87**, 105105 (2016).
- (7) A.P. Kotula and K. B. Migler, *J.Rheol.* **62**(1), 343–356 (2018).
- (8) K.S. Whiteley, *Ullmann's Encyclopedia of Industrial Chemistry* (Wiley-VCH Verlag GmbH, Weinheim, Germany, 2012), pp. 2–37.
- (9) C. Vasile and M. Pascu, *Practical Guide to Polyethylene* (Rapra Technology Press, Srewsbury, United Kingdom, 2005).
- (10) M. Nic, J. Jirat, and B. Kosata, *The IUPAC Gold Book*, online (2017).

- (11) R. Tauler, *Chemom. Intell. Lab.Syst.* **30**, 133–146 (1995).
- (12) J. Felten, H. Hall, J. Jaumot, R. Tauler, A. de Juan, and A. Gorzsás, *Nature Protocols*, **10**(2), 217 (2015).
- (13) C. Wang, L. Zeng, Z. Li, and D. Li, *J. Raman Spectrosc.* **48**(8), 1040–1055 (2017).
- (14) J. Zhao, H. Lui, D.I. McLean, and H. Zeng, *Appl. Spectrosc.* **61**(11), 225 (2007).
- (15) C.H. Camp, *J. Res. Natl. Inst. Stan.* 124:124018. <https://doi.org/10.6028/jres.124.018> (2019).
- (16) Y. Jin, A.P. Kotula, C.R. Snyder, A.R. Hight Walker, K.B. Migler, and Y. Jong Lee, *Macromolecules* **50**, 6174–6183 (2017).
- (17) G.A. Voyiatzis and G.N. Papatheodorou, *Ber. Bunseng. Phys. Chem.* **98**, 683–689 (1994).
- (18) K.B. Migler, A.P. Kotula, and A.R. Hight Walker, *Macromolecules*, **48**, 4555–4561 (2015).
- (19) C. Ruckebusch and L. Blanchet, *Anal. Chim. Acta* **765**, 28–36 (2013).
- (20) M. Kempf, B. Dippel, and O. Arnolds, *Ann. Trans. Nord. Rheol. Soc.* **25**, 81 (2017).

Frederik Fleissner, Katharina E. Napp, and Boris Wezislá are with Anton Paar OptoTec GmbH, in Seelze-Letter, Germany. **Loredana Völker-Pop** is with Anton Paar Germany GmbH, in Ostfildern-Scharnhausen Germany. Direct correspondence to frederik.fleissner@anton-paar.com ■


For more information on this topic, please visit our homepage at: www.spectroscopyonline.com

Spectroscopy

SHOWCASE


Low Frequency Raman Filters

Stokes and anti-Stokes modes at 5 cm⁻¹ and up



Available wavelengths 400-2500 nm

405, 442, 458, 473, 488, 491, 514, 532, 552, 561, 568, 588, 594, 632, 660, 785, 830, 980, 1064, 1550



PRODUCTS & RESOURCES

In-situ reaction monitoring analyzer

ABB's MB-Rx in situ reaction monitoring analyzer is designed to provide plug-and-play analyses for research laboratories and pilot plants. According to the company, the analyzer offers chemists direct access to real-time experiment data via an insertion probe and an intuitive software interface.

ABB Measurements & Analytics,
Quebec, Canada;
www.abb.com/analytical



Graphite furnace tubes

REFLEX Analytical's precision fabricated atomic absorption (AA) graphite furnace tubes are designed with high-purity, high-density graphite and coated with a layer of pyrolytically-deposited graphite. According to the company, the graphite tubes provide a dense and durable surface that is impervious to sample, vapor, or solvent.

REFLEX Analytical Corporation, Ridgewood, NJ;
www.reflexusa.com/pycgrfutu.html



Raman spectroscopy biological analysis brochure

A brochure available from Renishaw (BR015(EN)-01-A) is designed to provide information and answers to questions about the use of Raman spectroscopy and imaging in biological analysis. Topics and applications discussed in the brochure include research and clinical, cytology, proteomics and genomics, tissue and biofluid diagnostics and pathology, and bone, teeth, and cartilage, and the company's RA816 biological analyzer. **Renishaw plc,** Gloucestershire, UK; www.renishaw.com



CRMs for spectrophotometer qualification

Starna's range of certified reference materials (CRMs) for UV-visible spectrophotometer qualifications are designed to provide tailored solutions, advice, and support for a given situation. According to the company, the CRMs can help users of UV-vis spectrophotometers comply with the new editions of *U.S. Pharmacopeia* Chapter <857> and *European Pharmacopoeia* Chapter 2.2.25.

Starna Cells Inc., Atascadero, CA; www.starnacells.com



Ad Index

ADVERTISER

PG#

ABB, Inc.....	5
Amptek.....	7
Art Photonics GmbH.....	11
Bayspec Inc.....	CV4
B&W Tek LLC.....	15
Bio-Rad Laboratories, Inc.....	9
CEM Corporation.....	CVTIP, 47-48
Eastern Analytical Symposium.....	20
EDAX, Inc.....	23
Edinburgh Instruments.....	25
Harrick Scientific Corporation.....	51
Kaiser Optical Systems, Inc.....	35
Metrohm USA.....	CV3
Moxtek, Inc.....	49
Ocean Insight.....	CV2, 52
Ondax.....	13
OptiGrate Corporation.....	43
PIKE Technologies.....	19, 53
Renishaw, Inc.....	8
Rigaku GMG.....	17, 50
Scientific Cell Company.....	31
Society for Applied Spectroscopy.....	33
Specac.....	3
Starna Cells, Inc.....	21, 27
Stellar Net, Inc.....	39
Wasatch Photonics, Inc.....	29
WITec GmbH.....	37, 54

Supplement to

Spectroscopy[®]

Solutions for Materials Analysis

September 2019

www.spectroscopyonline.com



THE APPLICATION NOTEBOOK

THE APPLICATION NOTEBOOK

Atomic Spectroscopy

47 Microwave Digestion and Trace Metals Analysis of Cannabis and Hemp Products

Samuel Heckle and Leanne Anderson, CEM Corporation

49 High Voltage Accuracy and Precision on Small Compact X-ray Sources

Sterling Cornaby, Moxtek

50 Analysis of Organic Chlorides in Crude by ASTM D4929 Part C

Applied Rigaku Technologies, Inc.

Molecular Spectroscopy

51 A Diamond ATR Study of Worn Surfaces on Metal

Susan Berets, Harrick Scientific Products, Inc.

52 Trace-Level Pesticide Detection Utilizing Surface-Enhanced Raman Spectroscopy (SERS)

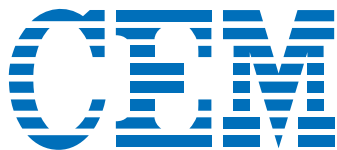
Anne-Marie Dowgiallo, Ocean Insight

53 Observation of Methanol in Ethanol Using Automated ATR Spectroscopy

Kyle J. Czech and Jenni Briggs, PIKE Technologies

54 Microparticles in Focus

Miriam Böhmler, Damon Strom, and Eleni Kallis, WITec GmbH



Microwave Digestion and Trace Metals Analysis of Cannabis and Hemp Products

Samuel Heckle and Leanne Anderson, CEM Corporation

In 1970, marijuana was designated a Schedule 1 drug, under the Controlled Substances Act, making it nearly impossible for laboratories to perform cannabis research. However, medicinal use of cannabis is now legal in Canada and 33 U.S. states. With the passage of the Farm Bill in 2018, it is now federally legal to grow and process hemp in all 50 states. All of this interest in medical cannabis and cannabidiol (CBD) has highlighted the need for good analysis methodology in this relatively young market. Cannabis analysis is still developing standardized protocols, requirements, and acceptable testing practices. Typical testing requirements for cannabis and its products include analysis of heavy metal, pesticide residues, and the potency of active ingredients such as tetrahydrocannabinol (THC). The terpene content of cannabis is also important. Terpenes have been shown to have beneficial uses for treatment of conditions ranging from cancer and inflammation to anxiety and sleeplessness. It is believed that the combination of terpenes and cannabinoids in cannabis produce a synergistic effect with regards to medical benefits.

Certain heavy metals can cause adverse effects on human health. Toxic heavy metals such as arsenic, cadmium, lead, and mercury are persistent once released into the environment and can accumulate in cannabis plants. Since hemp is a strain of cannabis that contains very little THC, it is susceptible to bioaccumulation of heavy metals like its THC-containing relative. Cannabis-based products such as foods, oils, tinctures, and salves should be tested for the presence of heavy metals to ensure patient safety and product quality. Cannabis and CBD-infused products have grown in popularity in states that allow recreational use of cannabis and hemp. This application note details the digestion

Table I: Preparation of hemp and cannabis samples

Sample	Preparation
Peanut butter	Placed on plastic spatula to deposit on bottom of vessel
CBD oils	Deposited on bottom of vessel with plastic pipette
Fruit snack	Cut in half with ceramic scissors
Topical cream	Placed on plastic spatula to deposit on bottom of vessel
Granola bar	Crushed
Chocolate raisins	Whole
Flower	Torn into small pieces

Table II: ICP-OES conditions

Parameter	Agilent 5110 ICP-OES
Plasma viewing mode	Axial
Read time	30 s
Measurement replicates	3
RF incident power	1400 W
Plasma argon flow rate	12 L/min
Nebulizer argon flow rate	0.7 L/min
Auxiliary argon flow rate	1.0 L/min
Inner diameter of the torch injector	2.0 mm
Nebulizer type	Concentric glass (Meinhard)
Spray chamber type	Class cyclonic spray chamber
Stabilization time	25 s

Table III: Spike recoveries of cannabis samples

Sample	As (%)	Cd (%)	Hg (%)	Pb (%)
Topical cream	104.7	105.6	101.8	102.2
Fruit snack	105.0	106.1	99.7	91.0
Cannabis flower	106.8	102.0	95.6	102.5
CBD oil 4.5k	101.5	101.3	92.3	102.6
CBD oil 6k	100.9	100.4	91.9	101.8

and analysis of various forms of hemp and cannabis products.

Instrumentation

A CEM MARS™ 6 microwave digestion system was used to digest the varied cannabis and hemp sample types. The MARSXpress™ Plus vessels with disposable glass inserts use a vent and reseat design, which allows for acid vapors to be exhausted while maintaining the sample integrity and elements within the vessel. The 110-mL vessel volume provides for a larger headspace, allowing a larger sample size for a more homogenous sample. The MARSXpress Plus vessel design uses only three pieces that are easily assembled and placed in a 24-position turntable, prior to placing into the MARS 6 system. The glass insert provides an inexpensive disposable vessel that eliminates the need for vessel cleaning.

Procedure and Method

All samples required special preparation, based on the qualities of each sample, in order to obtain a homogenous 0.25 g approximate

Table IV: Elemental content of samples

Sample	As ($\mu\text{g/g}$)	Cd ($\mu\text{g/g}$)	Hg ($\mu\text{g/g}$)	Pb ($\mu\text{g/g}$)
Topical cream	0.0003	0	0.0013	0.0003
Fruit snack	0.0050	0	0.0007	0.0003
Cannabis flower	0.0033	0.0020	0.0007	0.0003
CBD oil 4.5k	0.0007	0	0	0.0007
CBD oil 6k	0.0013	0	0.0003	0.0003

Table V: Medical action levels for the state of California

Medical Action Levels*	As ($\mu\text{g/g}$)	Cd ($\mu\text{g/g}$)	Hg ($\mu\text{g/g}$)	Pb ($\mu\text{g/g}$)
Edible cannabis products	1.5	0.5	3.0	0.5
Inhaled cannabis products	0.2	0.2	0.1	0.5
Topical products	3.0	5.0	1.0	10.0

sample weight. It is important to carefully deposit the oil, cream, and peanut butter, in order to not get the sample stuck to the sides of the vessel. For peanut butter and cream, a long plastic spatula was used to deposit the sample on the bottom of the liner. For the oil, the sample was deposited to the bottom of the vessel with a plastic pipette. Then, the inside of the liner was washed down with the acid to make sure all the sample got to the bottom. Table I shows the seven samples that were digested and the preparation method used, prior to placing them into the vessels.

Ten mL of HNO_3 was added to each vessel and then allowed to predigest for 15 min prior to sealing and placing the vessel in the turntable. The turntable was then placed in the MARS 6 and the Glass Cannabis One Touch™ Method was chosen on the touchscreen. The MARS 6 then counted the number of vessels and applied the precise power required to achieve the optimal digestion temperature of 200 °C. This temperature ensured the complete digestion of the samples, prior to analysis.

Samples were prepared in two batches. One batch was spiked with a spike solution containing between 0.4 and 1 ppm As, Hg, Cd, and Pb. The second batch was left unspiked. All samples were run in triplicate with blanks in each run. Upon successful digestion all samples were diluted to 50 mL with deionized water for analysis.

All samples were analyzed on an Agilent 5110 ICP-OES to determine spike recoveries and actual sample content of the “big

four” heavy metals of As, Cd, Hg, and Pb. Instrument conditions are detailed in Table II.

Results and Discussion

The MARS 6, with MARSXpress Plus vessels with disposable glass inserts, was able to successfully digest all samples in a mixed batch. All of the samples were completely digested, yielding clear and particulate-free solutions upon dilution with deionized water. The MARS 6 is an ideal digestion system for the cannabis industry because it is able to successfully digest batches of mixed materials, including foods, oils, tinctures, creams, and plant materials, in as little as 35 min.

After confirmation of the method through a spike recovery study, unspiked samples were analyzed for their total trace metals content using the same technique. Table IV shows the trace metals content of unspiked samples. Table V contains the California action levels for medical cannabis samples. It is worth noting that all of the unspiked samples contained far less than the maximum allowable limit for each element.

Conclusions

The MARS 6 with MARSXpress Plus vessels with disposable glass inserts was able to digest a wide variety of cannabis and hemp samples in mixed batches producing digestate that was suitable for analysis. Analysis of all samples showed excellent spike recovery and gave great confidence in the actual levels of trace metals in the unspiked samples.

CEM Corporation

P.O. Box 200, Matthews, NC 28106
tel. (704) 821-7015, fax (800) 726-3331

Website: www.cem.com



High Voltage Accuracy and Precision on Small Compact X-ray Sources

Sterling Cornaby, Moxtek

Moxi™ X-ray source is calibrated to within ± 250 V over all settings between 5 to 50 kV. This impressive accuracy and precision is achieved spectroscopically, by measuring an X-ray spectrum's bremsstrahlung edge and storing correction high voltage offset information on each source.

One optimization desired by manufacturers of X-ray fluorescent (XRF) instruments is X-ray sources that are spectroscopically identical. A spectroscopically identical X-ray source allows one to switch out an X-ray source in an instrument with no other changes to the instrument, for example, with minimal or no recalibration of the instrument. This benefit is desired by handheld XRF manufacturers, which reduces XRF calibration effort and service time for XRF instruments. Each Moxi™ X-ray source is calibrated to within ± 250 V over all settings between 5 to 50 kV. This voltage accuracy is tight enough to allow for XRF equivalence for several XRF applications.

Experimental Conditions

In order to calibrate an X-ray source, two basic requirements are needed:

- A meaningful and accurate way to measure the high voltage.
- A way to store the high-voltage calibration information on each X-ray source, offsetting source-to-source differences due to variance in the source's electrical components.

The X-ray source's high voltage is measured by collecting an X-ray spectrum from the tube's anode. The source is pointed directly at an

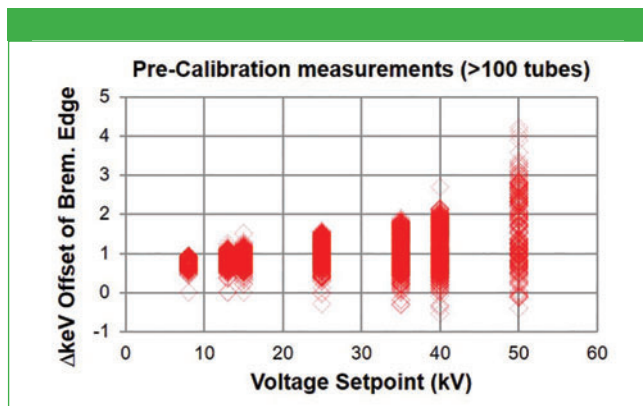


Figure 1: This graphic shows the offset between the tube's set voltage and bremsstrahlung edge over seven settings' precalibration, on over 100 separate X-ray sources. Precalibration, the high voltage is typically offset by 800 V, and can vary by up to ± 1000 V (@35 kV).

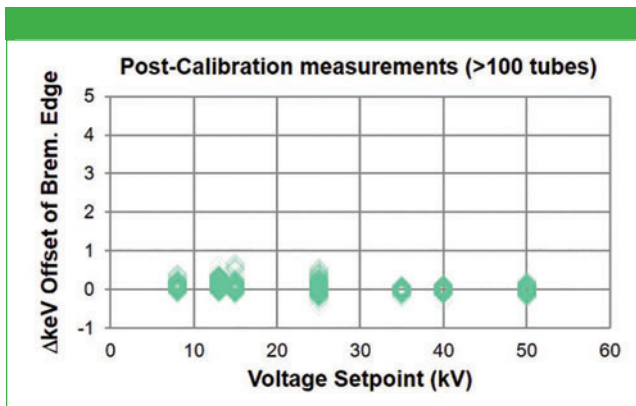


Figure 2: This graphic shows the offset between the tube's set voltage and bremsstrahlung edge over seven settings post-calibration, on over 100 separate x-ray sources. Post-calibration, the high voltage is typically offset by 100 V, and can vary by up to ± 250 V (@35 kV).

energy-dispersive detector, with a pinhole in-between to limit the intensity from the X-ray source. The spectrum's bremsstrahlung edge is fit with a proprietary algorithm, giving the value of the bremsstrahlung edge in keV. This measurement provides the "spectroscopic" voltage in keV, while the electronic monitors on the X-ray source give an electronically measured voltage in kV. The difference between the two gives a correction factor, which can be used to tighten the accuracy and precision between these two values. This test is repeated over several tube voltage settings between 5 and 50 kV.

The variance in the electronic components in aggregate is the major driving factor for the high-voltage inaccuracy of any particular X-ray source. The electronic components have a partially nonlinear relationship with high voltage. The Moxi™ X-ray source has an onboard memory which can hold a correction factor to correct for the nonlinear relationship.

Results

Comparing Figures 1 and 2 shows the accuracy and precision of the high voltage on the X-ray sources is drastically increased by the high-voltage calibrating procedure. These graphs are intentionally at the same scale to easily show the improvements.

Conclusions

Moxi™ X-ray sources are an "XRF equivalent" X-ray source for XRF instrument manufacturers. The key aspect for achieving this source's spectral equivalence is the high-voltage calibration of the source. Each digital X-ray source is calibrated to within ± 250 V over all settings between 4 to 50 kV. The high accuracy and precision is achieved spectroscopically by measuring the bremsstrahlung edge and storing high-voltage offset information on each source. This benefit is very much desired by handheld XRF manufacturers and reduces XRF calibration effort and service time for XRF instruments. This quantification has practical backing; it is working as intended in next-generation XRF handheld instruments sold today.

Moxtek, Inc.

452 West 1260 North, Orem, UT 84057
tel. (801) 225-0930, fax (801) 221-1121

Website: www.moxtek.com



Analysis of Organic Chlorides in Crude by ASTM D4929 PART C

Applied Rigaku Technologies, Inc.

The analysis of organic chloride in crude is demonstrated per ASTM D4929 Part C using Monochromatic EDXRF (MEDXRF).

Chlorides in crude contribute to corrosion in the piping at refineries during cracking as well as mid-stream in pipelines. Organic chlorides do not naturally occur in crude, however inorganic chlorides in the form of salts as well as residual organic chlorides from various natural sources as well as adulteration can contaminate crude. Contracts at the pipelines may contain clauses limiting the amount of organic chloride allowed in the crude. And at the refinery after desalting and desulfurization, crude needs to be analyzed for any residual organic chlorides possibly still entrained in the feedstock to avoid potential damage during the refining process.

Experimental Conditions

Instrumentation

Type:	Monochromatic EDXRF (MEDXRF) 90° Cartesian Geometry Polarization
Model:	Rigaku NEX CG
X-ray tube:	50 W Pd-anode
Detector:	Silicon drift detector (SDD)
Sample tray:	15-position Autosampler
Film:	Polypropylene (4 um)

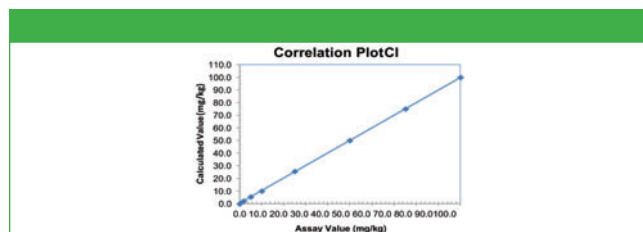


Table I: D4929 Part C XRF Calibration

Element: Cl RMS: 0.212
Units: mg/kg Correlation: 0.99999

Sample ID	Standard Value	Calculated Value
1	0.0	0.0
2	2.0	2.0
3	5.0	5.3
4	10.0	9.8
5	25.0	25.3
6	50.0	49.8
7	75.0	74.9
8	100.0	100.1

Table II: Precision and Repeatability

Element: Cl		Units: mg/kg			
Sample ID	Standard Value	Average Value	Standard Deviation (1σ)	Instrument r	D4929-17 Part C MEDXRF r
2	2.0	1.86	0.09	0.25	0.8
3	5.0	4.97	0.09	0.25	1.2
4	10.0	10.1	0.1	0.28	1.6
8	100	99.3	1.1	3.1	4.5

Table III: Detection Limits

Element	LLD
Cl	0.18 mg/kg

Lower Limit of Detection (LLD)

Analysis Time: 300 s

Environment: Helium

Sample Preparation

ASTM D4929 is designed for the measurement of residual organic chlorides in crude. The crude sample is first prepared by distillation and wash to remove H₂S and inorganic chlorides. After distillation and wash processes the resulting naphtha fraction is analyzed for Cl content by XRF using Part C methodology. The naphtha fraction is typically stable containing less than 1000 mg/g S. XRF calibration is made using mineral oil calibration standards, as mineral oil models naphtha for X-ray response.

To prepare a sample for XRF analysis simply place 4.0 g of the naphtha sample in a standard 32-mm XRF sample cup and measure directly.

ASTM D4929 Calibration: Part C XRF

Empirical calibration was made using commercially available mineral oil standards. For optimum calibration, the standards contain both S and Cl, with S content ranging from 100 to 1000 mg/kg (Table I). Alpha corrections are automatically employed to compensate for sulfur's effect on chlorine X-rays.

Precision and Repeatability

To demonstrate recovery, precision, and repeatability of the measurement, a few calibration standards were selected with results shown in Table II.

Detection Limits

The empirical method is used to determine detection limits using 300 s measurement time. Ten repeat analyses of a blank mineral sample are taken with the sample in static position and the standard deviation (σ) is determined. The lower limit of detection (LLD) is then defined as three times the standard deviation (3σ) as in Table III.

Conclusions

The performance shown here demonstrates NEX CG provides excellent sensitivity and performance for the measurement of chromium conversion coatings on aluminum.

Applied Rigaku Technologies, Inc.

9825 Spectrum Drive, Bldg. 4, Suite 475, Austin, TX 78717

tel. (+1) 512-225-1796

Website: www.RigakuEDXRF.com



A Diamond ATR Study of Worn Surfaces on Metal

Susan Berets, Harrick Scientific Products, Inc.

Tribology—the study of friction, wear, and lubrication—is important in mechanical, electromechanical, and biological systems. Changes in materials due to abrasion, friction, lubrication, erosion, and corrosion result in failures of the moving components during use. These effects are usually minimized by careful surface finish design and lubrication. Recycling and refinishing surfaces can extend the lifetimes of components. By examining worn surfaces, better methods can be developed to prevent wear. This applications note uses infrared spectroscopy to study tribology changes in steel.

Experimental

The sample investigated was 28 mm in diameter by 8 mm thick with a carbon-based coating. The sample was lubricated, tested, and then cleaned with n-heptane, leaving chemisorbed species in the wear scratches on the surface.

The spectra of the disc were measured on an FT-IR spectrometer equipped with the Harrick VideoMVP™ (see Figure 1). The background spectrum was collected from the clean ATR crystal. Then the sample was placed, face down, on the diamond crystal and positioned over the area of interest using the image on the display. The pressure applicator was lowered to apply ~240 N of force to compress the sample against the crystal. The spectrum and image were then recorded. All spectra were collected from 4000 to 400 cm^{-1} using 32 scans at 8 cm^{-1} resolution.

Results and Discussion

Figure 2 shows spectra measured from a section with wear scratches in comparison to a shiny smooth section, along with

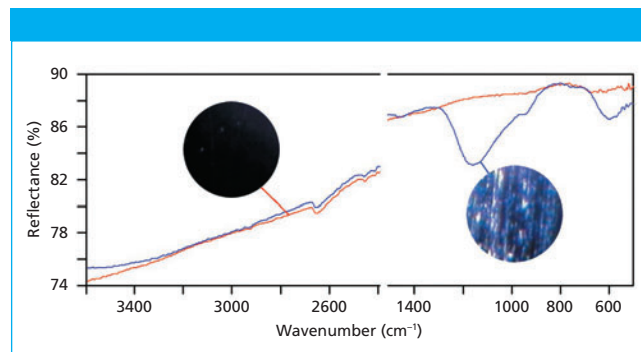


Figure 2: ATR spectra and photographs of an unworn area (red) and a worn area (blue) of a flat metal part.

photographs of the areas of each sample that were examined. The infrared spectrum of the wear scratches show a weak broad band in the $-\text{OH}$ stretching region and additional bands at 1450 cm^{-1} , 1165 cm^{-1} , 943 cm^{-1} , and 605 cm^{-1} , all of which are not present in the unworn section. This indicates that a residue from the lubricant or chemisorbed species remains in the worn area. More detailed analysis could be used to identify the chemisorbed species.

Conclusion

The results presented here clearly show that diamond ATR can be used to examine tribology materials. The viewing capabilities and small sampling area of the VideoMVP allow for inspection of the wear scratches in comparison to the unworn areas.



Figure 1: The VideoMVP™ Diamond ATR.

Harrick Scientific Products, Inc.

141 Tompkins Ave., Pleasantville, NY 10571
tel. (914) 747-7202, fax (914) 747-7409

Website: www.harricksci.com

Trace-Level Pesticide Detection Utilizing Surface-Enhanced Raman Spectroscopy (SERS)

Anne-Marie Dowgiallo, Ocean Insight

Several pesticides were detected at parts-per-million levels on apple skin using a unique swabbing method and surface-enhanced Raman spectroscopy (SERS).

Commonly used pesticides, such as organothiophosphates and fungicides, can attack the central nervous system, posing a risk to humans and other animals upon exposure (1). SERS has been investigated as a technique to detect trace levels of pesticides on food items, and offers reduced instrument size, fast measurement times, non-destructive sampling, and simple implementation compared to the traditionally used methods, such as HPLC and GC-MS (2). In this study, we utilize a swabbing technique that has the potential to be a testing platform for field use to detect trace levels of pesticides on apple skin.

Experimental Conditions

Pesticide-containing apple skin pieces are swabbed and added to colloidal gold nanoparticles. The mixtures are interrogated with 785 nm excitation laser with 3 s integration time and 350 mW laser power, and the Ocean Insight QE Pro spectrometer.

Results

The pesticides examined in this study were thiram, malathion, acetamiprid, and phosmet. The SERS spectra of each pesticide after being applied to apple skin and swabbed are presented in

Figure 1. The observed peaks are consistent with reports in the literature.

Conclusions

We present a swabbing technique that has the potential to be a testing platform for field use and utilizes colloidal gold to detect trace levels of several pesticides on apple skin. This technique can detect each pesticide down to 1 ppm, where the pesticide residue tolerances on apples are 5 ppm, 8 ppm, 1 ppm, and 10 ppm for thiram, malathion, acetamiprid, and phosmet, respectively (3). The results presented here indicate that SERS coupled with the swab method is a valuable tool, and has significant potential for identifying pesticide residues on the surface of fruits for food quality and safety control.

References

- (1) M. Stoytcheva, *InTech*, 30–48 (2011). doi: 10.5772/1003.
- (2) M.L. Xu, Y. Gao, X.X. Han, and B. Zhao, *J. Agric. Food Chem.* **65**, 6719–6726 (2017).
- (3) Office of the Federal Register, *Electronic Code of Federal Regulations*, 2018, <https://www.ecfr.gov> (8 January 2019).

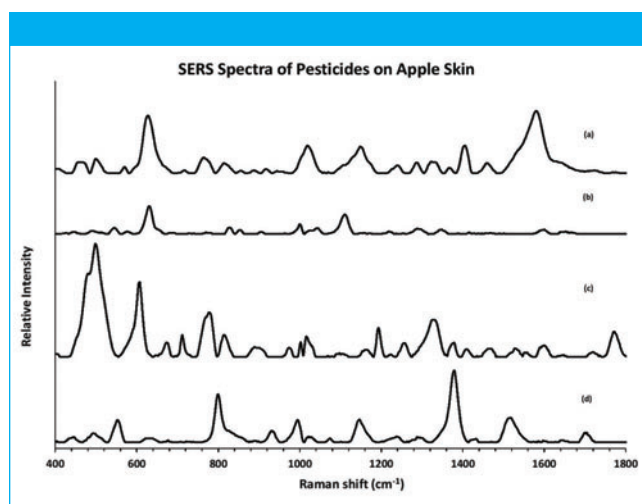


Figure 1: SERS spectra of swabs of 1 ppm (a) malathion, (b) acetamiprid, (c) phosmet, and (d) thiram on apple skin.

Ocean Insight

8060 Bryan Dairy Road, Largo, FL 33777

tel. +1 (727) 733-2447

Website: www.oceaninsight.com

Observation of Methanol in Ethanol Using Automated ATR Spectroscopy

Kyle J. Czech and Jenni Briggs, Ph.D, PIKE Technologies

Mixtures of methanol in ethanol were investigated using an automated ATR accessory. The spectral bands of methanol and ethanol were evaluated showing the expected absorbance changes.

Quantitation of contaminants and toxins within human-consumable products is a critically important aspect of ensuring consumer safety. Methanol contamination of consumable alcoholic beverages is particularly concerning due to the acute toxicity of methanol, with 4 mL of ingested methanol leading to irreversible vision loss and 30 mL of methanol potentially resulting in death (1). Recently, headlines discussing deaths and injuries linked to methanol contamination of commercially available liquors at popular resorts have emphasized the importance of methanol screening and quantitation methodologies.

Here, we use PIKE Technologies' automated ATR accessory, the AutoATR, to observe the spectral changes over various concentrations of methanol in ethanol (Figure 1). The AutoATR uses 24 unique Si ATR elements, which have a thickness of 500 microns. The thin profile of the ATR crystal minimizes absorption of the IR source by the Si phonon bands which, in combination with the accessory's base optics, results in high energy throughput and reproducibility.

Sampling automation is made possible by the AutoPRO7 software package. AutoPRO7 streamlines the collection of all background and sample spectra, reducing the required user involvement to the distribution of samples after the background spectra acquisition has completed.

Experimental Details

A series of five concentrations of methanol in ethanol were investigated, including 0, 10, 20, 30, and 40% *v/v* methanol in ethanol. Each



Figure 1: PIKE AutoATR automated ATR accessory.

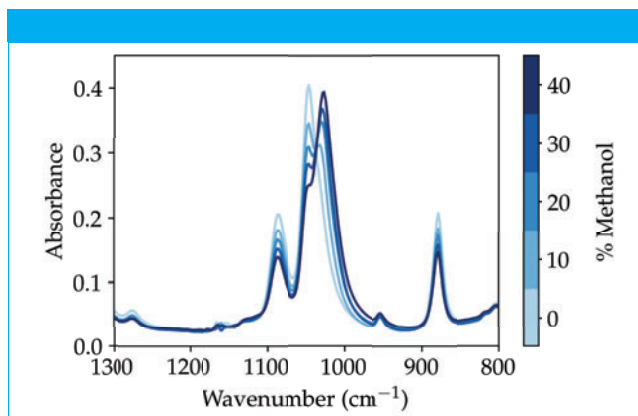


Figure 2: ATR spectra of each % *v/v* methanol in ethanol, collected with the AutoATR.

mixture was created using an Eppendorf micropipette and high-purity methanol and ethanol. After each mixture was created, a clean micropipette tip was used to distribute 120 μL of each solution into the AutoATR well plates after the background spectra acquisition was completed.

Results

The ATR spectrum of each methanol/ethanol sample is shown in Figure 2. The dominant spectral bands of ethanol correspond to the 1087 and 1046 cm^{-1} , while methanol exhibits a characteristic spectral band at 1033 cm^{-1} . The complementary change in concentration of the two species is highlighted by the isosbestic point at 1036 cm^{-1} of the ATR spectra.

Conclusions

Quantitation of contaminants and toxins such as methanol is critically important to ensuring the well-being of consumers. In order to streamline these measurements, automated technologies such as the AutoATR provide a uniquely accurate and high-throughput approach to ATR-based chemical identification. The AutoATR has proven capable of spectrally distinguishing methanol from ethanol and is well-suited for quantifying individual species in mixed solutions.

References

- (1) A. Dasgupta and A. Wahed, *Clinical Chemistry, Immunology and Laboratory Quality Control* (Elsevier, San Diego, California, 2014), pp. 317–335.

PIKE Technologies, Inc.

6125 Cottonwood Drive, Madison, WI 53719

tel. (608) 274-2721, fax (608) 274-0103

Website: www.piketech.com



Microparticles in Focus

Miriam Böhmler, Damon Strom, and Eleni Kallis, WITec GmbH

High-resolution measurements of particles are of great interest in many fields of application. With ParticleScout, WITec has developed a tool that makes it possible to find, classify, and identify particles automatically.

We encounter microparticles in many everyday products and in the environment. The analysis of fragments between 0.1 μm and 1 mm is challenging. Large areas have to be scanned, and even the most miniscule components must be recognized. The particles of interest need to be determined, classified according to selected properties such as shape or size, and finally their chemical composition has to be identified. The easiest and quickest way to perform this task is to use an automated and standardized microscopic inspection and chemical analysis. WITec ParticleScout, an advanced microparticle analysis tool, in combination with Raman microscopy, now offers this capability.

Experimental conditions

Two experiments were carried out with ParticleScout coupled to an alpha300 R confocal Raman microscope. Raman spectra were analyzed with the TrueMatch Raman database management system (all WITec). The excitation wavelength was 532 nm.

Sludge from a wastewater treatment plant was analyzed for the presence of microplastic particles (sample courtesy of Dieter Fischer, Leibniz Institute of Polymer Research, Dresden, Germany). Fifty grams of the sludge was pretreated and purified, then filtered in a two-stage process through silicon filters with 50- and 10- μm pore sizes, respectively. Raman spectra of a subset of found particles were acquired. In a second experiment tungsten disulfide (WS_2) nanoparticles several micrometers long and a few hundred nanometers thick were examined (sample courtesy of Reshef Tenne, Weizmann Institute,

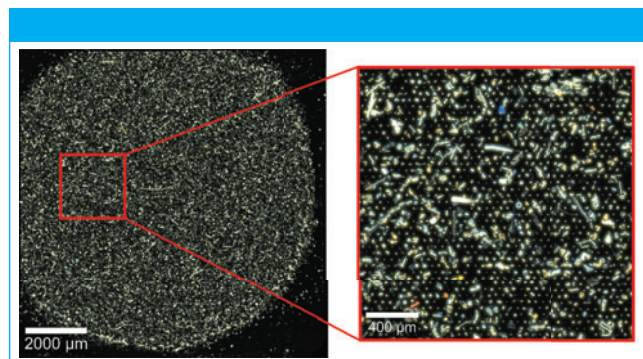


Figure 1: A $10 \times 10 \text{ mm}^2$ dark-field overview of a filter with microparticles from sludge was stitched together from 1089 images (left). From the selected area (right), Raman spectra were acquired from 18,000 fragments. The particles were automatically located and measured using the ParticleScout software.

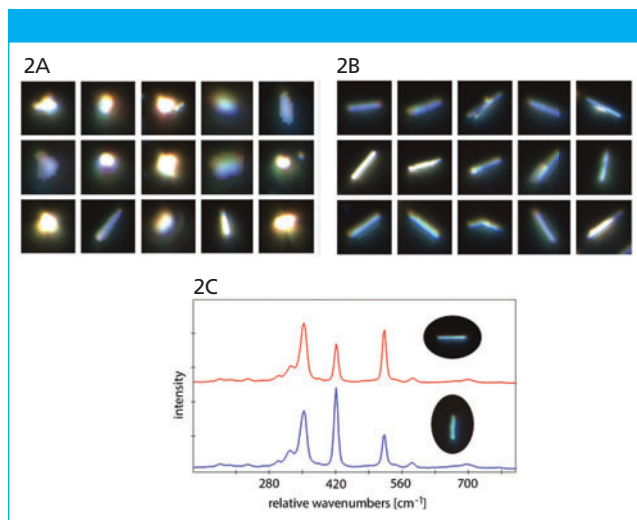


Figure 2: Under the microscope, WS_2 nanoparticles were imaged automatically with ParticleScout. A subset of 3135 detected fragments is shown (A). Of these, 218 granules had an aspect ratio of greater than 2.5 and were therefore classified as nanowires (B). (C) shows Raman spectra for two nanowires with different orientations. The intensity at 420 relative wavenumbers depends on the angle between the nanowire and the polarization of the laser.

Israel, provided through the Institute of Physical Engineering at Brno University of Technology [CEITEC], Czech Republic). Fragments shorter than 5 μm were located, then nanowires were classified by their aspect ratio, which was greater than 2.5.

Results

Microparticles were successfully discovered and classified using confocal white-light microscopy with the ParticleScout software. In the sludge sample, Raman spectra were acquired from 18,000 of the tens of thousands of microparticles that could be seen in the dark-field microscopic image (Figure 1). Forty six were plastic fragments: Polyethylene (25 pieces) and polypropylene (12 pieces) were the most abundant types of microplastic. Their sizes varied from 5 to more than 50 μm (circular equivalent diameter). Additionally, many different pigments and titanium dioxide particles were found.

In the WS_2 sample 3,135 nanoparticles were detected and imaged (Figure 2). From these, 218 were classified as nanowires according to their aspect ratios. The Raman peak at 420 relative wavenumbers (cm^{-1}) indicates the orientation of the nanowires with respect to the polarization of the laser light.

Conclusions

Using a confocal Raman microscope equipped with ParticleScout, large numbers of particles were easily located and classified into categories, as demonstrated using two samples from the fields of microplastic pollution and materials science. Raman spectra were measured automatically for all particles of interest. The seamlessly integrated TrueMatch database management software enabled quick identification of the particles. Reports summarize the results and describe the materials in terms of physical properties.

WITec GmbH

Lise-Meitner-Str. 6, 89081 Ulm (Germany)

tel +49 (0)731 140700

Website: www.witec.de

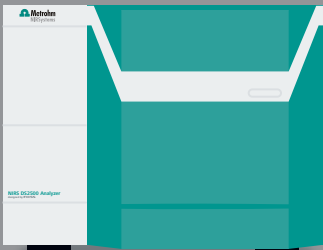
COMPLETE SOLUTIONS



Handheld



Process



Laboratory

Going Beyond Spectrometers to Build Complete Solutions

At Metrohm, we understand that you aren't looking for a spectrometer, you need answers that provide a complete solution.

Our team works with you from feasibility, to installation and beyond to deliver an application that works from the start. This coupled with our rugged handheld spectrometers, easy to use benchtop instruments, or powerful process analyzers turns instruments into solutions for:

- Raw materials inspection
- Quality assurance
- Process control
- And more

Find out more at
www.metrohm.com/spectroscopy



Make Spectroscopy a Breeze™

With BaySpec's New Palm Spectrometer (VIS/NIR/SWIR)



Introduces the world's first palm spectrometer VIS-NIR-SWIR (400nm-1700 nm). Featuring proprietary miniaturized spectral engine. Breeze is an one-button operation, Bluetooth connected spectrometer to do rapid chemical analysis anywhere, anytime.



BaySpec, Inc.

1101 McKay Drive | San Jose, CA 95131
(408) 512-5928 | www.bayspec.com